Design, Modeling and Control of Tip Actuated Soft Continuum Manipulators for

Applications in Endoscopy

By

Federico Campisano

Dissertation

Submitted to the Faculty of the

Graduate School of Vanderbilt University

in partial fulfillment of the requirements

for the degree of

DOCTOR OF PHILOSOPHY

in

Mechanical Engineering

May 8, 2020

Nashville, Tennessee

Approved:

Pietro Valdastri, Ph.D.

Robert J. Webster III, Ph.D.

Keith L. Obstein, M.D., M.P.H.

Nabil Simaan, Ph.D.

Thomas J. Withrow, Ph.D.

ACKNOWLEDGMENTS

I would like to acknowledge the many people who have contributed to this dissertation in various ways. It would not have been possible without their time, effort, and support, and I am very grateful for their contributions.

First and foremost, I would like to thank my family, in particular my wife Megan. She has been my main source of encouragement, support, and love through the ups and downs of research and I am incredibly grateful to have had her by my side during this time.

I would like to thank my advisors Pietro Valdastri, Keith Obstein and Bob Webster for their mentorship, support and enthusiasm throughout my graduate career. Your objective help, and constructive feedback have helped me grow as a researcher and as a professional.

I would also like to thank my dissertation committee: Bob Webster, Nabil Simaan, Tom Withrow, Keith Obstein and Pietro Valdastri. Thank you for giving your valuable time in support of this dissertation, and for providing helpful feedback for substantially improving this work.

I am also grateful to all my lab-mates and friends at StormLab USA, StormLab UK and MedLab and all the people that have been involved in the HydroJet system thorough all these years. In particular, I would like to thank Francesco Gramuglia, Imro Dawson, Gregorio Aiello and Chris Lyne for their help in the design, characterization and preliminary testing of the various components of the HydroJet Platform. A big thanks to Simone Caló and James Chandler for their work in coordinating shipments between Leeds and Nashville and for their assistance in setting up experiments and analyzing data. I would also like to acknowledge and thank Andria Remirez for her help both in the manufacturing of the HydroJet device and in the implementation and validation of the modeling and control methods presented in this work. Finally, a particular thank you to Addisu Taddese and Piotr Slawinski for many inspiring ideas and conversations that have contributed to the completion of this work.

TABLE OF CONTENTS

LIST OF TABLES

LIST OF FIGURES

LIST OF ABBREVIATIONS

SCM   Soft Continuum Manipulators

TFA   Tip Follower Actuation

UGI   Upper GastroIntestinal

LMICs   Low and Middle Income Countries

FEs   Flexible Endoscopes

EGD   EsophagoGastroduoDenoscopy

PRB-C   Pseudo Rigid Body Chain Model

HJ   HydroJet Endoscopic Device

NAG   Non-Atrophic Gastritis

CAG   Multifocal Chronic Atrophic Gastritis

IM   Intestinal Metaplasia

WAND   WAterjet Necrosectomy Device

Chapter 1

Introduction

Continuum manipulators, defined as flexible devices that take on curvilinear shapes as they are actuated, have proven useful in a variety of industries, from medicine to military applications [1]. The design of these devices is often biologically inspired, with motions mimicking those of elephant trunks or octopus tentacles [2]. In comparison to traditional rigid robots, continuum robots possess several unique capabilities, such as whole-arm grasping and manipulation [3], navigation through complex and unpredictable environments [4], and passive compliance, which can make them safer for interacting with humans [5].

In the medical field, non-robotic versions of continuum devices have long been used in the form of steerable catheters for cardiovascular interventions, flexible endoscopes for inspecting the digestive tract and lungs, and surgical tools that provide access to remote surgical sites via small openings and nonlinear pathways. When coupled with robotic actuation, these devices can become more precise, more dexterous and easier to use. Continuum robots for medical applications include robotic catheters [6], robotic flexible endoscopes [7], multi-backbone snake robots [8], concentric tube robots [9], [10], [11], [12], and steerable needles [13], [14]. While the flexibility of continuum robots provides advantages for minimally invasive surgery, many designs are still too stiff for certain clinical applications, in which insufficient compliance of the manipulator increases the risk of inadvertent tissue damage [15], [16].

As the demand for safer robots has increased, new compliant devices made of soft materials have started to populate the robotic field. These robots are composed primarily of materials with comparable or lower Young's modulus to those of soft biological materials, such as muscles, tendons, and skin [17]. This includes materials such as silicone, rubber,

or other elastomeric polymers that can be easily manufactured with varying form factors and material properties [18]. This subarea of compliant mechanics called "soft continuum mechanics" or "soft robotics" when the devices are coupled with robotic actuation, has grown exponentially in recent years. The use of soft, elastomeric materials for the manufacturing of continuum devices has enabled researchers in this field to develop continuum manipulators with variable stiffness [19] that can safely interact with highly unstructured environments [20, 21].

The vast majority of soft continuum manipulators presented to date can be categorized into two primary morphologies: (1) arms actuated through tension applied to tendons or cables running along their length (e.g. [22], [23], [24]), and (2) arms composed of multiple chambers that can be pressurized by air or fluid to produce bending as a result of pressure differences within the robot's cross-section (e.g. [25], [26], [27]). These two actuation morphologies are similar in that they both involve distributed loads along a central "backbone". While these actuation mechanisms maintain a high level of safety, the manufacturing process required to create these complex, miniature actuation geometries (through a multi-step molding process) greatly increases the overall cost of the device. When the cost of the device is high, reprocessing after each use is required, which further limits their use in medical application where affordable, disposable devices are needed.

A possible solution to reduce cost and simplify the manufacturing process is to remove the actuators from the body of the device and localize them at the tip. If the actuators are not localized along the body (and thus the body is passive), the body can be manufactured at low cost through extrusion or injection molding. In this dissertation, these manipulator designs are referred to as soft continuum manipulators under tip follower actuation (TFA) to highlight that the only source of actuation is a tip wrench and to differentiate them from the other two categories described above. An example of TFA can be found in [28], where the soft manipulator is steered via a tip wrench generated by a permanent magnet mounted on and controlled by an industrial robot arm. More examples can be found in [29, 30]

where the soft manipulator is actuated by water jets of controllable flow rates that spray water out from the tip of the manipulator to produce its deflection.

Despite the advantages of soft continuum manipulators under TFA in terms of cost and safety, their use still presents challenges in terms of modelling and control. These systems are highly affected by: (1) the non-linear response of the material, (2) manufacturing impurities that can create a nonhomogeneous strain distribution, (3) misalignment during assembly of the device, and (4) errors in calibration of material parameters [31]. All these factors affect the modelling and control performance.

1.1 Clinical Application

The main clinical application addressed in this dissertation is affordable diagnostic endoscopy, which is a growing need worldwide. Gastric cancer is the fifth most common malignancy in the world and the third leading cause of cancer death in both women and men around the world, with approximately one million new gastric cancer cases arising annually [32][33]. Low- and middle- income countries (LMICs) in regions such as East Asia, Eastern Europe, and Central and South America, are disproportionately impacted by gastric cancer due in large part to the high prevalence of infection with Helicobacter pylori (*H. pylori*), which is the leading cause of gastric cancer [34]. Early detection of cancer and related premalignant lesions has been shown to greatly reduce the morbidity and mortality associated with this disease [35]. The standard of care for gastric cancer screening is inspection with flexible endoscopes (FEs). These devices consist of a long flexible probe ending in an articulating tip that contains a camera, light, and a series of dedicated channels for irrigation, insufflation and insertion of procedural tools. The articulation of the tip is controlled by a double knob mechanism that requires intensive training for efficient and safe use. The inspection of the upper gastrointestinal (UGI) tract is achieved during a procedure called esophagogastroduodenoscopy (EGD), which involves c endoscopic examination of the UGI tract typically to the second portion of the duodenum. While EGD

3

is a very common procedure in the United States, with over 6.9 million annual procedures, successful implementation of EGD screenings in areas with high gastric cancer incidence, such as in LMICs, remains challenging [36].

The primary cause of low screening rates in these settings is the overall cost associated with mass screening programs. Performing procedures such as EGD with traditional FEs requires a dedicated endoscopy suite/area and highly trained personnel, due to the need for sedation and monitoring equipment. On average, while a diagnostic procedure only requires 5 or less minutes to complete, the total time spent by a patient in an endoscopy facility can range between approximately 60 to 120 minutes, as this includes the preprocedure/sedation assessment, sedation recovery, and discharge. The high initial capital cost of an endoscopic tower (about $80,000 USD) and flexible endoscope (about $20,000 USD) also represents a major economic barrier in some settings. In addition, currently used FEs are reusable devices that require specialized reprocessing and sterilization facilities. Lack of proper sterilization facilities greatly increases the risk of cross-contamination between patients [37], and the need for such specialized facilities limits screening access to patients living in close proximity to regional or urban endoscopy centers. Such economic and logistical challenges greatly limit the availability of FE-based screening in many H. pylori endemic areas.

The second clinical scenario discussed in this dissertation is endoscopic intervention for pancreatic necrosis. Patients who suffer from acute necrotizing pancreatitis may develop complications such as walled off necrosis (WON). Symptomatic pancreatic necrosis, including infected necrosis, can result in significant morbidity. Endoscopic management, consisting of transmural drainage and necrosectomy, has emerged as first-line therapy for symptomatic WON. The lack of dedicated devices and accessories for pancreatic necrosectomy currently present a major limitation for endoscopic intervention. Development of an effective disposable device specifically designed for endoscopic debridement of pancreatic necrosis would represent a major advance in the field and in patient care.

4

1.2 Motivation and Contributions

This dissertation is motivated by a lack of existing medical technology that specifically targets the two medical scenarios presented above, and by gaps in literature pertaining to modeling and control of soft continuum manipulators under TFA. In detail, the deficiency in existing medical technology is addressed by proposing two medical devices that use the force generated by miniature waterjets to provide both diagnostic (i.e providing camera articulation) and interventional capabilities for medical use. Preliminary work on waterjet actuation for clinical use is thus far limited to those presented in [29, 30]. For the first time, this work presents novel methods for controlling waterjet force to inspect and intervene in the endoluminal enviroment. Gaps in modeling and control of TFA soft continuum manipulators are addressed by proposing a unifying framework that addresses the unique issues of soft continuum manipulators under TFA and is independent of the actuation mechanism. While this work focuses on waterjet propulsion for TFA, which is required by the clinical application chosen, the modeling and control frameworks presented can be applied to various actuation morphologies (i.e. magnetic, soft pneumatic, tendons or cables) and continuum manipulator designs. The contributions of this work can be summarized as follows: (1) Design improvements to the platform presented in [29] to target the clinical need for affordable diagnostic endoscopy. These improvements are required to achieve controllable waterjet actuation; (2) Kinematic model for TFA soft manipulators undergoing large deflections. This work introduces the use of a disturbance parameter that can be updated by sensor feedback to address modeling inaccuracies that are inherent to continuum manipulator designs; (3) Closed loop control framework for TFA soft manipulators undergoing large deflections, which uses the combination of both actuator and pose feedback. The actuator feedback is utilized to both regulate the follower load and to compensate for nonlinearities of the actuation system that can introduce kinematic modeling errors. Pose feedback is required to maintain accurate path following; (4) Telerobotic operation scheme for TFA soft manipulators and the introduction of a method for detecting contact with the environment.

The work of the teleoperation scheme in conjunction with contact detection is crucial to enable the use of these devices in confined space; and (5) Design and characterization of a waterjet interventional soft continuum device that allows fragmentation of friable biological tissue during endoscopic procedures.

1.3   Outline

A detailed overview of each chapter, with emphasis on the contribution, is as follows:

- Chapter 2 presents the design improvements that are needed to achieve controllable waterjet actuation for an UGI endoscopic device that meets the needs for diagnostic screening in LMICs. A suitable endoscopic platform should meet the following requirements, 1) be easily controllable within both the esophagus and stomach, 2) be portable to easily move from one remote location to the next, 3) be disposable for sanitation purposes, and 4) be operable at minimal cost per procedure (i.e. 2-5 USD). With procedural costs in mind, any on-board system electronics should be reclaimable and not require any further reprocessing. A soft capsule endoscope was preliminarily introduced in [29], showing potential for enabling screening programs in LMIC and rural or remote locations. It articulates by using the propulsion force generated by waterjet actuators. In contrast to the Bowden cable actuation used in traditional flexible endoscopes, waterjet actuation uses a simple flexible tether that can be produced at low cost. The use of an incompressible liquid instead of air as the jet medium allows less stress to be created on the internal environment, thus the device can be used in contact with human tissue without causing damage. Water is also readily available in remote locations and this type of actuation does not affect the cost of manufacturing of the device. To maintain low cost (less than 2-3 USD) and support primary screening programs, the presented device is specifically designed as a purely diagnostic modality with the intent of identifying suspicious lesions and then triaging and referring patients if needed to a regional or central urban endoscopy

center for traditional interventional endoscopy with biopsies and/or endoscopic mucosal resection. In this manner, the novel device can serve as a tool to enable primary screening in settings where traditional endoscopy is limited. While the design presented in [29] addressed the sanitation and cost needs of LMIC, it did not provide adequate controllability for a high quality screening procedure. The scope itself was composed of a capsule attached to four separate, single-lumen tubes that were free to move independently, which caused issues with result repeatability. In addition, the control of jet actuation was confined to three discrete settings that greatly limited the resolution of motion control. Lastly, the waterjet actuation force was generated using a peristaltic pump, that caused the waterjets to follow an oscillatory wave, which created unstable behavior during the motion. Fixing the previous design issues for both the platform and the endoscope, and presenting a new soft continuum endoscopic device that allows accurate control of the waterjet propulsion represent the first contributions of this work.

- Chapter 3 covers modeling of soft continuum manipulators under TFA. In this chapter two modeling frameworks, a kinematic-based model (Pseudo Rigid Body Chain (PRB-C) Model) and a mechanics-base model (Cosserat Model) are presented. These frameworks can account for non-constant curvature and out-of-plane bending which are two common effects in soft continuum manipulator under TFA. This chapter also explores calibration issues that are common in any CM designs and proposes a method for compensating for unmodeled effects such as friction, nonlinear elastic and/or spatially varying material properties, and manufacturing imprecision. The proposed method corrects for these modeling inaccuracies by using a disturbance parameter that can be calibrated with the other model parameters, and then updated in real time by sensor feedback. Presenting modeling for SCM under TFA and improving the local model accuracy using a disturbance parameter are additional contributions of this work.

- Chapter 4 covers control of soft continuum manipulators under TFA. The control challenges of SCM (i.e. delays in signal propagation, high sensitivity to changes in actuator wrench, non linear behavior of the actuation system) are addressed by proposing a control strategy based on the Cosserad rod framework, which incorporates both actuator and pose feedback. Actuator space feedback is used to account for the nonlinearities of the actuation system that can lead to incorrect tip wrench estimation, which would produce error in the kinematic model. Pose feedback is utilized to maintain accurate path following. The presented control strategy limits the complexity of the kinematic model (i.e. no need to integrate complex constituitive laws) and mitigates the disturbance effects arising from both incorrect calibration and imperfect assembly, which are common issues in soft continuum manipulators designs. The addition of sensing does not increase the overall cost of the device thanks to the integration of inexpensive orientation sensors. Presenting and experimentally validating the proposed closed loop control for TFA soft continuum manipulators is another contribution of this work.

- Chapter 5 presents the teleoperation scheme and introduces a method for contact detection of soft continuum manipulators under TFA. Both components are important to show the possible use of soft continuum manipulators under TFA in the proposed medical scenario of endoscopy. Teleoperation and contact detection for the proposed application were not explored previously in literature and present an additional contribution of this work.

- Chapter 6 presents the design and characterization of an interventional waterjet device. In addition to providing an articulation method for soft devices, waterjets have the advantage of being capable for use as an interventional tool to fragment friable biologic tissue during surgical or endoscopic procedures. Necrotic tissue, for example, presents a friable, low bonding material that could be targeted during endoscopy.
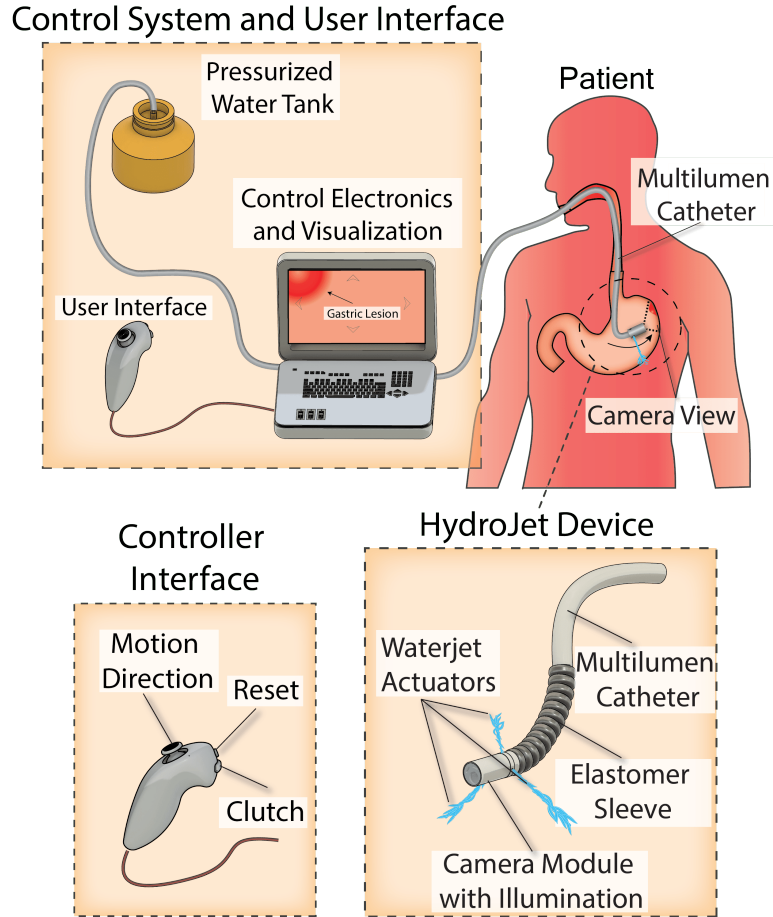
Figure 1.1: Overview of the HJ endoscopic device: a soft continuum endoscope for use in LMIC and remote locations. The endoscope articulation system consists of a portable interface and a pressurized water tank. The articulation of the endoscopic camera is obtained through bending caused by waterjet propulsion on a soft elastomer body.

The proposed interventional tool can be passed through the channel of a standard endoscope to assist during minimally invasive procedures. While interventional waterjet tools exist for surgical procedures [38, 39], the application for gastrointestinal endoscopic intervention represents a need that has not been previously explored in the literature.

In summary, a detailed overview of the two medical devices that are presented in this dissertation are as follows:

The first device is the HydroJet (HJ) endoscopic device, which is a soft continuum en-
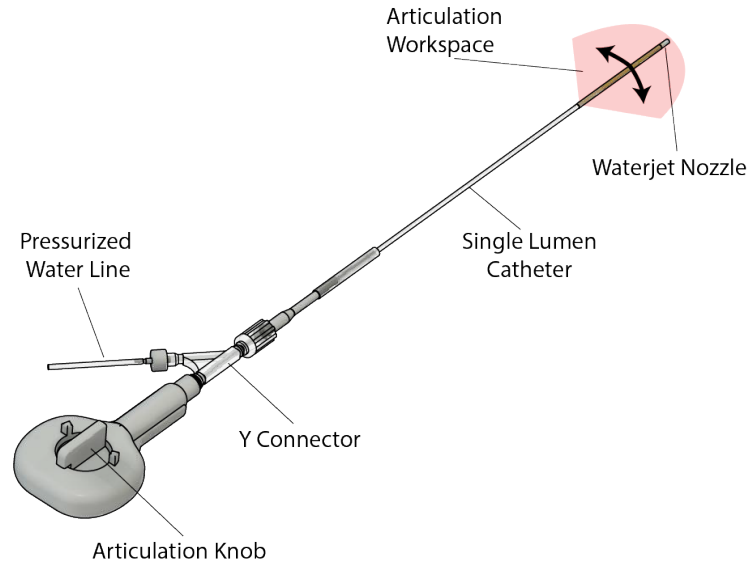
Figure 1.2: Overview of the WAter-jet Necrosectomy Device (WAND): an interventional device for fragmenting low bonding material such as necrotic tissue through use of directed waterjet pressure. The device is articulated through the manual rotation of an articulation knob, while the waterjet pressure is controlled by a foot pedal.

doscope that addresses the need for upper GI cancer screening in LMIC and rural/remote locations (Fig. 1.1). The HJ uses three waterjets spaced 120 degrees around the diameter of a camera-containing capsule to articulate the endoscopic device within a confined environment. Compared to traditional Bowden cables present in standard endoscopes, the waterjet actuation allows the HJ endoscope to be swallowed and disposed after the procedure with exception of the camera, which is extracted and reused with each new procedure. This is a significant advantage for LMIC as the endoscope does not require expensive repair or specialized reprocessing facilities. The propulsion and mechanical bending of the endoscope are designed to perform the typical diagnostic tasks while avoiding damage to the tissue by waterjet pressure. Tissue preservation is achieved by finding the optimal balance between bending and the force generated by the waterjet system.

The modelling and control strategies presented in each chapter for soft continuum manipulators under TFA are experimentally validated on the HydroJet. Ultimately, results show the ability of the device to inspect key areas within a geometrically accurate stomach

phantom to perform gastric cancer screening.

The second device proposed is an interventional WAterjet Necrostomy Device (WAND) (Fig. 1.2). The mechanism for tissue fragmentation by the WAND consists of a highly focused waterjet delivered through a 2 mm steerable catheter. The device offers adjustable levels of water beam intensity controlled through a foot pedal, as well as 180 degrees of articulation that is independent of the endoscope tip. The use of waterjet pressure serves the dual purposes of dissecting/fragmenting necrotic tissue and facilitating irrigation of the necrotic cavity. The prototype was entirely fabricated using a Stereolithography 3D printer that uses ultraviolet light to cure photosensitive polymers. The articulation consists of a one degree of freedom push-pull mechanism operated by rotating a knob located on the device handle. Results show successful fragmentation of multiple densities of material including freshly explanted human pancreatic necrosis, at pressure and flow rates well below the threshold necessary to cause tissue damage.

Chapter 2

Hydrojet Endoscopic Device: A Waterjet Actuated Soft Continuum Endoscope for Upper
GI Screening in Low-resource Settings

2.1   Introduction

Gastric adenocarcinoma is the fifth most common malignancy in the world and the
third leading cause of cancer death in both women and men. In 2012, its estimated global
incidence was of 952,000 new cases with an estimated 723,000 deaths worldwide [40, 32,
34]. It is projected to rise from fourteenth to eighth in all-cause mortality in the near term,
primarily due to the growing and aging populations in the high incidence areas, such as
Latin America and eastern Asia [41, 42]. Unlike any other major cancer, gastric cancer
demonstrates marked geographic variability in regions and within countries, with more
than 70% of incident cases concentrated in low- and middle-income countries (LMICs)
[40, 32].

Gastric adenocarcinoma is a multifactorial process, which progresses through a series
of histopathology stages: normal mucosa, non-atrophic gastritis (NAG), multifocal chronic
atrophic gastritis (CAG), intestinal metaplasia (IM), and finally to dysplasia and adenocar-
cinoma [43, 44]. The substrate leading to early gastric mucosal inflammation and chronic
gastritis is driven by H. pylori infection, host genotypes and responses, and dietary and en-
vironmental factors [45]. Over 80% of the general population in LMICs of Central America
(i.e., Honduras, El Salvador, Guatemala, and Nicaragua) are infected with H. pylori [43].
H. pylori eradication may help prevent gastric cancer in individuals with chronic gastritis,
but is an inadequate strategy in patients with precancerous lesions. CAG, IM, and dysplasia
are considered premalignant lesions, and are also highly prevalent (20-25%).

Early detection of premalignant lesions effectively reduced the mortality rate associ-
ated with gastric cancer in Japan and Korea [46]. Gastric cancer screening procedures are

conducted at regional or urban medical centers using flexible endoscopes, which provide high definition video and a tool channel for interacting with the tissue (e.g., tissue biopsy, endoscopic mucosal resection). After a procedure, the flexible endoscope needs to be reprocessed in order to sanitize it for the following case [47].

Despite the high incidence of gastric cancer and the critical need for early detection, screening programs with flexible endoscopy are not common in LMICs and remote locations. The high initial cost of an endoscopic tower (e.g., about 80,000 USD), the cost and the time associated with repairing the instrument (flexible endoscope repairing centers are rarely located in LMICs), and the need for specialized equipment for reprocessing the endoscope in between procedures are the most relevant roadblocks to screening programs in LMICs. The limited portability of flexible endoscopes also limits screening to patients near regional or urban endoscopy centers.

An endoscopic platform for upper gastrointestinal (UGI) cancer screening programs in resource-limited and/or remote areas of LMICs would ideally need to be simple to control within the esophagus and stomach, easy to transport between remote locations, mechanically robust, disposable for sanitation, and ultra-low-cost (2-5 USD per procedure).

Alternative endoscopic screening technologies that could potentially be used in LMIC include capsule endoscopes and robotic endoscopy. Capsule endoscopes provide sanitary screening through disposability without the need for reprocessing [48], but they lack controllability and have a high cost-per-procedure (about 500 USD) [49]. Robotic endoscopy still at the stage of preclinical [50, 51] or pilot clinical [52] trials provides a highly controllable option, but also comes with a high cost-per-procedure that is not suitable for LMICs. Despite the considerable need for endoscopic screening technologies suited to low resource settings, there are currently no options that meet the unique needs of LMICs.

The HydroJet endoscopic platform was previously introduced in [29], showing potential for enabling screening programs in LMICs and rural or remote locations. The HydroJet (Fig. 2.1) is a soft continuum robot that is maneuvered using three water jet actuators. In

contrast to the Bowden cable actuation used in flexible endoscopes, jet actuation allows for a simple flexible tether that can be produced at a low cost. This solution is intended as a pure diagnostic device (i.e., no therapeutic or instrument channel) with the intent of identifying suspicious lesions optically and then triaging patients to a regional or central urban endoscopy unit for traditional therapeutic endoscopy with biopsies/mucosal resection. Thi technology is targeting a population that would otherwise not be screened and subject to high disease incidence and mortality due to the numerous barriers to standard flexible endoscopic screening in rural/remote areas of Central America.

Despite addressing the sanitation and cost needs of LMIC, the HydroJet design presented in [29] did not provide adequate controllability for a high-quality screening procedures. Due to the use of On/Off valves, the jet actuation control was confined to three discrete settings (high, medium and low throttle), greatly limiting the resolution of motion control. Additionally, in the previous system, water for jet actuation was pressurized by a diaphragm pump, which both relies on external power and has a wetted path that is not inert. Non-inert parts corrode after long-term exposure to water, affecting system operation and potentially contaminating water used for the procedure, which endangers patients.

This chapter presents the current platform and discusses the implications of the design optimization for the clinical efficacy of the device. First, the pump was replaced by the series of dispensing vessel and an air pressure tank. A pressure regulator connected to the dispensing vessel allows precise regulation of the overall pressure, without requiring water to constantly flow within the system. On/off valves were replaced by proportional valves which allow selective control of the flowrate at each waterjet. Next, the four full-length single lumen tubes were replaced with a multilumen catheter connected distally to a low stiffness section, which is constituted by a soft elastomer sleeve that wraps around single lumen flexible tubing. This allows the tip of the scope to achieve high bending angles while maintaining a uniform body. In this case, the force generated by waterjets is not dependent on the constitutive mechanical strain relationships of the sleeve but instead is uniquely

14
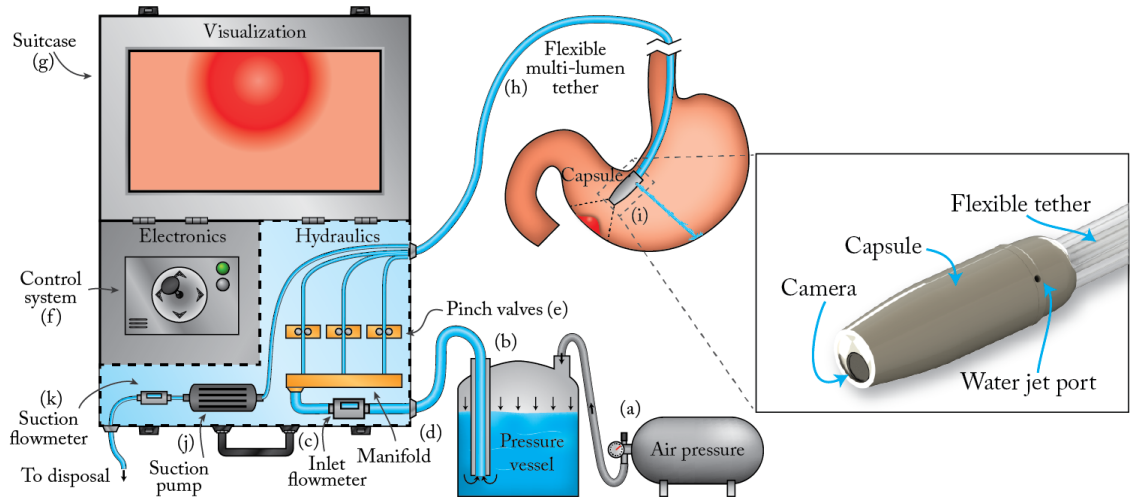
Figure 2.1: Diagram of the HydroJet system: (a) Air pressure tank, (b) Dispensing pressure vessel, (c) Inlet flowmeter, (d) Manifold, (e) Pinch valves, (f) Control system, (g) Suitcase, (h) Multi-lumen tether, (i) Capsule, (j) Suction pump, (k) Suction flowmeter.

dependent on the fluid flow rate passing through the tubing and the geometry of the nozzle. The mechanical deflection can be determined independently by choosing the geometric and material properties of the sleeve based upon the desired application. The number of actuating jets was reduced to three, enabling smaller capsule and tether diameters. Finally, the platform was redesigned to fit inside a suitcase the size of an airline carry-on, thus improving portability. The power consumption of the entire platform was optimized to be easily adapted to battery operation. These improvements make the HydroJet well suited as a screening aid to complement flexible endoscopes in LMIC.

2.2   Platform Overview

The HydroJet is an endoscopic platform (Fig. 2.1) designed for upper gastrointestinal cancer screening. The capsule (10 mm diameter by 32 mm length) carries a camera within a hermetically sealed shell (Fig. 2.2). The camera, which contains embedded light emitting diodes (LEDs) for illumination, is loaded into the back half of the capsule shell and connects through a four prong snap connector. The front half of the capsule is then attached to
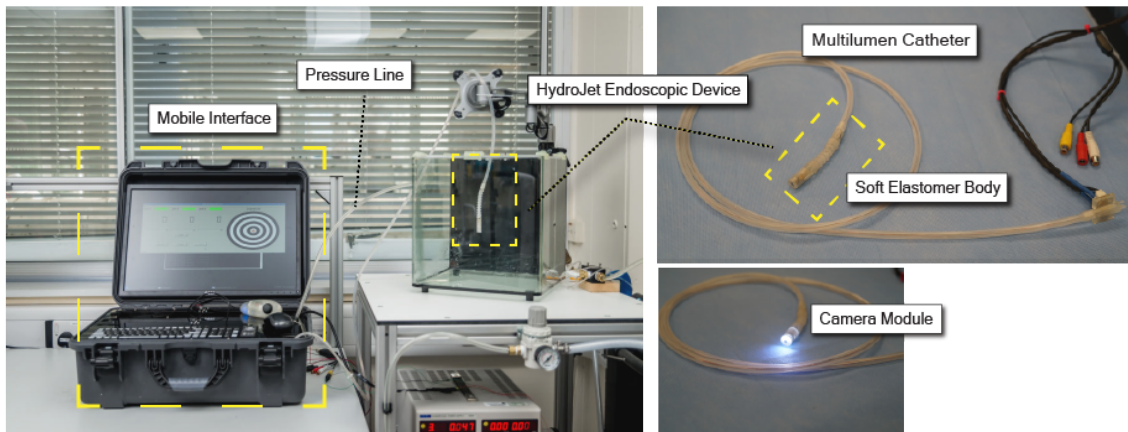
Figure 2.2: HydroJet platform designed to be easily transportable. The HydroJet endoscopic device is completely disposable with exception of the camera module that can be reused for a different procedure.

restrain the camera and seal the capsule. The capsule body contains three jet ports, spaced at 120 each around the diameter, which serve as actuators when pressurized water is ejected from the capsule. Jet actuation force is controlled externally by the components in the suitcase, resulting in a mechanically simple capsule design. The HydroJet is designed with disposable and reusable components (see Fig. 2.1). After completion of a cancer screening procedure, the HydroJet outer shell and tether are discarded and the capsule's camera (preserved from patient contact by the outer shell) is reclaimed without reprocessing.

The capsule and tether form a system that is similar to traditional endoscopes. Through selectively throttling each of the water jets, the HydroJet can autonomously pan the capsule with two degrees of freedom (DoF). Linear control of the capsule is accomplished by pushing/pulling the tether. Adjustment of the tether pivot length can be varied as needed to visualize the entire esophagus and stomach. By combining the 2 robotic DoFs, and a manual DoF given by pushing and pulling the tether, the HydroJet can achieve 3-DoF motion to explore the gastric cavity. Suction to remove the excess of water from the stomach is provided through the tether by a dedicated line, which does not require an additional port on the capsule.

The hydraulic system, part inside the suitcase, is designed to precisely regulate flow to each of the capsule jets, and in turn control jet actuation force. Compressed air is used to pressurize water in a dispensing pressure vessel (Fig. 2.1). The water is delivered from the vessel (b) to a distribution manifold (c). Throttle control of the jets is achieved using a set of proportional pinch valves (d), which independently regulate the flow rate of each jet. These valves use a specialized piston to pinch the line closed without contacting the water, and provide a simple and responsive way to control the flow. Suction is provided through the multi-channel tether into a hygienic receptacle. Similarly to traditional endoscopy, a button can be depressed at the endoscopists discretion to trigger the pump and begin suction. In case of suction lumen obstruction, backflow flushas in traditional endoscopy, can be performed to clean and clear the suction port. Two flowmeters (c and k in Fig. 2.1) monitor the rate of fluid flow to and from the stomach, in order to maintain a safe balance (typically around 1.3 liters).

2.3   System Design and Fabrication

2.3.1   Dispensing Vessel and Air Tank

The dispensing pressure vessel (Millipore, Model: 6700P05, Volume: 5 Liters, Max operating pressure: 100 psi) is responsible for providing the pumping power for the jet actuators. The vessel contains enough water for approximately two screening endoscopies, and can be refilled without stopping the procedure. Compressed gas is used to pressurize the vessel, and water is expelled from the vessel through a dip tube (Fig. 2.1). The use of the dispensing pressure vessel greatly simplifies the pumping system so that only inert parts contact water, favoring long-term system reliability and patient safety. Alternative pump options such as peristaltic pumps are often used when an inert wetted path is needed, but despite this and resistance to occlusion, the output pressure and flow rate fluctuates drastically over a pumping cycle. These fluctuations result in an unsteady jet force and unstable

capsule motion, interfering with visual diagnostics. In contrast, pneumatic pressurization does not rely on reciprocating parts, and can provide an inherently stable delivery pressure to enhance capsule stability. Another notable advantage of pneumatic pressurization is the independence from electrical power. Since compressed air can be carried in commercial tanks, this approach offers unique advantages in terms of portability and utility in LMIC.

2.3.2   Suitcase

The platform was developed for easy transport and storage in a compact and durable suitcase that contains all of the components of the system (Fig. 2.1). The suitcase is divided into hydraulics, control electronics, and visualization sections. Each of the three sections was designed to be hermetically separated thus allowing for protection from potential water damage. In keeping with the design goals of the water distribution system, the pinch valves (Resolution Air, model: MPPV-2) provide flow control without exposing the valve parts to the water. This inert wetted path is an advantage in LMIC due to the lack of training and other resources necessary for routine maintenance. This design ensures that corrosion from exposure to potable water will not occur with long-term use, and that the water will not be contaminated prior to delivery to the patient. This makes the HydroJet platform inherently safe, as lack of proper maintenance or operation will not present any health complications to the patient. The operator controls the HydroJet through a custom user interface implemented on an Arm A8-Cortex processor running Linux. The images streaming from the capsules camera and the opening level for each of the pinch valves are shown on the monitor in real-time, together with the amount of water currently present in the patients stomach, as measured by the flowmeters.

2.3.3   HydroJet Endoscopic Device

The first step in the design of a soft continuum scope that articulates using waterjets, is correct sizing of the hydraulic system to ensure that the waterjet propulsion can be used

safely in close contact with internal tissue. The design for medical use is also subject to limitations of workspace articulation (high bending angles within relatively small workspace) and overall diameter of the scope (less than 10mm in diameter to be able to pass through the esophagus). These factors are balanced through the selection of appropriate material and geometric properties of the sleeve (such as elasticity, density, length etc.) that produce the desired bending based on a tip force.

2.3.3.1 Capsule

The capsule components are made from a durable plastic (Objet Verowhite Plus) via 3D printing (Objet Geometries Ltd., Model: OBJET 30). Suction is provided by a dedicated port off-board the capsule, thus eliminating the need for additional suction ports on the capsule. The reusable inner core (Fig. 2.2) contains the camera module (Aidevision, Model: AD- 3915): an ultra-mini endoscopic camera (Diameter: 3.9 mm, Length: 14.5 mm, 54 field of view, 65 USD), which is used for diagnostics and control of the capsule, and two ultra-bright LEDs. The inner core is hermetically sealed within the outer shell, which snaps together to facilitate easy loading/unloading between procedures. A four-pole female connector, located on the rear of the inner core, provides electrical connectivity through the multi-channel tether. The inner core module is easily inserted or removed from the outer shell, allowing on-board electronics to be reclaimed and reused.

The jet ports feature a converging nozzle design, and jet actuation force is controlled by the hydraulic system. The purpose of the converging design is to accelerate the flowing water as it leaves the capsule, thus producing a reaction force in the opposite direction. The nozzle entrance is 1.6 mm to match the internal diameter of the jet tubes, and the nozzle exit diameter is 0.75 mm. The smooth transition between the inlet and outlet diameters contribute to an efficient nozzle design by eliminating regions of recirculating flow.

2.3.3.2 Multilumen Catheter

A custom-made multilumen tether connects the capsule to the water distribution system and is composed by seven total lumens, one centrally located and the remaining six divided equally around the diameter. The cross section is designed so that it incorporates channels for actuation, suction, and wiring. All outer channels are equally spaced and identical in shape and dimensions. Three of these channels are used for actuation and the other three are used for suction. Although it would be possible to have only a single channel available for suction, and thus having only four outer channels, this could cause undesirable bending behavior. By using six channels, the nozzles for the jets always line up with the channels supplying them with water. Additionally, with the current design the bending stiffness in each jets bending direction is identical, which would not be the case with only four outer channels. The central channel is used for the wiring of the capsule. This way all wires are close to the neutral axis of the tether, limiting their effect on the bending stiffness of the total tether. Additionally, strains near the neutral axis are low during bending, reducing the chance of damage to the wires. In order to extrude the multi-lumen tether, a custom pin and die set was fabricated. The medical-grade silicone material, Nusil 4080, was used for the extrusion.

2.3.3.3 Soft Elastomer Sleeve

To work as an effective endoscopic device for upper gastrointestinal inspection, the HydroJet is required to achieve high bending angles within a relatively small workspace. To facilitate greater range of motion, a low stiffness bending section was developed and integrated between the capsule-shaped tip and the multi-lumen catheter, as shown in Fig. 2.3. The low stiffness bending section is composed of two main parts: 1) three thin-walled tubes (35D Pebax 6fr 0.008" wall, Apollo Medical Extrusions), responsible for carrying pressurized water from the multi-lumen catheter to the water jet nozzles, and 2) a custom elastomeric bellows for setting the stiffness of the soft body and for constraining the internal
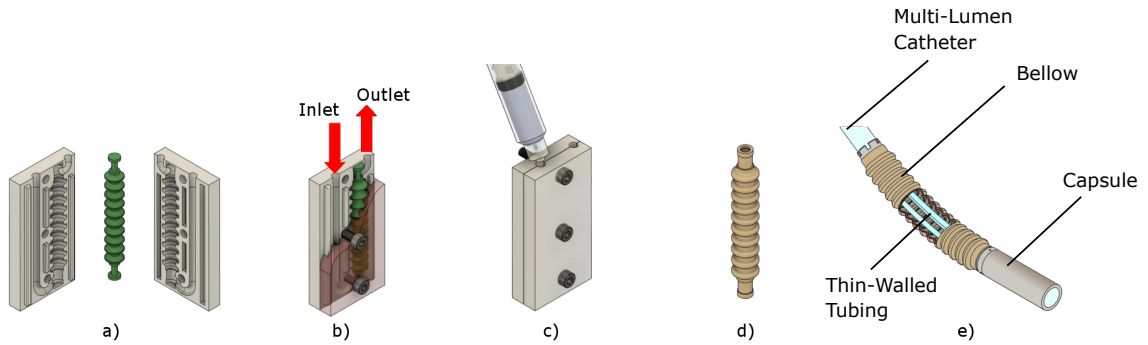
Figure 2.3: Manufacturing process for the soft elastomer sleeve

tubes to prevent their relative motion or buckling. The internal tubes were twisted around themselves to achieve a relatively even stiffness in all bending directions. The bellows was manufactured of soft silicone (Ecoflex 00-30, Smooth-On, USA) through injection molding and has a maximum and minimum outer diameter of 10.5 mm and 6.5 mm, respectively, with wall thickness of 0.7 mm (under zero strain). The internal tubing and bellows were assembled as shown in Fig. 2.3. The resulting body allows bending relative to the base connector if actuated under TFA.

2.4   Experimental Analysis

2.4.1   Waterjet Force Characterization

Water jet actuation leverages a pressurized liquid ejected through propulsion nozzles to obtain thrust. The reaction thrust characteristic of a propulsion system has been extensively studied in the past [53, 54]. Two internal profiles with different aspect ratio (A/R) were designed in order to quantify the relationship between reaction thrust and nozzle cross-sectional area under the condition of different flow rates. Each profile has an exponential convergence along the cross-sectional axis.

Considering the fluid conservation of mass and assuming a time invariant laminar flow, the thrust depends uniquely on the internal geometry of the capsule jet as follows:

$$F = -\dot{m}(v_{in} - v_{out}) + \int_{A_{out}} p_{out} n \, dA_{out} \qquad (2.1)$$

where $\dot{m}$ is the mass flow rate through the cavity, v_{out} and v_{in} the outlet and inlet velocity, p_{out} the pressure acting on A_{out} and n is the unit vector normal to the inner wall surface. The analytical model obtained by integration over the two different contours was then validated using experimental data. An upper limit pressure of 3 bar was implemented to prevent potential damage to the tissue [29].

Characterization of water actuation force was performed to establish the relationship between valve position and jet force, and to examine hysteresis in jet control. Jet force was measured using a calibrated load cell (ATI Industrial Automation, Model: NANO17, resolution 0.318 gram-force). The capsule was connected to the load cell using a 265 mm rod and jet force was measured using a cantilever arrangement (Fig. 2.6). Five trials were conducted showing good repeatability of results. At a standard system pressure of 80 Psi, the maximum measured actuation force was 0.128 N with the valve fully opened. The measured jet force as a function of valve position exhibits a linear region in the center of the input range, which is favorable for capsule controllability.

Although control is repeatable, hysteresis is present between the opening (unloading) and closing (loading) of the valve. This discrepancy is likely due to positional inaccuracies in the pinch valves themselves, rather than a fluid dynamical hysteresis.

The waterjet experimental testing aimed to: i) characterize the relationship between thrust (with changes in outer diameter) and flow rate and ii) estimate the error due to rapid prototyping. Pressurized water was provided to the proximal opening of the jet using a PVC plastic tube (Shore hardness A90, 1.6mm inner diameter) before being expelled out through the smaller external opening. In order to compare the two different shapes, the upstream pressure was fixed at 70 psi and the flow was controlled using a fixed-step valve.

The average of three experiments on the same profile, for each different A/R and diameter, was compared to the analytical model in order to find a shape calibration coefficient

22
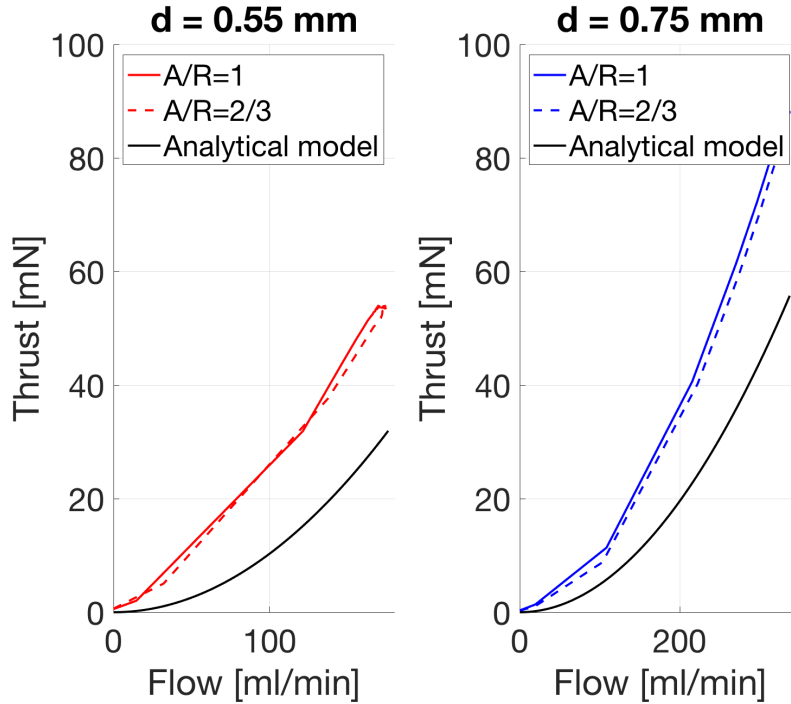
Figure 2.4: Average measured thrust on five experiments with different A/R, compared with the analytical model with outer diameter (d) and inner diameter (1.6mm).

(Fig.2.4). The results show that the experimental data follow the general thrust equation trend thus the actual thrust can be calculated at each time.

In order to understand the error due to rapid prototyping, the same nozzle profile was fabricated five times and the data was compared to obtain the absolute and relative error of the process (Fig.2.5). The maximum absolute error is 10 mN obtained for an effective thurst of 70 mN. This correspond to a relative error of 18% with respect to the average value. However, these plots show that the trend due to the process is linear, thereby allowing for easy compensation and effective thrust estimation at each time.

2.4.2 Flowrate Characterization

Volumetric flowrate was estimated starting from the energy conservation equation:

$$\frac{p_2 - p_1}{\gamma} + \frac{v_2^2 - v_1^2}{2g} + h_l = 0 \tag{2.2}$$

23
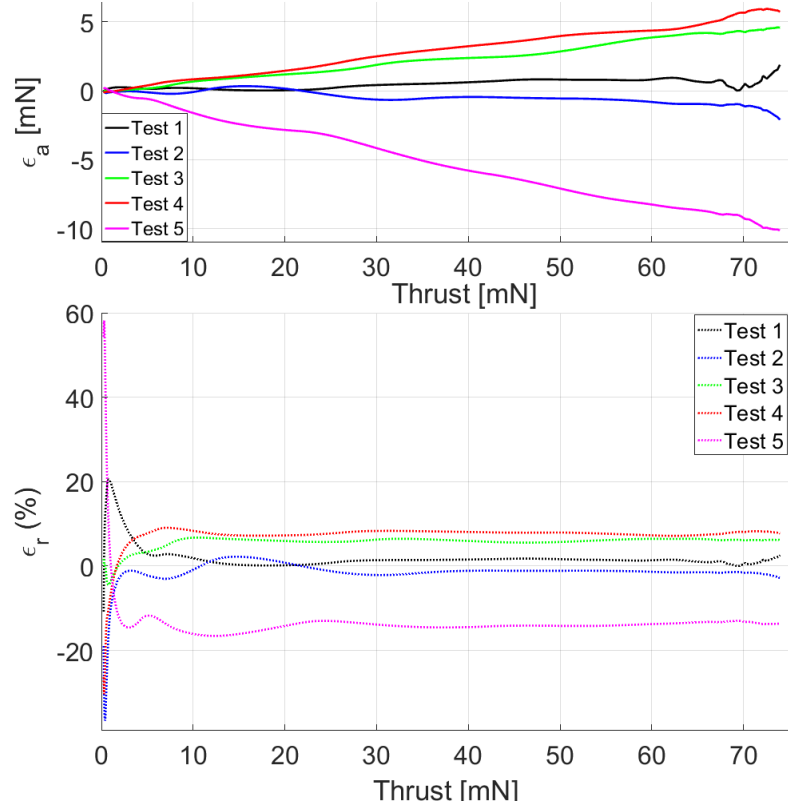
Figure 2.5: Absolute (ε_a) and relative (ε_r) error due to rapid prototyping calculated with respect to the average thrust. $\varepsilon_{ai} = F_i - \mu_i$; $\varepsilon_{ri} = \frac{F_i - \mu_i}{\mu_i}$ where F_i is the ith thrust sample and μ_i is the average thrust in the ith experiments.

where p_2 and p_1 are pressures at two location on the hydraulic system, v_2^2 and v_1^2 are fluid velocities, $\gamma = \rho g$ is the specific weight of the fluid and h_l is the head loss in the tubing that can be calculated as:

$$h_l = f \frac{L}{D} \frac{v^2}{2g} \tag{2.3}$$

where f is the Darcy friction factor, L and D are the length and internal diameter of the tube, v is the velocity of the fluid and g is the gravitational constant.

Jet flow rate was measured during jet force testing using an ultrasonic flowmeter (Atrato, Model: Titan 760), which provides the instantaneous flow rate through the jets. As expected from the jet force measurements, hysteresis in flow control is present in the experimental
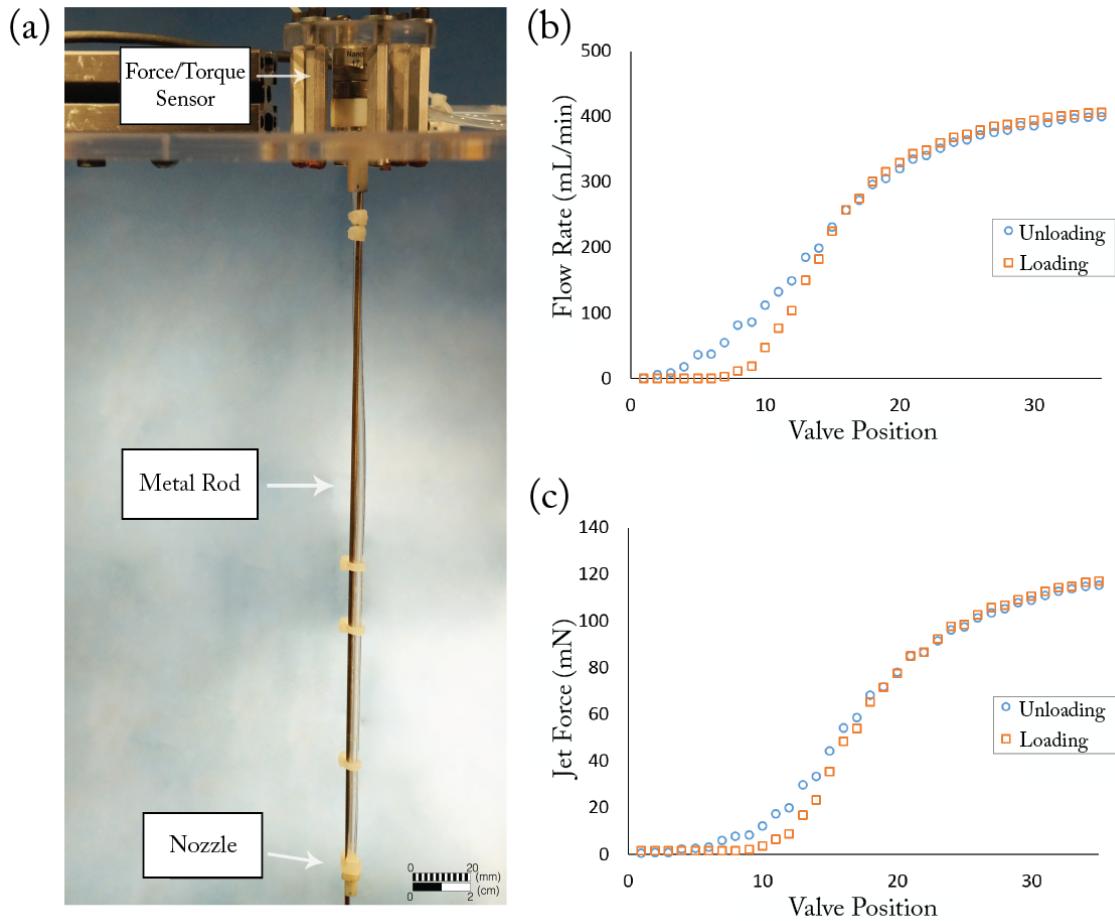
Figure 2.6: (a) Experimental setup during the force characterization experiment. (b) Jet flow rate as a function of valve position. (c) Jet actuation force as a function of valve position.

data (Fig. 2.6). Although fluid flow should show no hysteresis, pinch valves rely on a mechanical drivetrain and show some error in control. The hysteresis is seen to increase as the valve clamping force increases, due to the greater forces imposed on the valve drivetrain. When loaded, both frictional forces and motor dynamics contribute to hysteresis in the drivetrain. Using a fixed upstream pressure of 80 Psi, the maximum measured flowrate was 410 mL/min that agrees with classical fluid modeling equations.
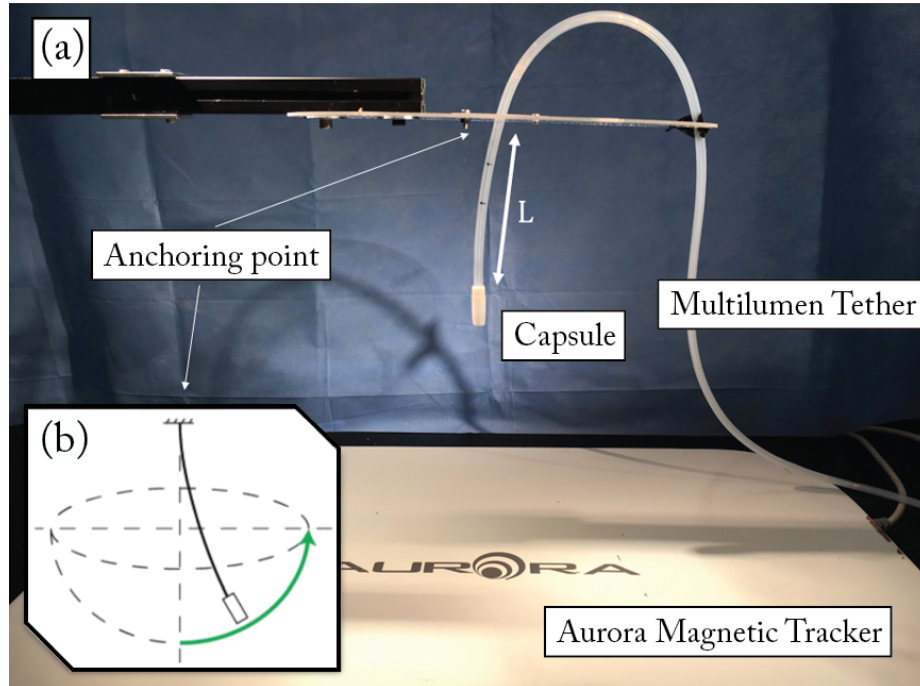
Figure 2.7: (a) Custom experimental test-bench: The capsule was held vertically using an aluminum metallic arm with a custom 3D printed holder to provide a well-defined pivot point. (b) Programmed sweep operated controlling onlyone pinch valve sending one-step forward command every 5 seconds until valve is completely open.

2.5 Feasibility Study

As a first step towards the development of the platform, the feasibility study was performed using a version of the scope composed exclusively of a capsule connected directly to the multilumen catheter (Fig. 2.7). The deflection using the soft sleeve is characterized starting from chapter 3.

2.5.1 Range of Motion Using Single Jet Actuator

This experimental trial aimed at understanding the controllability of the capsule while throttling a single jet from fully closed to fully open. Camera stability for internal visualization is the main requirement for any endoscopic platform. This trial was carried on to quantify the number of stable positions the capsule can reach and the maximum displace-
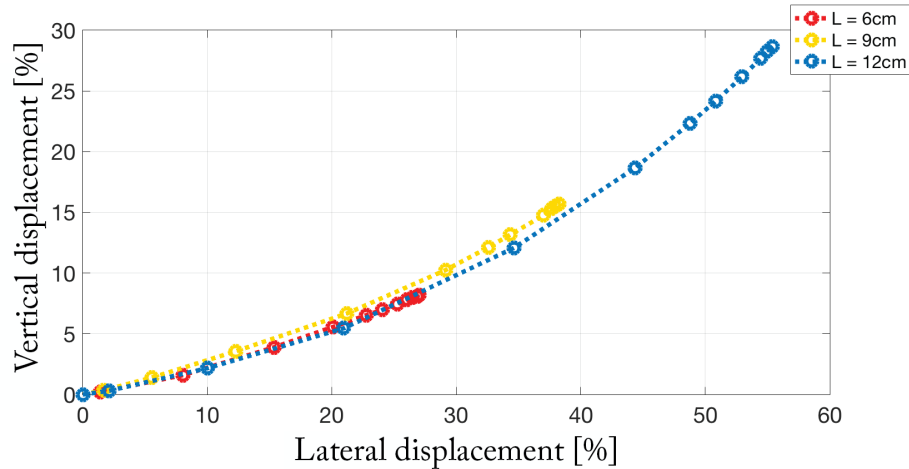
Figure 2.8: Single jet motion result: A total number of 13 stable points (dots) were found after the trial for each tether length. Maximum lateral displacement of 56% with respect to the tether length corresponds to 6.60mm or 50 degree angle with respect to the vertical.

ment that can be obtained with respect to the free length of the tether. To be considered a stable position, the capsule must be still enough to use the camera for visual inspection. The capsule motion was monitored using a 6-DoF magnetic coil (0.9 mm diameter, 12 mm length) embedded in the capsule and excited with an electromagnetic transmitter (Northern Digital Inc. (NDI), Model: AA138). During the study, the tether was secured and held vertical using an aluminum metallic arm with a custom 3D printed holder to provide a well-defined pivot point (Fig. 2.7). Water was fed to the capsule internal nozzles using the multi-lumen catheter described in section B.2. Three different tether length (L) 6 cm, 9 cm, and 12 cm were tested in order to obtain the relationship between lateral and vertical displacement and therefore quantify the maximum motion with respect to the vertical position. A single sweep motion was programmed using the suitcase control electronics. The sweep consisted of gradually controlling the jet pinch valve, sending the capsule one step forward command every 5 seconds, until the valve was completely open.

A plot of the stable positions reached by the capsule is shown in Fig. 2.8. Thirteen stable position were found for each tether length that correspond to 2197 positions using the combination of three jets. The experiment shows repeatability of the results despite vary-

ing the tether length. The motion was constrained, as expected, in a semi-hemispherical workspace. The maximum lateral displacement was 56% , 38% and 28% of the 12 mm, 9 mm and 6 mm free lengths, respectively. These results show maximum angle of 50 from the vertical that can be adjusted changing the tether length without losing controllability. This is the most important result since controllability is guaranteed even with changes in the anchoring point, and means that many common tasks, such as retroflexion, can be obtained by pushing more tether inside the stomach while adjusting the position using jet propulsion.

2.5.2 Full Workspace Characterization

To obtain the full hemispherical capsule workspace, multiple jets must be actuated at once. The full workspace was explored using the custom test-bench of Fig. 2.7 and the system was programmed to follow a pre-planned path. The path consisted of the following steps: (1) starting from the free vertical position, one jet was throttled up until the full power was reached, then the capsule starts travelling around in a circle using combination of jets. The path continued by throttling up the second jet until the maximum power was reached while the first one was still active (2). Then, the first jet was decreased gradually to zero (3) and the same pattern was followed with the remaining jet until the capsule returned to the initial position (4).

By controlling the actuation force of each jet individually, the jets can produce a resultant motion in 2-DoF. As in the previous trial, three different tether lengths were tested, 12 cm 9 cm and 6 cm, and each one was restrained from rotating. The resulting capsule motion demonstrated maneuverability in a quasi-hemispherical workspace, and a bidimensional side view of the capsule workspace is given in Fig. 2.9. There are six peaks in Fig. 2.9 that correspond to the characteristic travelling motion of the HydroJet. They are due to the geometric location of the nozzles on the capsule. Once a second jet couples with an active jet, the capsule is pushed down and recovers the original height only when the two
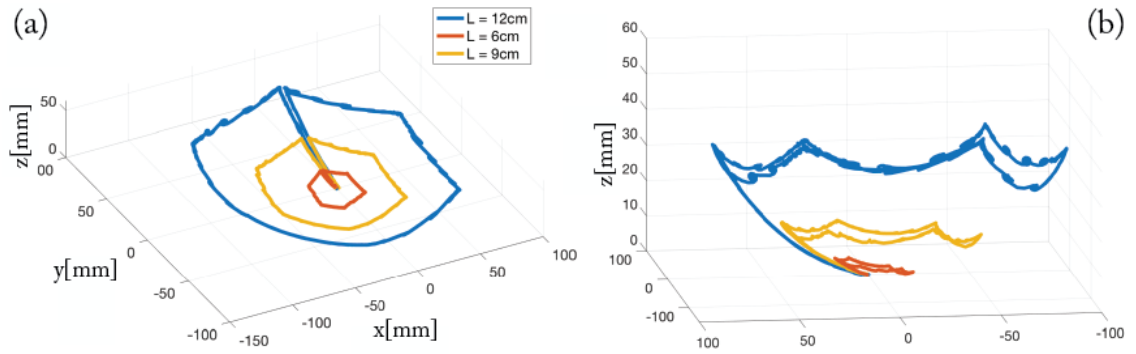
Figure 2.9: (a) Full semi-hemispherical workspace using different tether length (L) (Top View). (b) Full semi-hemispherical workspace using different tether length (L) (Lateral View).

jets provide an equivalent reaction thrust. The workspace shows repeatability and symmetry with respect to change in tether length. In addition, the capsule was able to return to the initial position after traveling along the path. The maximum lateral displacement recorded for the 12 cm tether was around 6 cm, corresponding to an equivalent hemispheric diameter of 12 cm, the same length as the tether.

2.5.3 Stomach Phantom Retroflexion Trial

To validate the feasibility of retroflexing the capsule within a confined space, an anatomically realistic human stomach phantom was used for this trial. The phantom, having the size of an average adult stomach (internal volume of 1000 cm3 [55]), was fabricated at Vanderbilt University Medical Center using a 3D mold from a human stomach CT scan reconstruction and a mixture of silicone rubbers (Dragonskin30 and Ecoflex10: 1-2 ratio, Smooth-On, USA) to match the original tissue properties. As briefly introduced before, retroflexion can be performed by advancing the tether further into the stomach while using the opposite wall of the cavity to deflect the movement (similar to the mechanics of retroflexion when using a traditional endoscope). The different phases of the procedure can be seen in Fig. 2.10. As illustrated, the capsule is initially directed toward the greater
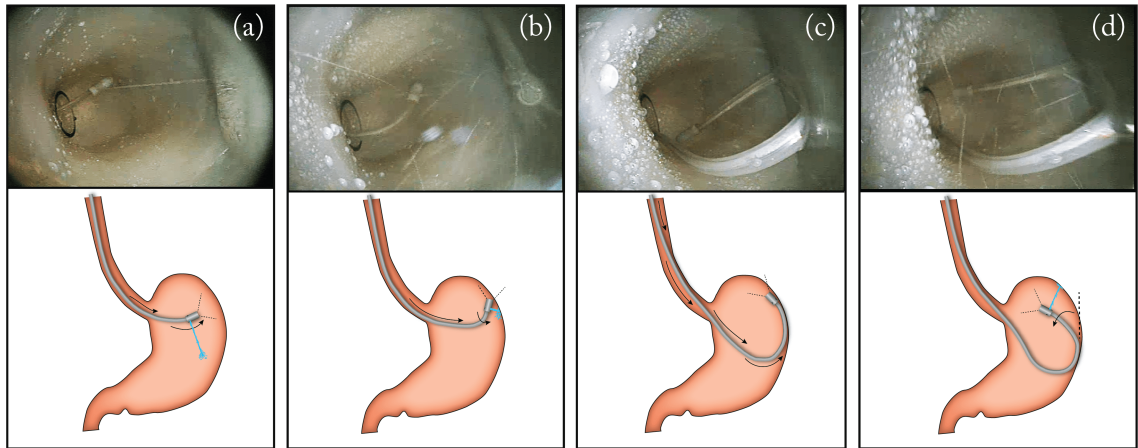
Figure 2.10: Different phases of a retroflexion maneuver.

curvature wall by throttling one jet (a). The operator, maintaining the same throttle, pushes the tether until the capsule hits the stomach wall (b). By looking at the image from the camera, the operator now uses the wall to pivot the capsule by controlling the amount of tether inserted (c). Once the capsule is lying against the wall, water jets are again used to complete retroflexion (d). During this set of trials, an expert endoscopist (attending physician who has performed more than 2,000 lifetime endoscopies) attempted retroflexion ten times with both the HydroJet and with a standard upper endoscope (Karl Storz, Tuttlingen, Germany). All trials were successful. The average time to perform the maneuver was 32 seconds with the HydroJet and 5 seconds with the flexible endoscope.

2.5.4 Comparative Trial

A bench top trial was performed to compare the controllability of the HydroJet with a traditional flexible endoscope (Storz, Model: Pediatric Gastroscope), shown side by side in Fig. 2.11. A small opaque bucket was used to simulate the workspace of the stomach, and 3 sets of 6 points were marked on the inner wall for visual identification. The sets were differentiated by using a shape designator, either a circle, star, or square. Trials were then conducted with 4 novice users and 1 expert user (attending with more than 1,000
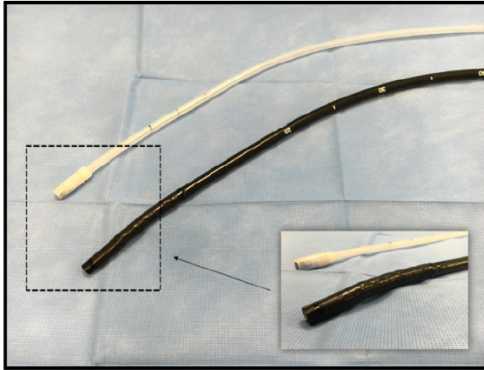
Novice	Endoscope	HydroJet
Total Time	5:42	8:24
Average Time	0:19	0:28
Standard Deviation	0:13	0:25
Expert		
Total Time	2:54	13:18
Average Time	0:10	0:44
Standard Deviation	0:06	1:11

Figure 2.11: Results of comparative trials between the HydroJet and a standard flexible endoscope. Total time refers to the cumulative time to complete all three trials with a given endoscopic device, while average time and standard deviation refer to the time needed to identify a single point. Time data given in minutes:seconds format.

lifetime endoscopies), in which each user identified and navigated to each point within the set of points. Each user conducted three trials with the gastroscope and three trials with the HydroJet, and the total time of the procedure and time between points were recorded. The sets of points and endoscopic device for each trial were chosen in a randomized order to prevent memory bias from affecting the results. The results of this trial are reported in Fig. 2.11 for both expert and novice users. With novice users, the HydroJet took approximately 50% longer than the flexible endoscope to complete a procedure. With the expert user, the difference between the HydroJet and flexible endoscope was much larger due to the users expertise in using traditional endoscopes. This time discrepancy is mainly due to the waterjets being directly controlled by the operator, and confirms that a modelling and control strategy, that allows to send motion comands with respect to the camera view, is required to achieve intuitive control of the device. Although the HydroJet takes longer than the flexible endoscope to complete a screening procedure, it still can provide screening care in a reasonable amount of time, and shows potential for improvement with operator training.

It is worth also comparing the optical capabilities of the HydroJet to that of the flexible endoscope to better understand the results. The endoscope used for comparison has a 140

deg field of view, and a focal distance of 2 mm-100 mm. In contrast, the camera used in the HydroJet has a 54 deg field of view and a focal distance of 10 mm - 50 mm. As such, the discrepancy in the quality of camera used in each device is expected to give the endoscope a baseline advantage, regardless of capsule controllability. Thus, these results can be considered to be a conservative estimate of the capabilities of the HydroJet. Of course, using a camera with a wider field of view would definitely reduce the time required to complete a procedure.

While these experiments showed that the inspection performed with the HydroJet tend to take a somewhat greater amount of time than those performed with a conventional endoscope, this increase in time is negligible in comparison with the amount of time a patient spends in a clinic or hospital for pre- and post-procedure care. A typical diagnostic procedure takes just 4-12 minutes, while the total time the patient spends with the medical staff is 60-120 minutes when sedation, recovery and discharge are included [56]. More importantly, the reduced cost of the HydroJet device stands to make gastric cancer screenings available to patients with little or no access to gastroscopies performed with conventional endoscopes. In addition, the disposable HydroJet represents a potential solution to the problem of inter-patient cross-contamination in settings where FEs are available but access to proper sterlization facilities are limited [37].

2.6   Conclusion

The HydroJet endoscopic platform addresses the need for a low cost, portable system for upper gastrointestinal cancer screening in LMIC. In this chapter, a novel water distribution system is introduced, which addresses many of the deficiencies of the previous design. Open-loop and throttle control of the actuating jets are examined and show good controllability of the reaction thrust. The range of stable positions the capsule can reach was further examined and is invariant on the tether length, depending only on the resolution of the pinch valve. This allows full controllability and stable spatial resolution with

differing tether lengths. Finally, comparative trials were conducted to evaluate the medical practicality of the platform.

Chapter 3

Modelling of Soft Continuum Manipulators Under Tip Follower Actuation

3.1 Introduction

The choice of modeling approach for modelling a specific manipulator, whether soft or hard, depends on a number of factors, including the mechanism of actuation, the significance of the effect of external loads like gravity, the required level of accuracy, and in some cases computation speed. The simplest modelling method for tendon-driven and pressurized chamber-actuated devices is the constant curvature (CC) model (see [57] for a review). This approximation is based on the assumption that each DoF is independent and the deflected shape can be modelled as a perfect circular arc. Depending on the robot design and the required level of accuracy for the application, this modelling approach may suffice. However, as the device stiffness decreases and deflection increases, accuracy of the CC approximation is typically reduced, making it unsuitable for many applications. An extension of the CC approximation is to discretize the manipulator into many short constant curvature sections, ([58], [59]). In this approach, finer discretization provide more accurate models, but also present many more parameters in need of calibration.

A Pseudo Rigid Body (PRB) approach [60] has been extensively used for describing the deflection of end-loaded beams [61, 62, 63]. An extension of the PRB approach, defined as Pseudo Rigid Body Chain (PRB-C), was introduced in [64]. In this approach the beam is divided into chain elements constituted of three superimposed pseudo-rigid-body models acting orthogonally in relation to each other [65]. This approach has been used for magnetically steered catheters [66, 67] and devices such as soft-tethered endoscopic capsules [68, 69], whose body is characterized by a passive flexible tether attached to a capsule experiencing a point wrench. These devices, proposed as an alternative to endoluminal endoscopes, provide access to remote surgical sites by entering the human body

via natural orifices. In [69], the device is steered within the colon through the application of a magnetic wrench on the capsule. For this application, the spatial configuration of the soft-tether is not modeled, and the forces generated by the presence of the tether are treated as an external disturbance to the pose of the capsule's body and compensated through the use of pose feedback. This has proven effective for motion in a closed lumen, where tissue interaction forces dominate over the loads applied on the capsule by the tether; however, when tip motion due to a TFA is controlled in free space, the forces applied on the capsule by the tether become relevant.

Nonlinear finite element analysis (FEA) has also proven useful for modeling the kinematics of soft continuum manipulators. In [70], the authors show that this method can accurately predict the displacement of a pressurized chamber-actuated soft continuum manipulator based on pre-computed strain maps for varying input pressures. However, this method proves to be highly sensitive to uncertainties in model parameters, as well as external disturbances, such as a change of the robot orientation with respect to gravity, making it challenging to apply this approach in a variety of practical applications.

Forward kinematic models based on Cosserat rod theory have emerged as some of the most accurate models available for continuum manipulators. This approach involves integrating the constitutive differential equations for a rod-type structure subject to certain boundary conditions, as described for soft pressurized chamber-actuated robots in [71]. Since Trivedi's work, Cosserat rod theory has been applied to tendon-actuated robots ([72]), concentric tube robots ([12], [11]), and elastic rods with permanent magnets at the tip subject to spatially varying magnetic fields ([73], [74]).

All of these modeling approaches include parameters which typically require calibration, including material properties and geometric/structural characteristics of the robot [75]. However, even after calibration of these parameters, kinematic accuracy may still be less than desired, due to unmodeled effects such as friction, nonlinear elastic and/or spatially varying material properties, and manufacturing imprecision.

One option for further improving kinematic accuracy is to incorporate some of these effects into the model. For example, for certain designs, researchers have integrated more complex, nonlinear constitutive laws within the models [76]. However, accurately determining these constitutive laws requires tedious material testing processes. Friction and manufacturing uncertainties can also be modeled in principle, but for many designs, these are extremely difficult to accurately describe in practice [77, 78]. In addition, incorporating these effects increases overall model complexity and can significantly increase the number of parameters, thereby requiring an even more complex calibration procedure.

Another approach to improving kinematic accuracy is to incorporate feedback from sensors. One of the most commonly used method is to embed strain sensors along the principal bending directions and then use the kinematic model to predict the shape of the manipulator based on strain measurement [79, 80]. This approach, however, is not suitable for all types of continuum manipulators, as these sensors do not scale down well to small designs and require precise alignment, complicating the fabrication process. Another common method is to use fiber optic shape sensors [81, 59]. However, this method begins to lose accuracy at high curvatures due to propagation losses, and cannot be implemented for many low-stiffness designs, as the fiber optic sensor is often stiffer than the manipulator itself. As an alternative which does not require any mechanical interaction between the robot and the sensors, much work has focused on reconstructing the shape from an external camera [82, 83]. The use of an external camera, however, can become problematic when direct visualization is limited by occlusions, such as during operation in a confined environment.

To address the previous limitations, a new method is presented to improve the accuracy of the kinematic model for CMs by utilizing sensory information from two inclinometers, one at the base of the manipulator and one at the tip. These sensors avoid the problem of occlusions associated with camera-based sensing modalities, while remaining compatible with low-stiffness CMs undergoing large deflections, as the sensors themselves do not need to bend with the structure of the CM. In addition, this type of sensor is inexpensive, making

36

it well-suited to cost-sensitive applications. Utilizing this sensor feedback, the approach presented in this chapter is to include a "disturbance" parameter in the model, which can compensate for a variety of unmodeled effects, and then calibrate this parameter in real time, based on the sensor data. The disturbance is in the form of an external point wrench, which is not meant to describe any particular external loads or actuation forces, both of which are considered separately within the CM modeling framework. The update of the disturbance can be performed by iteratively sensing the end effector's orientation through the inclinometers. Since the disturbance represents a set of additional model parameters, it is possible to numerically evaluate a sensitivity matrix that expresses how changes in the disturbance affect the end effector's angular velocity. The sensitivity matrix can then be inverted to update the disturbance estimate. This can then be applied back to the model, with the process being repeated iteratively to find a disturbance wrench that minimizes orientation error.

This chapter is organized as follows: first, the kinematic modeling of soft continuum manipulators under TFA is presented using both Pseudo Rigid Body Chain (PRB-C) Model and Cosserat Model approaches. These frameworks can account for non-constant curvature and out-of-plane bending which are two common effects in soft continuum manipulators under TFA. In addition, a disturbance parameter able to compensate for unmodeled effects such as friction, nonlinear elastic and/or spatially varying material properties is incorporated in both frameworks. Then, a procedure to improve the calibrated value of the disturbance parameter through sensor feedback is presented. Lastly, the proposed methods are applied to the HydroJet device, and show improvements in kinematic model accuracy in both modeling frameworks.
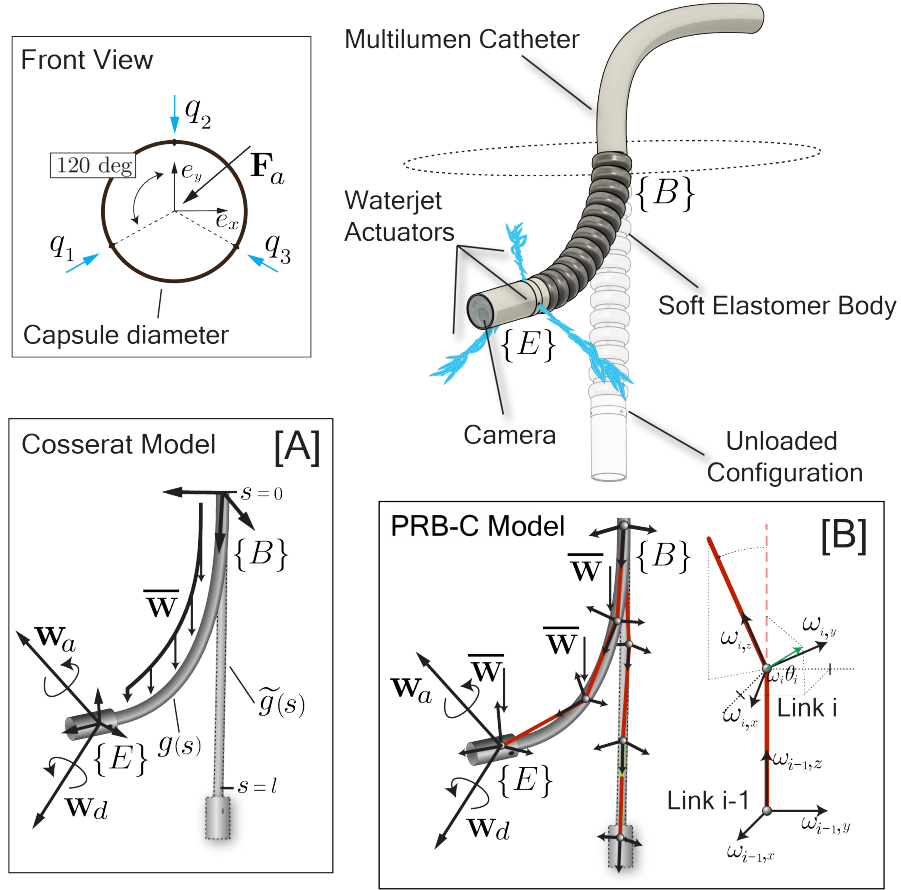
Figure 3.1: Mechanical deflection for the HydroJet endoscopic device expressed in both PRB-C and Cosserat frameworks. The waterjet actuators are spaced 120 degrees around the capsule diameter and modeled as a tip follower force.

3.2 Kinematic Modelling for TFA Soft Continuum Manipulators

3.2.1 PRB-C Kinematics

The PRB-C model is based on the approximation of subdividing the elastic body of the continuum manipulator into a series of rigid links connected by conventional revolute, universal, or spherical joints. In this case, the continuum structure is modeled as $n+1$ uniformly spaced rigid links connected by n spherical joints (Fig. 3.1 (B)) [67]. The rotation of each joint i with respect to the orientation of the previous joint $i-1$ is described using a rotation vector $\boldsymbol{\omega}_i \theta_i = \boldsymbol{\omega}_{ix} \theta_{ix} + \boldsymbol{\omega}_{iy} \theta_{iy} + \boldsymbol{\omega}_{iz} \theta_{iz}$, where $\boldsymbol{\omega}_{ix}$, $\boldsymbol{\omega}_{iy}$, $\boldsymbol{\omega}_{iz}$ are the three

orthonormal axes attached to the ith joint and θ_{ix}, θ_{iy}, θ_{iz} are the rotation angles around each axis. The resulting rotation axis and magnitude of rotation are indicated with ω_i and θ_i respectively. Considering that the magnitude and the direction of rotation of the ith joint can be calculated as $\phi_i = \|\theta_i\|$ and $\omega_i = \theta_i / \|\theta_i\|$, the corresponding twist, $\hat{\xi}_i \in se(3)$ results in:

$$\hat{\xi}_i = \begin{bmatrix} \hat{\omega}_i & \omega_i \times q_i \\ 0 & 0 \end{bmatrix} \tag{3.1}$$

where q_i is a vector pointing from the origin to any location on the axis ω_i, and $boldsymbol\hat{\omega}_i \in so(3)$ is the skew-symmetric matrix:

$$\hat{\omega}_i = \begin{bmatrix} 0 & -\omega_{iz} & \omega_{iy} \\ \omega_{iz} & 0 & -\omega_{ix} \\ -\omega_{iy} & \omega_{ix} & 0 \end{bmatrix}. \tag{3.2}$$

The homogeneous transformation matrix of each joint can be determined using the twists of equation 3.1, the rotation angle ϕ_i and the product of exponentials formula [84]:

$$g_{si}(\theta) = e^{\hat{\xi}_1 \phi_1} e^{\hat{\xi}_2 \phi_2} ... e^{\hat{\xi}_i \phi_i} g_{si}(0) \tag{3.3}$$

where $g_{si}(\theta) \in SE(3)$ is the configuration of joint i in the space frame for joint angles $\begin{bmatrix} \theta_1 & \theta_2 & ... & \theta_i \end{bmatrix}^T$ and $g_{si}(0)$ represents the initial configurations of joint i.

The relationship between the internal bending moment and deflection angle at each joint i can be modeled as:

$$\tau_i = K_i \omega_i \theta_i$$

$$= \begin{bmatrix} k_{i,x} & 0 & 0 \\ 0 & k_{i,y} & 0 \\ 0 & 0 & k_{i,z} \end{bmatrix} \begin{bmatrix} \omega_{ix}\theta_{ix} \\ \omega_{iy}\theta_{iy} \\ \omega_{iz}\theta_{iz} \end{bmatrix}. \tag{3.4}$$

where $\tau_i \in \mathbb{R}^3$ is a vector representing the internal bending moment and K_i is the stiffness matrix of joint i with components in x, y and z directions. The effective torsional spring constant can be found in terms of the elastic material properties by comparing spring energy and strain energy due to bending, as explained in [59]:

$$k_{i,x} = l_c/L \frac{2E_{L,x}I}{l_s} + (1 - l_c/L)\frac{2E_{0,x}I}{l_s} \tag{3.5}$$

where l_s is the length of the ith link, $l_c \in [0, L]$ is an incremental counter with l_s incre-ments, and E is varying along the length of the body, with $E_{0,x}$ and $E_{L,x}$ representing the Young's modulus of the joints i in the direction x at $l = 0$ and $l = L$, respectively. A similar expression can be found for y and z directions.

The Jacobian matrix can be calculated using [67, 84]:

$$J_{si}(\theta) = \begin{bmatrix} \xi_1^\dagger & \ldots & \xi_i^\dagger & 0 & \ldots & 0 \end{bmatrix} \tag{3.6}$$

where

$$\xi_1^\dagger = \begin{bmatrix} \xi_{i,x}^\dagger & \xi_{i,y}^\dagger & \xi_{i,z}^\dagger \end{bmatrix}$$

$$\xi_{i,j}^\dagger = Ad_{(e^{\xi_i \phi_i} \ldots e^{\xi_n \phi_n} g_{si}(0))}^{-1} \xi_{i,j} \tag{3.7}$$

The Jacobian for the end-effector can be expressed as:

$$J_{sn}(\boldsymbol{\theta}) = \begin{bmatrix} \xi_1^\dagger & \cdots & \xi_{n-1}^\dagger & \xi_n^\dagger \end{bmatrix}. \tag{3.8}$$

The mapping of forces applied on the body (i.e distributed loads and actuations) are modeled through the manipulator Jacobian. The effect of a distributed load on the body can be modeled as:

$$\tau_f = \sum_{i=1}^{n} J_{si}(\boldsymbol{\theta})^T \begin{bmatrix} \overline{\mathbf{w}} \\ \mathbf{0}_{3 \times 1} \end{bmatrix} \tag{3.9}$$

where $\overline{\mathbf{w}}$ represents a distributed force expressed in body frame at the ith joint. The effect of the actuators can be modeled as

$$\tau_a = J_{sn}(\boldsymbol{\theta})^T \begin{bmatrix} \mathbf{F}_a + \mathbf{w}_d|_f \\ \mathbf{M}_a + \mathbf{w}_d|_m \end{bmatrix} \tag{3.10}$$

where $\mathbf{F}_a$ represents force and $\mathbf{M}_a$ moment due to the actuators, $\mathbf{w}_d|_f$ represents the disturbance force at the tip and $\mathbf{w}_d|_m$ represents the disturbance wrench.

The quasi-static configuration of the soft continuum manipulator given external forces and moments as well as the TFA can be obtained in closed form using elliptic integrals [85, 86, 87]. In this work, the configuration vector θ is obtained by equalizing internal and external moments applied on the body using the chain algorithm as described in [88]. The solution to this equation cannot be obtained analytically, and is thus obtained through the following minimization:

$$\underset{\theta}{\text{minimize}} \quad K\omega(\boldsymbol{\theta}) - \tau_f(\boldsymbol{\theta}) - \tau_a(\boldsymbol{\theta}, \mathbf{q}) \tag{3.11}$$

The first term in the objective function is the internal moment due to the stiffness of the body, where $K\omega(\boldsymbol{\theta})$ is the internal bending moment of the whole body. The second and third terms represent the external moments acting on the body, which are related to the

configuration vector θ through the manipulator Jacobian, and **q** represents the actuation forces (e.g. forces applied by the water jets). The SLSQP method is used to solve the minimization problem.

3.2.2   Cosserat Rod Kinematics

Based on Cosserat rod theory, a deflection model for continuum manipulators with configuration space parameters **q**, and under a six DoF follower wrench **w**, can be written in the following form ([89]; [12]):

$$
\begin{aligned}
g'(s) &= g(s)\hat{\boldsymbol{\xi}}(\mathbf{y}) \\
\mathbf{y}'(s) &= \mathbf{f}(s, \mathbf{y}, g, \mathbf{q}, \mathbf{w})
\end{aligned}
\tag{3.12}
$$

where $g(s) \in SE(3)$ describes the homogeneous transformation defining the position and orientation of an arc-length parameterized reference frame along the arc coordinate s (Figure 3.2), $\hat{\boldsymbol{\xi}} \in se(3)$ is a body frame twist describing how g evolves in s ([84]), and the operator $'$ denotes a derivative with respect to s. A set of variables **y** describe the equilibrium equations governing the behavior of the manipulator.

Solving for the deflection of a generic soft continuum manipulator requires the knowledge of a subset of elements of **y** that is usually in the form of boundary conditions at the base ($s = 0$) and at the tip ($s = l$). These may be expressed in the form of [90], with the conditions at the base being:

$$
\begin{aligned}
g(0) &= H(\mathbf{y_u}(0), \mathbf{q}, \mathbf{w}) \\
\mathbf{y_k}(0) &= \Pi(\mathbf{y_u}(0), \mathbf{q}, \mathbf{w})
\end{aligned}
\tag{3.13}
$$

where $\mathbf{y}_u$ represents a set of unknown elements of **y** and $\mathbf{y}_k$ represents a known set of conditions at $s = 0$. Similarly, at the tip of the robot ($s = l$) the boundary conditions assume a more general form:
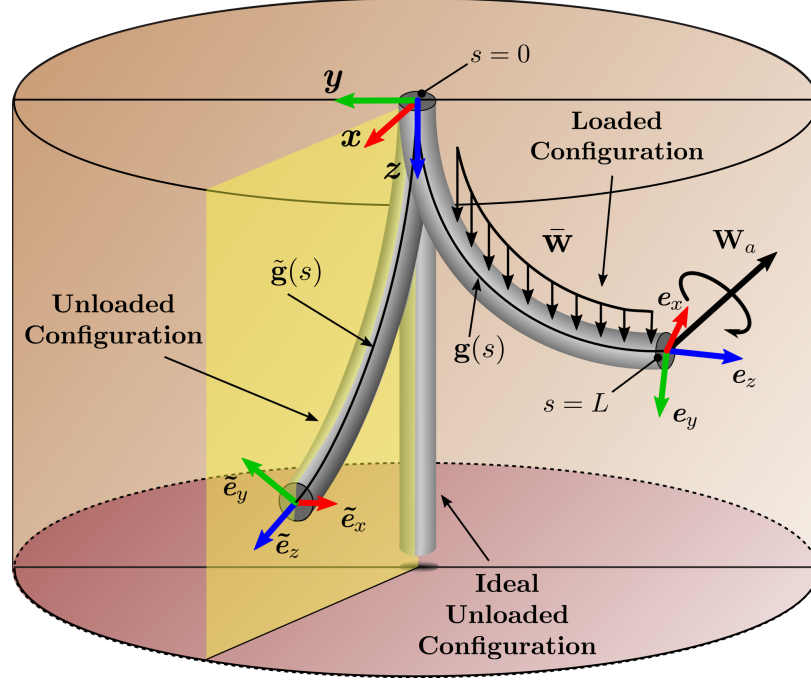
Figure 3.2: Soft continuum manipulator spatial configurations using the Cosserat model approach. In the ideal unloaded configuration the rod is perfectly straight. The unloaded configuration is pre-curved due to the existence of internal strain. The loaded configuration shows the rod bending under distributed and point loads.

$$\boldsymbol{\Gamma}(\mathbf{y}(l), g(l), \mathbf{q}, \mathbf{w}) = \mathbf{0} \tag{3.14}$$

Equation (3.14) is in a generic form and may account for multiple connected continuum elements, each with different properties. Assuming a single continuum element whose spatial configuration can only be altered through the application of a follower wrench, as in Figure 3.2, the boundary conditions can be simplified to:

$$g(0) = H(\mathbf{y_u}(0), \mathbf{w}^*)$$
$$\mathbf{y_k}(0) = \boldsymbol{\Pi}(\mathbf{y_u}(0), \mathbf{w}^*) \tag{3.15}$$
$$\boldsymbol{\Gamma}(\mathbf{y}(l), g(l), \mathbf{w}^*) = \mathbf{0}$$

where $\mathbf{w}^* = \mathbf{w}_a(\mathbf{q}) + \overline{\mathbf{w}}$ represents the effect from both a time-varying localized wrench which is a function of the joint parameters, $\mathbf{w}_a(\mathbf{q})$, and an external constant wrench $\overline{\mathbf{w}}$, e.g.

gravity. By integrating equations (3.12) using the boundary conditions (3.15) (i.e solving the forward kinematic model), it is possible to estimate the deflection of the rod caused by a wrench applied at a specific location along its body. The solution of the forward kinematic model represents a geometric configuration in which all forces and moments applied on the body are in equilibrium. In order to accurately control tip motion with a soft structure, it is advantageous to apply a wrench in close proximity to the tip while constraining the base. A schematic representation of a soft continuum manipulator under these constraints is presented in Figure 3.2, and the associated boundary conditions can be expressed as:

$$
\begin{aligned}
g(0) &= g_0 \\
\mathbf{y_k}(0) &= \Pi(\mathbf{y_u}(0)) \\
\Gamma(\mathbf{y}(l), g(l), \mathbf{w}_a(\mathbf{q}), \overline{\mathbf{w}}(l)) &= \mathbf{0}
\end{aligned}
\tag{3.16}
$$

where it is assumed that the deformation of the soft body is caused exclusively by a wrench $\mathbf{w}_a$ generated by the actuators and a tip load $\overline{\mathbf{w}}(l)$. The next section presents the static equations describing the equilibrium of the rod under the boundary conditions (3.16).

3.2.2.1 Derivation of Cosserat-Rod Kinematic Model for TFA Soft Manipulators

As introduced in [91], the centerline of an unloaded precurved rod can be described by an arc-length parameterized space curve $\widetilde{\mathbf{p}}(s) \in \mathbb{R}^3$, expressed with respect to a base coordinate frame attached at the proximal end of the rod. A frame is assigned to each point on the rod $\widetilde{\mathbf{p}}(s)$, with the orientation of the frame represented by a rotation matrix $\widetilde{R}(s)$ corresponding to the rotation of the base frame unit vectors $\begin{bmatrix} \widetilde{\mathbf{e}}_x & \widetilde{\mathbf{e}}_y & \widetilde{\mathbf{e}}_z \end{bmatrix}^T$. Under an external load, the parametric curve $\widetilde{\mathbf{p}}(s)$ deflects to the curve $\mathbf{p}(s)$ and $\widetilde{R}(s)$ rotates to $R(s)$. The homogeneous frames are assigned so that the z-axis of each frame is tangent to the curve. By differentiating the arc-length parameterized curve with respect to the parameter s, we obtain:

$$\mathbf{p}'(s) = \mathbf{e}_z \tag{3.17}$$

where $\mathbf{e}_z = R(s)\mathbf{k}$, and $\mathbf{k} = \begin{bmatrix} 0 & 0 & 1 \end{bmatrix}^T$ is the versor associated with the z-axis of the base coordinate frame. The continuous homogeneous transformation for the deflected rod may be defined as:

$$g(s) = \begin{bmatrix} R(s) & \mathbf{p}(s) \\ \mathbf{0}^T & 1 \end{bmatrix}. \tag{3.18}$$

A similar expression may also be defined for the initial state $\widetilde{g}(s)$. The rotation of each point on the rod may be expressed in terms of a local curvature vector $\mathbf{u}(s)$, which can be found using the relationship [84]:

$$\mathbf{u}(s) = (R^T(s)R'(s))^\vee \tag{3.19}$$

where the operator $^\vee$ denotes conversion of an element of $\mathfrak{so}(3)$ to its corresponding element in $\mathbb{R}^3$. The curvature at each material point with respect to the initial state $\widetilde{\mathbf{u}}(s)$ represents the local strains within the rod, and can be obtained using $\triangle\mathbf{u}(s) = \mathbf{u}(s) - \widetilde{\mathbf{u}}(s)$. The constitutive relationship between the curvature vector and internal moments, expressed in the local coordinate frame at s, is:

$$\mathbf{M}_b(s) = K(s)(\mathbf{u}(s) - \widetilde{\mathbf{u}}(s)) \tag{3.20}$$

where $\mathbf{M}_b(s)$ is the internal moment and K represents the stiffness matrix, defined as:

$$K(s) = \begin{bmatrix} E(s)I_x(s) & 0 & 0 \\ 0 & E(s)I_y(s) & 0 \\ 0 & 0 & G(s)J(s) \end{bmatrix} \tag{3.21}$$

where E is the Young's modulus, I_x and I_y are the second moment of area of the tube cross-section, G is the shear modulus and J is the polar moment of inertia of the tube cross-section. The equilibrium equations for the rod under external forces and moments were derived following a similar process to that described in [12]. The resulting equations that govern the distribution of forces and moments along the rod can be expressed as:

$$\mathbf{Q}'(s) + \overline{\mathbf{w}}(s) + \mathbf{P}\delta(s-l) = 0$$
$$\mathbf{M}'(s) + \overline{\mathbf{m}}(s) + \mathbf{p}'(s) \times \mathbf{Q}(s) = 0 \tag{3.22}$$

where $\mathbf{Q}(s)$ is the internal force, $\mathbf{M}(s)$ is the internal moment, $\overline{\mathbf{w}}(s)$ represents the distributed force, $\overline{\mathbf{m}}(s)$ represents the distributed moment along the rod and $\mathbf{P}\delta(s-l)$ represents the concentrated force due to the tip concentrated mass at $s = l$. Since the follower wrench is geometrically located at the tip of the manipulator, remaining always fixed with respect to the tip frame, it is convenient to express equations (3.22) with respect to the local coordinate frame. Thus,

$$\mathbf{Q}'_b(s) = -\hat{\mathbf{u}}\mathbf{Q}_b(s) - \overline{\mathbf{w}}_b(s) - \mathbf{P}_b\delta(s-l)$$
$$\mathbf{M}'_b(s) = -\hat{\mathbf{u}}\mathbf{M}_b(s) - \overline{\mathbf{m}}_b(s) - \hat{\mathbf{e}}_z\mathbf{Q}_b(s) \tag{3.23}$$

where $\overline{\mathbf{w}}_b(s) = R(s)^T\overline{\mathbf{w}}(s)$, $\mathbf{P}_b = R(s)^T\mathbf{P}$ and $\hat{\mathbf{e}}_z$ is the skew-symmetric matrix associated with the vector $\mathbf{e}_z$. The effect of both the distributed force and of the weight at the tip can be easily estimated by knowing the orientation of the base and tip frames with respect to a global frame aligned with gravity:

$$\overline{\mathbf{w}}(s) = R_g \begin{bmatrix} 0 \\ 0 \\ -m_b(s)g \end{bmatrix}$$

$$\mathbf{P} = R_g \begin{bmatrix} 0 \\ 0 \\ -m_t g \end{bmatrix} \tag{3.24}$$

where m_t is the total concentrated mass at the tip and m_b is the distributed mass of the body and R_g represents the rotation of the base frame with respect to gravity. Substituting (3.20) in (3.23) and then solving for $\mathbf{u}'$ yields

$$\mathbf{u}'(s) = \widetilde{\mathbf{u}}'(s) - K^{-1}\Big((\hat{\mathbf{u}}K + K')(\mathbf{u}(s) - \widetilde{\mathbf{u}}(s)) \\ + \overline{\mathbf{m}}_b(s) + \hat{\mathbf{e}}_z \mathbf{Q}_b(s) \Big) \tag{3.25}$$

Equations (3.17), (3.20), (3.23) and (3.25) represent the model equations that need to be integrated from $s = 0$ to $s = l$ in order to determine the state variables $\begin{bmatrix} \mathbf{p}(s) & R(s) & \mathbf{u}(s) & \mathbf{Q}_b(s) \end{bmatrix}$ in the form expressed by (3.12). A summary of the Cosserat rod equations that govern the rod shape expressed in local frame coordinates are:

$$g'(s) = g(s)\hat{\xi}(s)$$

$$\mathbf{Q}_b'(s) = -\hat{\mathbf{u}}\mathbf{Q}_b(s) - \overline{\mathbf{w}}_b(s)$$

$$\mathbf{u}'(s) = \widetilde{\mathbf{u}}'(s) - K^{-1}\Big((\hat{\mathbf{u}}K + K')(\mathbf{u}(s) - \widetilde{\mathbf{u}}(s)) \\ + \hat{\mathbf{e}}_z \mathbf{Q}_b(s) \Big) \tag{3.26}$$

where $\mathbf{Q}_b$ is the internal force, $\overline{\mathbf{w}}_b$ is the distributed force and $\hat{\mathbf{u}}$ and $\hat{\mathbf{e}}_z$ are the skew-symmetric versions of vectors $\mathbf{e}_z$ and $\mathbf{u}$, respectively. In the previous equations we have ignored the contribution of distributed moments along the body.

To allow the body to bend sharply as the arch length parameter s increases, the Young's modulus is considered to be linearly varying along the length of the body going from a value E_0 at the base to E_l at the tip following the equations: $E(s) = sE_l + (1-s)E_0$ and $G(s) = E/2\gamma$. Boundary conditions for systems constrained at the base with TFA are expressed with respect to the proximal and distal ends of the soft body. Therefore, at $s = 0$, the position of the rod and the rotation of the attached frame at its base are defined respectively as:

$$
\begin{aligned}
\mathbf{p}(0) &= \begin{bmatrix} 0 & 0 & 0 \end{bmatrix}^T. \\
R(0) &= R_g
\end{aligned}
\tag{3.27}
$$

The boundary condition applied to the distal tip contains the discrete point wrench generated by the actuators, $\mathbf{w}_a$. The generic form for this boundary expression is:

$$
\begin{aligned}
\mathbf{Q}_b(l) - \mathbf{w}_a|_f - \mathbf{w}_d|_f &= \mathbf{0} \\
\mathbf{u}(l) - \widetilde{\mathbf{u}}(l) &= K^{-1}(\mathbf{w}_a|_m + \mathbf{w}_d|_m)
\end{aligned}
\tag{3.28}
$$

where $\mathbf{w}_a|_f$ and $\mathbf{w}_a|_m$ respectively represent the force and the moment components of the follower wrench generated by the actuators expressed with respect to the tip frame and $\mathbf{w}_d|_f$ and $\mathbf{w}_d|_m$ the contribution of the disturbance force and moment, respectively.

3.3 Disturbance Estimation Approach

This section describes the estimation procedure used to find a disturbance wrench which minimizes the tip rotation error associated with the kinematics. This problem is approached by first calibrating geometric and material properties of the manipulator with the additional disturbance wrench parameter to find a solution for the manipulator parameters which is
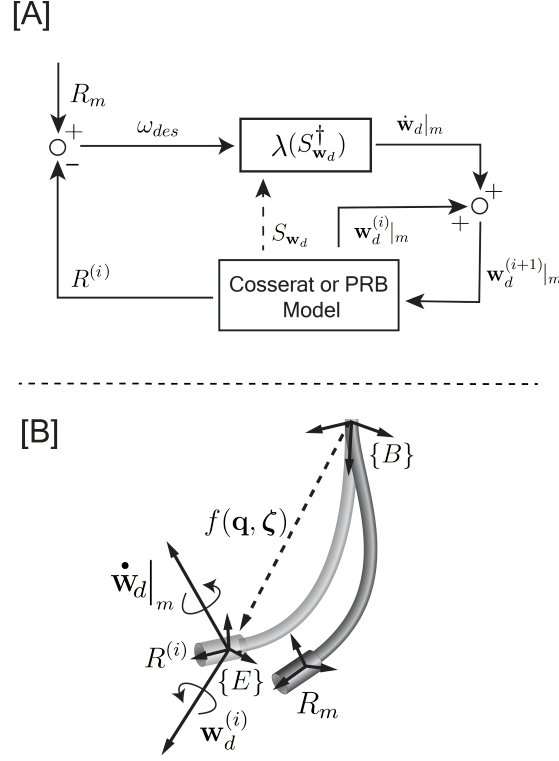
Figure 3.3: Iterative disturbance estimation algorithm. [A] Block Diagram illustrating the iterative update of the disturbance based on inclinometer data. The initial value for $\mathbf{w}_d^{(i)}$ is obtained after initial calibration. [B] The compliance matrix $S_{\mathbf{w}_d}$ is used to minimize the orientation error between current estimated orientation $R^{(i)}$ and the measured value from the sensors R_m.

optimal across the initial calibration data set. Then, during robot operation, the calibrated value of the tip disturbance is iteratively changed by using sensory information to minimize the orientation error at the current position within the workspace.

The disturbance estimation approach is described by first assuming a general kinematic model for continuum robot which can be expressed in the form:

$$g = f(\mathbf{q}, \zeta) \tag{3.29}$$

where g represents the pose of the end effector as a function of the actuation inputs $\mathbf{q}$, and a set of manipulator's parameters $\zeta = \begin{bmatrix} \eta & \mathbf{w}_d \end{bmatrix}^T$ composed by geometric and mate-

rial properties of the manipulator η, (such as length, Young's Modulus, etc.), and by the disturbance wrench $\mathbf{w}_d$. The nominal mapping between end effector pose and actuator inputs can be used to calibrate the manipulator's parameters by using the scalar product of end effector absolute orientations as the error metric [92]. After calibration, the resulting parameters (indicated as ζ^*) are used to estimate the equilibrium pose of the end effector that corresponds to the inputs $\mathbf{q}$.

3.3.1 Iterative Disturbance Estimation

The sensing of absolute orientations can help to correct the rotation error iteratively through the use of the sensitivity matrix:

$$S_{\zeta^*} = (g^{-1} \frac{\partial g}{\partial \zeta^*})^{\vee} \tag{3.30}$$

which maps body frame end-effector velocities to changes in the manipulator's calibrated parameters ζ^*. Independent of which kinematic modelling approach is used, the sensitivity matrix can be computed numerically using a finite difference approximation [90]. Each column can be computed as:

$$S_j \approx (g^{-1} \frac{g_j - g}{\Delta \zeta_i})^{\vee} \tag{3.31}$$

where g_j is the homogeneous transformation describing the end effector pose obtained after perturbing g with a small change in the ith calibrated parameter by $\Delta \zeta_i$. Using this method, each column of the sensitivity matrix can be obtained after 2 solutions of the kinematic equations.

The rotation error is iteratively minimized by using a gradient descent approach where the change in the disturbance wrench $\dot{\mathbf{w}}_d|_m$ is calculated by:

$$\dot{\mathbf{w}}_d|_m = \lambda \left(S_{\mathbf{w}_d}^T (S_{\mathbf{w}_d} S_{\mathbf{w}_d}^T - \mu \mathbf{I}_3)^{-1} \right) \omega_{des} \tag{3.32}$$

where $S_{\mathbf{w}_d}$ represents the columns of the sensitivity matrix which map changes in the disturbance parameter to changes in the tip orientation, ω_{des} can be calculated by using the orientation error between the current estimated rotation R^i and the measured value from the sensors R_m expressed in body coordinate, λ represent a gain correction coefficient which can be experimentally tuned using the calibration dataset, μ is a damping factor and $\mathbf{I}_3$ is the identity matrix (Fig. 3.2). The calculated change can then be added to the previously estimated value of the disturbance and applied to the model $\mathbf{w}_d^{(i+1)} = \mathbf{w}_d^{(i)} + \dot{\mathbf{w}}_d$ where $\dot{\mathbf{w}}_d = \begin{bmatrix} \dot{\mathbf{w}}_d|_f & \dot{\mathbf{w}}_d|_m \end{bmatrix}^T$ and $\dot{\mathbf{w}}_d|_f = \mathbf{0}$.

3.4 Experimental Validation

3.4.1 HydroJet System Testbed

The testbed was assembled as depicted in Fig. 4.4. The capsule was manufactured from a durable plastic (Clear resin, FormLabs, Sommerville, MA, USA) through rapid prototyping. The capsule's outer diameter and length are 9.8 mm and 28 mm, respectively. A 6 DoF electromagnetic sensor (EM) (Northern Digital Inc., Canada) was integrated within the capsule, with its frame aligned to the capsule in a known orientation. The wire of the electromagnetic sensor runs through the soft elastomer sleeve together with the three single-lumen water lines connecting the tip to the base connector. The base was connected to three solenoid water valves (A352273, Asco Numatics, USA) using standard hydraulic tubing (1/16"ID X 1/8"OD Tygon E-3603, Cole-Parmer, USA). The base connector was held in the desired orientation using a custom 3D printed holder. The assembly was secured in place through attachment to an aluminum frame (Rexroth, Bosch, Germany). A second 6-DoF EM sensor was attached to the base holder to sense the orientation of this frame as well and compute the direction of gravity with respect to the capsule and tether.

3.4.2   Initial Calibration

The purpose of calibration is to find values for the parameters of the model that best describe the deflection of the manipulator for a set of N poses distributed throughout the workspace of the manipulator. This means that the intrinsic parameters found during calibration may not be the optimal for a single actuation value. The parameters of both models are optimized such that the rotation at the tip and at the base closely approximate those of the experimental data under the same set of actuations. In these experiments, the data used for calibration consist of a set of 40 randomly distributed equilibrium configurations within the workspace. The parameter optimization problem is defined as follows:

$$\underset{\zeta}{\text{minimize}} \quad \sum_{i=1}^{40} ||(< \mathbf{h}_m(\mathbf{q}_i, \zeta), \mathbf{h}_i >)||^2 \qquad (3.33)$$

where $\mathbf{h}_m = a + b\mathbf{i} + c\mathbf{j} + d\mathbf{k}$ represents the quaternion associated with the rotation of the tip with respect to the base, as computed by solving for the equilibrium configuration (eq. (3.11) for the PRB-C model and eqs. (3.26), (4.9), (3.27) for the Cosserat model) with inputs $\mathbf{q}_i$ and manipulator parameters ζ. Similarly, $\mathbf{h}_i$ represents the quaternion associated with the measured experimental rotation, which is obtained by calculating the relative rotations of the two inclinometer sensors. The operator $< \cdot >$ represents the scalar product of two vectors and is chosen as the distance metric between two elements of SO(3) [92].

Assuming the soft elastomer body to have a cylindrical shape with radially isotropic properties results in $E_{L,x} = E_{L,y} = E_L$, $E_{0,x} = E_{0,y} = E_0$ and $G_L = E_L/2\gamma$ and $G_0 = E_0/2\gamma$, where γ is the Poisson's ratio. The manipulator's parameters that we seek to calibrate are then $\zeta = \begin{bmatrix} E_0 & E_l & L & \mathbf{w}_d \end{bmatrix}^T$. The results of calibration using both models are summarized in Table 4.1.
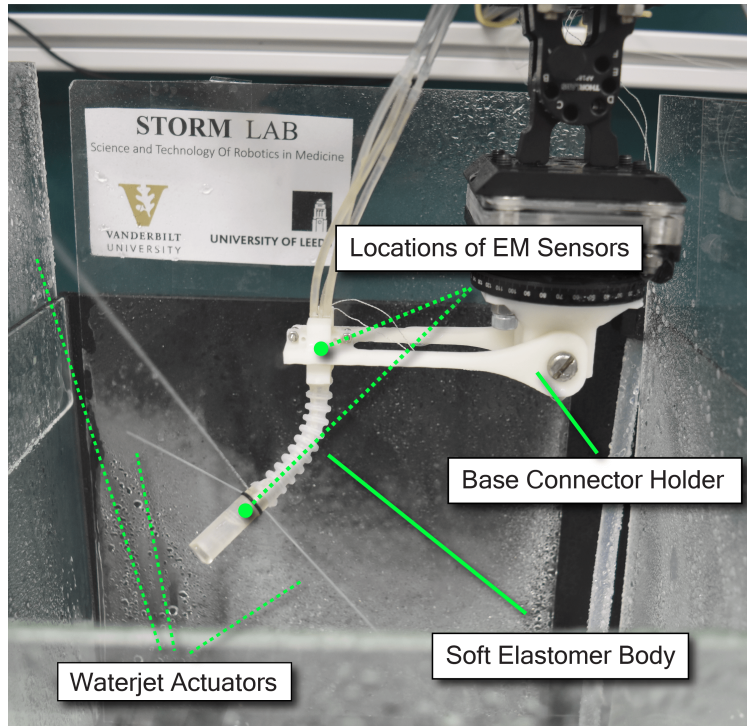
Figure 3.4: Experimental bench test setup consisting of the Hydrojet Endoscopic Device. A 3D printed holder anchors the base of the device while the waterjets at the tip cause deflection of the soft elastomer body.

3.4.3 Constant Disturbance Results

The optimal value for the manipulator parameters ζ^* was obtained for both PRB-C and Cosserat models using the calibration procedure described in the previous section. To validate the accuracy of both models after calibration, the soft manipulator was moved throughout its workspace by gradually increasing the actuation force of one waterjet at a time until the maximum force was reached. This resulted in three sweeping motions, shown in different colors in Fig. 3.5. During this motion, the orientations of the base and the tip of the manipulator were recorded through the EM sensors. The force generated by the waterjet was directly controlled by input signals to the solenoid valves. To facilitate quasi-static motion, each command was sent with a delay of 5 seconds, which is higher than the settling time of the body to its equilibrium. The sweeping motion corresponding
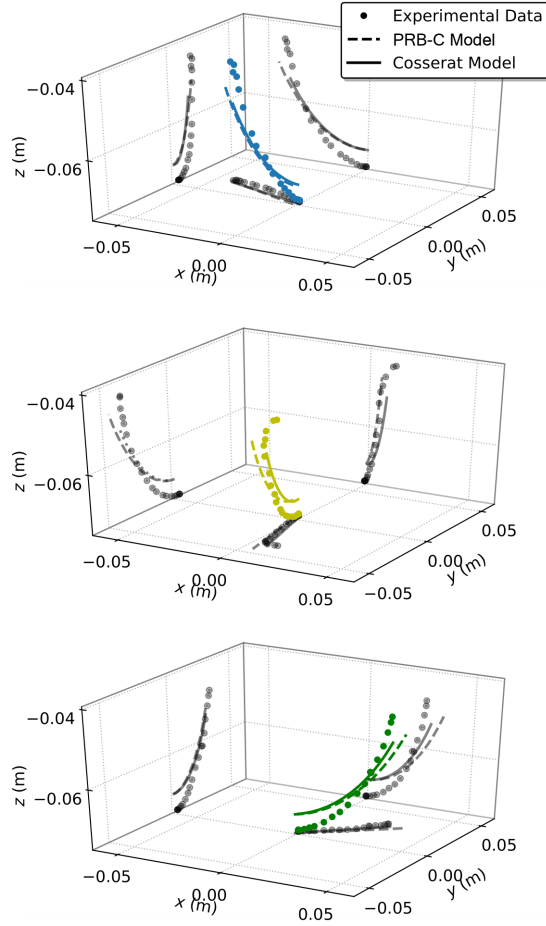
Figure 3.5: Experimental validation of the calibrated coefficient ζ^*. Each sweep is marked with a different color. The experimental deflection (dots) is projected on *xy*, *xz*, *yz* planes together with the corresponding position estimated from both PRB-C (black dashed line) and Cosserat (black continuous line) frameworks.

to each of the three jets was repeated three times, for a resulting total of nine separate motions. For each actuation force, each model was evaluated with the parameters obtained during calibration (ζ^*) to compute the end-effector pose. The results are shown in Figs. 3.5 and 3.6. The position error ($||\varepsilon||_2$) is defined as the Euclidean norm of the difference between model-predicted tip position and measured tip position obtained from the EM sensors, while the rotation error $\Delta\psi$ is calculated as in section 3.4.2. To enable similar discretization of the body of the manipulator for both frameworks, the length of the links for the PRB-C model was chosen to be the same as the integration step size used for the
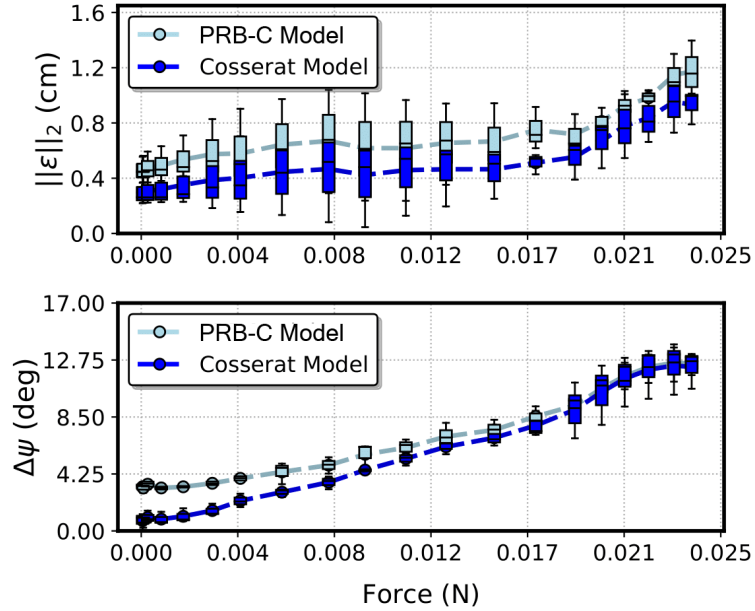
Figure 3.6: Box Plot Comparison of PRB-C and Cosserat Models. Position and orientation errors with constant disturbance wrench.

Cosserat model. The root-mean-square (RMS) and standard deviation (SD) position and orientation error resulting from the nine sweeps was 0.69 cm $\pm$ 0.20 cm with 6.85 deg $\pm$ 3.41 deg for the PRB-C and 0.51 cm $\pm$ 0.20 cm with 5.66 deg $\pm$ 4.21deg for the Cosserat model, showing similar behavior of the two modelling frameworks.

3.4.4 Iterative Disturbance Estimation Results

The same sweeping motions described in the previous section were used with online adjustment of the disturbance wrench based on sensor orientation. The disturbance wrench was iteratively adjusted following the gradient descent minimization approach described in Section 3.31 using a gain correction coefficient of $\lambda = 0.4$. The local minimum was generally reached after one to two iterations per time step. Results are shown in Fig. 3.7. Compared to the constant disturbance approach, the iterative estimation reduces the orientation error by 43%, going from an average error of 6.85 deg to 3.96 deg in the case of

Table 3.1: RMSE Position and Orientation of Iterative Disturbance Estimation compared to Standard Geometric Calibration

	Bending Angle		10°	25°	50°	75°
PRB-C Model	Position RMSE (cm)	Ref.	0.44	0.75	1.16	1.34
		Proposed.	0.66	0.69	0.74	0.79
	Orientation RMSE (deg)	Ref.	9.06	9.89	10.02	10.75
		Proposed.	1.74	3.18	5.18	7.07
Cosserat Model	Position RMSE (cm)	Ref.	0.52	0.78	1.01	1.25
		Proposed.	0.37	0.47	0.56	0.75
	Orientation RMSE (deg)	Ref.	9.17	9.81	9.27	10.04
		Proposed.	0.82	2.46	3.96	7.18

PRB-C model, and by 42%, from 5.66 deg to 3.29 deg for the Cosserat model. While the error in orientation is significantly reduced, there is no significant variation in positional error, which remains confined within the same range of the values observed for the PRB-C model without online disturbance estimation, and is slightly improved for the Cosserat model.

In Table 3.1, the RMS errors calculated using the iterative estimation method (Proposed.) are compared to the standard geometric calibration (Ref.). The proposed method significantly improves both positional and orientation error over the standard calibration method showing 42% positional error reduction and 32% orientation error reduction for 75° deflection of the end effector.

3.5 Discussion

In this chapter, a new method for using sensory feedback from orientation sensors to improve the kinematic modeling accuracy for continuum manipulators is presented. This
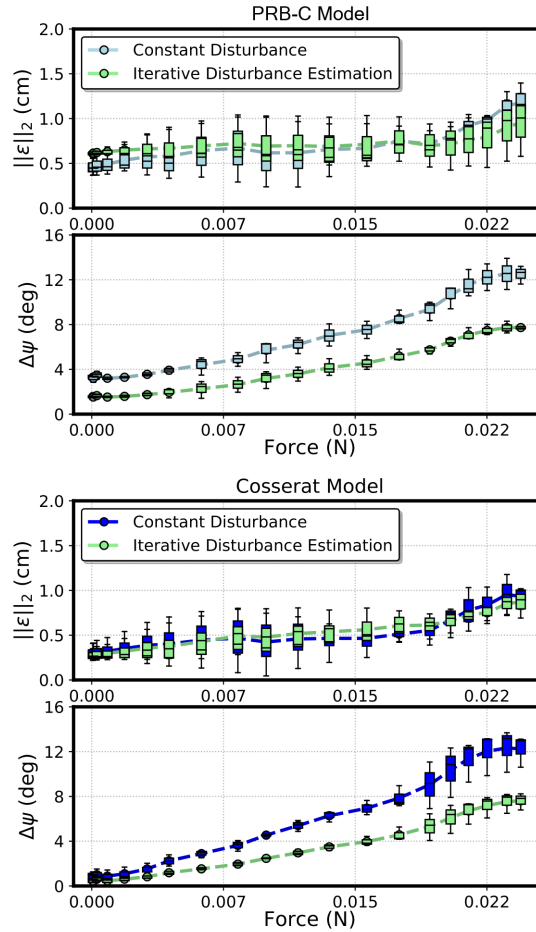
Figure 3.7: Box plot showing error distribution and variability over the nine sweeping motions. The iterative estimation of the disturbance wrench using sensor data allows for significant reduction in the rotation error for both modelling frameworks.

is achieved by incorporating a "disturbance wrench" to account for unmodeled phenomena, which is continually updated based on the sensor data. Future work will focus on the integration of this method into a Jacobian-based motion controller; the improved modeling accuracy demonstrated in this work is expected to improve trajectory following abilities as well. The improved modeling and control accuracy which this approach can enable is expected to be highly valuable, as improving kinematic modelling accuracy is still a very active area of research for CMs in particular. For the HydroJet System, this improved accuracy will enable medical providers to more precisely control the device within the stomach during upper gastrointestinal endoscopy. As a result, this highly cost-effective system may

also prove easier to use than conventional endoscopes, facilitating its widespread use in resource-limited settings. It is expected that this approach could provide similar benefits for a wide range of soft robotics applications, both in and outside of the medical field. EM sensors are used in this chapter to calculate absolute orientations, however these sensors can be replaced by inertial motion units (IMUs) without changing the proposed disturbance estimation method. Absolute orientation can be obtained from IMUs through an orientation filter as the one proposed in [93].

3.6   Conclusion

This chapter presents two modelling approach for TFA soft manipulators and a method for augmenting the kinematic models for continuum manipulators with information from orientation sensors in order to improve model accuracy. The method is based on online calibration of a "disturbance wrench" used to account for various unmodeled phenomena. This method is applied in particular to a soft continuum manipulators actuated by a tip follower wrench and experiencing external loading, and demonstrated that the method is effective in improving kinematic model accuracy for both PRB-C and Cosserat rod modeling frameworks.

Chapter 4

Closed-loop Control of Soft Continuum Manipulators Under Tip Follower Actuation

4.1   Introduction

The choice of a control approach for CM depends on factors such as: the mechanism of actuation, the significance of the effect of external loads like gravity, the required level of accuracy, and computation speed. Model-based static controllers are currently the most widely used and studied strategy for control of continuum robots. While the majority of model-based controllers rely on the CC approximation, this assumption breaks down when out of plane bending occurs, whether due to the actuation itself, such as in the case of non-linear tendon-routing, or due to external loads, such as those due to gravity ([72]).

Control methods based on the Cosserat framework have emerged thanks to their ability to easily incorporate more complex effects such as: varying longitudinal stiffness, non-linear constitutive behaviour and effects of various loading on the continuum structure. While Cosserat rod theory can be directly adapted to compute forward kinematics of these manipulators, it typically does not allow for direct inversion. Instead, a differential kinematics approach is typically used, in which the Jacobian matrix is used to map desired task space velocities into desired actuator space velocities. This forward kinematic model and resolved rates approach has proven effective, even without pose feedback, for continuum robots [94], [95], [96]. However, many of the simplifying assumptions used to make calibration and real-time control via this model feasible (such as linear elastic materials, uniform precurvature, and uniform and isotropic material properties) do not hold up well for soft elastomeric manipulators. Challenges arise when applying the resolved rates approach to continuum robots as the stiffness becomes extremely low, such that the singular values in the Jacobian matrix mapping tip wrenches to tip motion are very large. This implies

that for soft robots, small changes in actuation forces can result in very large changes in manipulator pose. As a result, effective control of the robot's task space requires extremely precise control of the actuator space, which may be difficult to achieve for certain TFA designs, depending on the mechanism used to generate the tip wrench. For example, in the case of the HydroJet, the system used to deliver water through the jets possesses its own nonlinear dynamics, making it difficult to accurately control flow rate without actuation feedback.

Alternatively, model-less controllers have been presented and applied to CM morphologies [97, 98, 99]. These methods rely on sensor data to build arbitrarily complex kinematic models that can accommodate for highly non-linear systems that are too complex to describe with traditional deflection models. In [100] the CM configuration is calibrated using a vision system. In [101], camera feedback is incorporated within the controller to update the Jacobian Matrix from tracking data. However, for well-behaved manipulators in known environments, model-based controllers are still more accurate and reliable [98].

This chapter proposes a control framework designed to address the unique challenges of low stiffness TFA soft continuum manipulators being actuated in free space, under quasistatic deployment conditions. This is achieved through a combination of a kinematics model based on Cosserat rod theory with known external loads due to gravity, closed loop control with respect to the manipulator pose, and closed-loop control with respect to the actuators. A similar mixed feedback controller was used to enhance the control performance of multi-backbone continuum robots [102]. The use of Cosserat rod model provides a more accurate description of the kinematics when compared with simpler models such as CC-based models, though due to many simplifying assumptions used to reduce the calibration problem and increase computational speed (such as uniform precurvature, isotropic stiffness, linear elastic material, etc.), it is still not sufficiently accurate in the absence of feedback. Manipulator pose feedback is utilized to account for these modelling approximations, while actuator space feedback is used to account for nonlinearities of the actuation

system that can lead to incorrect tip wrench estimation that would produce errors in the kinematic model. This drastically improves accuracy for the case of TFA manipulators of extremely low stiffness.

4.2   Closed-loop Control in Task Space

In this section, a control scheme that can be applied to a soft manipulator actuated by a follower wrench in free space si presented. During the motion, the body of the soft manipulator is acted upon by various forces and moments, including the tip follower actuation wrench, external distributed and point loads due to gravity, and internal forces and moments within the elastic structure. The goal of the control scheme is to select and apply the tip follower wrench required to produce a static equilibrium corresponding to a desired manipulator pose. In addition to achieving a desired pose, reducing oscillations enough to smoothly transition from one desired equilibrium state to another is challenging for soft continuum robots under TFA. These oscillations result primarily from two factors: 1) unmodeled dynamic effects that result from the acceleration of the body, and 2) the sentitivity of the manipulator pose to small changes in applied follower actuation, both of which are significant for soft compliant bodies. In addition, intrinsic model error due to inaccuracies in model parameters precludes accurate open loop control, even in the case of very slow accelerations.

To address these challenges, the proposed quasi-static control scheme includes feedback from both the actuators and the tip pose. The actuator feedback is utilized to both regulate the follower load, in order to reduce any noise or overshoot in the input signal which can produce oscillations in the soft manipulator, and to compensate for nonlinearities of the actuation system that can lead to incorrect tip wrench estimation, and thereby introduce kinematic model error. Pose feedback is required to compensate for modelling uncertainties and approximations in order to achieve the desired pose. In addition, only small accelerations are commanded to the system in order to keep dynamic effects negligi-
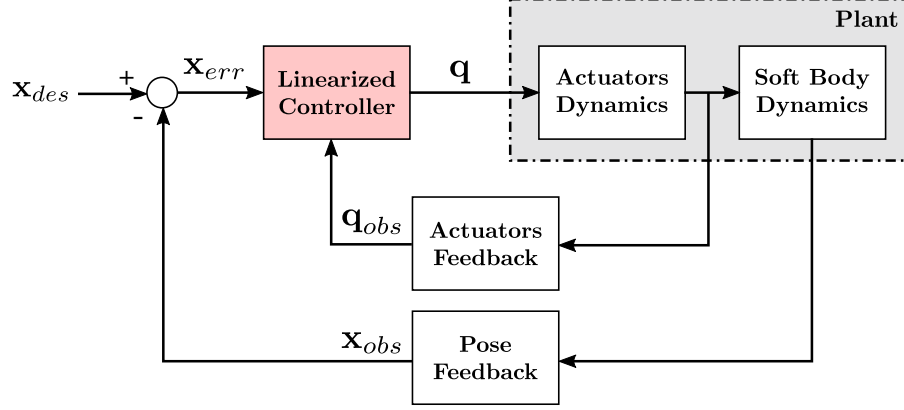
Figure 4.1: Block diagram representation of the proposed control system.

ble. All three of these features work in conjunction with one another to enable quasistatic path following.

A block diagram of the proposed control system is shown in Figure 4.1. The first feedback line senses the state of the actuator, while the second indicates the current configuration of the rod. Actuator feedback is used to estimate the current tip wrench to compute the forward kinematics model and the Jacobian matrix which maps changes in the wrench applied by the actuators to changes in the body configuration. The sensed configuration of the rod is used to calculate the error $\mathbf{x}_{err}$ between the current pose $\mathbf{x}_{obs}$ and the desired input pose $\mathbf{x}_{des}$. The pose error and actuator feedback are utilized within the linearized controller in order to solve for the desired actuator states $\mathbf{q}$.

Figure 4.2 shows the linearized controller in detail. The control signal $\mathbf{x}_{cntr}$ is obtained using a proportional-derivative feedback control scheme such as

$$\mathbf{x}_{cntr} = \mathbf{K}_p \mathbf{x}_{err} + \mathbf{K}_d \frac{d\mathbf{x}_{err}}{dt} \tag{4.1}$$

where $\mathbf{K}_p$ and $\mathbf{K}_d$ are the proportional and derivative feedback gains and $\mathbf{x}_{err}$ is the pose error defined as:

$$\mathbf{x}_{err} = \mathbf{x}_{des} - \mathbf{x}_{obs} \tag{4.2}$$
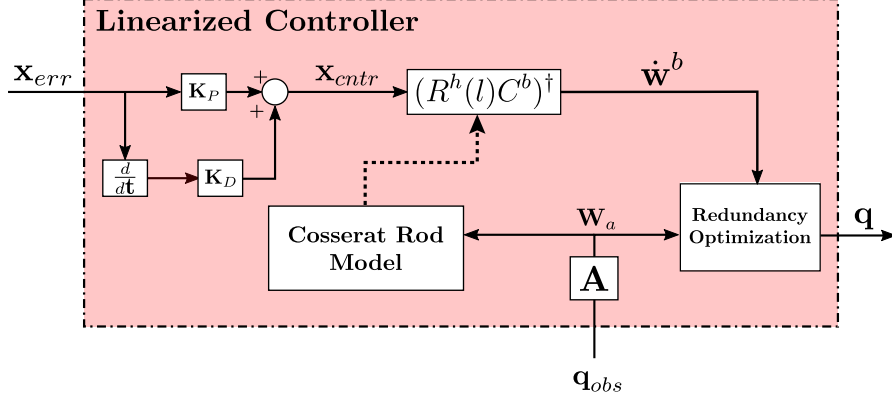
Figure 4.2: Block diagram detail of the linearized controller.

where $\mathbf{x}_{obs} = \begin{bmatrix} \mathbf{p}(l) & \theta_e & \psi_e & \gamma_e \end{bmatrix}^T$ and θ_e, ψ_e, γ_e represent the orientation of the tip with respect to the base frame. The control signal is then converted into change in tip wrench by using:

$$
\begin{aligned}
\dot{\mathbf{w}}^b &= (R^h(l)C^b)^\dagger \mathbf{x}_{cntr} \\
&= (\begin{bmatrix} R(l) & \mathbf{0}^{3\times3} \\ \mathbf{0}^{3\times3} & R(l) \end{bmatrix} C^b)^\dagger \mathbf{x}_{cntr}
\end{aligned}
\tag{4.3}
$$

where $R^h(l)C^b$ is inverted with a least-squares method such as the Moore-Penrose pseudoinverse, indicated by † ([103]), C^b is the body Jacobian matrix that maps changes in tip pose with changes in tip wrench ($C^b = \begin{bmatrix} (g^{-1}\frac{\partial g}{\partial w_1^b})^\vee & \dots & (g^{-1}\frac{\partial g}{\partial w_6^b})^\vee \end{bmatrix}$ as described in [90]), and $R^h(l)$ represents the hybrid transformation between body frame and base frame. The hybrid transformation is required exclusively for the purpose of commanding desired tip trajectories expressed with respect to the base frame. This transformation can be removed if the application requires tip frame velocities to be commanded. A resolved motion rate approach (Whitney, 1969) is then used to obtain the required wrench to be produced at the tip.

The DoF that can be controlled depend on the mapping between configuration pa-

Algorithm 1 Closed-loop Motion Control.

RobotMove[$\mathbf{x}_{des}$, $\mathbf{x}_{obs}$, $\mathbf{q}_{obs}$]

1: $\mathbf{x}_{err} \leftarrow \mathbf{x}_{des} - \mathbf{x}_{obs}$
2: **repeat**
3:     $\mathbf{w}_a \leftarrow A\mathbf{q}_{obs}$
4:     $\mathbf{x}_{cntr} \leftarrow PD(\mathbf{x}_{err})$
5:     $C^b \leftarrow$ SolveFK($\mathbf{w}_a$) {Eqs (3.17),(3.20),(3.23),(3.25).}
6:     $\dot{\mathbf{w}}^\mathbf{b} \leftarrow (R^h(l)C^b)^\dagger \mathbf{x}_{cntr}$
7:     **if** A is invertible **then**
8:       $\mathbf{q} \leftarrow A^{-1}(\mathbf{w}_a + \dot{\mathbf{w}}^\mathbf{b})$
9:       $ROBOT \leftarrow \mathbf{q}$ {Send Command}
10:    **else**
11:       $\mathbf{q} \leftarrow$ RedundancyOpt($\mathbf{w}_a, \dot{\mathbf{w}}^b$) { Eq.5.4 }
12:       $ROBOT \leftarrow \mathbf{q}$ {Send Command}
13:    **end if**
14: **until** $\mathbf{x}_{err} <=$ Threshold
15: **return** =0

---

rameters and generated wrench. In general the wrench can be expressed as a system: $\mathbf{w}_{a,des}(\mathbf{q}) = A\mathbf{q}$, where A is a matrix constituted of either linear or non-linear terms. If A is directly invertible then the configuration parameters can be found analytically by $\mathbf{q} = A^{-1}\mathbf{w}_{a,des}$. If the actuator values are redundant or the matrix is not directly invertible, quadratic programming methods can be used to find the configuration parameters that minimize the norm squared of the error between the desired follower wrench to be applied by the actuators $\mathbf{w}_{a,des}(\mathbf{q})$ and the applied follower wrench detected by the sensors $\mathbf{w}_a$, as:

$$\underset{\mathbf{q}}{\text{minimize}} \quad \left\| A\mathbf{q} - (\mathbf{w}_a + \dot{\mathbf{w}}^b) \right\|^2 + \|\mathbf{q}\|^2$$

$$\text{subject to} \quad \mathbf{q}_{min} \leq \mathbf{q} < \mathbf{q}_{max} \tag{4.4}$$

where $\mathbf{q}_{min}$ and $\mathbf{q}_{max}$ represent respectively the lower and the upper limit of the actuator value. The Levenberg - Marquardt algorithm is used to solve the minimization problem. The pseudo-code of the closed-loop motion control algorithm is shown in Algorithm 1.

4.3   Stability

As previously described, a change in the applied TFA wrench causes the manipulator to move into a new equilibrium configuration where internal body forces and moments are in balance with the applied wrench, as long as the robot remains in a stable static equilibrium. If the manipulator equilibrium configuration is close to an energy bifurcation point, small perturbations in the applied wrench can cause the manipulator to rapidly "snap" from one equilibrium configuration to another, spatially distant configuration ([10], [104]). In order to prevent the manipulator from reaching an unstable region of the workspace, the effective stiffness matrix S is analyzed, which relates to the manipulator's ability to counteract the applied follower load:

$$S = (C^b)^{\dagger} = \frac{\partial \mathbf{w}^b}{\partial \mathbf{x}}. \tag{4.5}$$

A similar technique was implemented in [105]. The eigenvalues of S can be calculated from the compliance matrix C^b using the singular value decomposition:

$$
\begin{aligned}
(C^b)^{\dagger} &= V\Sigma^{\dagger}U^T, \\
\Sigma^{\dagger} &= \mathrm{diag}(\frac{1}{\sigma_1} \cdots \frac{1}{\sigma_k}).
\end{aligned}
\tag{4.6}
$$

Here $(\sigma_1 \cdots \sigma_k)$ are the eigenvalues of the compliance matrix C^b. To prevent elastic instability, the eigenvalues of S ($\frac{1}{\sigma_1} \cdots \frac{1}{\sigma_k}$) must all remain greater than zero, indicating an elastic restoring force which acts to counteract applied loads and maintain a stable equilibrium. Greater eigenvalues correspond to configurations that are more robust to external disturbances. Thus, our stability metric is defined as:

$$\sigma_c = \min(\mathrm{diag}(\Sigma^{\dagger})) \tag{4.7}$$
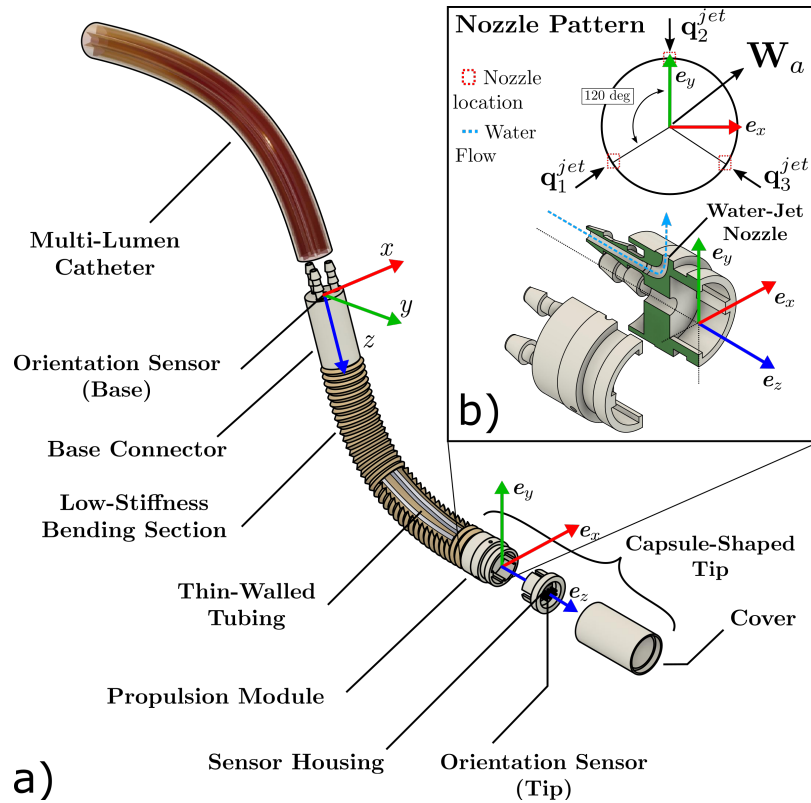
Figure 4.3: The HydroJet, is used to experimentally validate the proposed control method, showing a) Exploded view of the continuum endoscope, and b) a detailed view of the locations of the water jet nozzles with respect to the tip frame.

which must remain greater than zero during operation to avoid elastic instabilities.

4.4   Experimental Methods

The modelling and control framework described previously can be applied to any soft continuum manipulator under TFA and tip load. In order to experimentally assess the proposed approach, the proposed method is appliad to control the motion of the HydroJet device.

4.4.1   HydroJet System Testbed

The testbed was assembled as illustrated in Fig. 4.4. The capsule-shaped tip components (propulsion module, sensor housing, cover) were made from a durable plastic (Clear
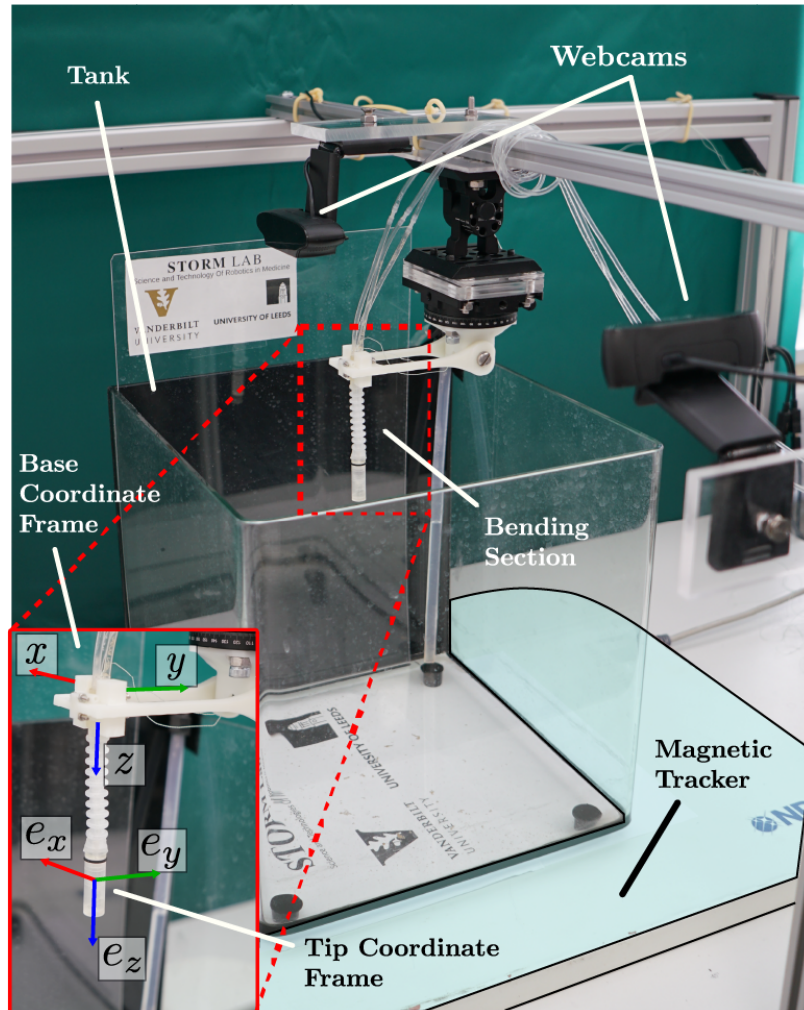
Figure 4.4: Experimental setup consisting of a magnetic tracker, two webcams and the HydroJet. At the bottom left corner, the base and tip reference frames are shown.

resin, FormLabs, Sommerville, MA, USA) through rapid prototyping. The tip outer diameter and length are 9.80 mm and 28 mm, respectively. A 6 DoF electromagnetic sensor (Northern Digital Inc., Canada) was integrated within the capsule and aligned to the capsule frame. The wire of the electromagnetic sensor runs through the soft-elastomer bellows together with the three single-lumen water lines connecting the tip to the base connector (Fig. 4.3). The base was connected to three solenoid water valves (A352273, Asco Numatics, USA) using standard hydraulic tubing (1/16"ID X 1/8"OD Tygon E-3603, Cole-Parmer, USA). The flow rate of each of the water lines was measured using independent

flow sensors (710-V00A Atrato ultrasonic flow sensor, Titan Enterprises Ltd., UK). The base connector was held in the desired orientation using a custom 3D printed holder attached to a manual rotation stage (PR01/M, Thorlabs, USA). The assembly was secured in place through attachment to an aluminum frame (Rexroth, Bosch, Germany). A second 6 DoF electromagnetic sensor (EM) was attached to the base holder to sense the orientation of this frame as well. Two webcams (C930e, Logitech, Switzerland) were placed in the positions shown in Fig. 4.4 to visually observe the motion during the various experiments from front and top view.

4.4.2   Calibration

The kinematic model was calibrated through optimizing the set of parameters listed in Table 4.1 to best fit experimental data. The boundary conditions for the HydroJet are described as follows: at $s = 0$, position is considered to be zero and the orientation is captured via the electromagnetic sensor within the base connector. At $s = l$, the three components of the internal moment must be zero and the force expressed in tip frame is defined by the flow rates of the three waterjets. Considering that the water nozzles are spaced approximately 120 degrees apart around the diameter of the capsule (Fig. 4.3), the net applied wrench in the body frame acting on the tip of the manipulator due to the water-jet forces is defined as:

$$\mathbf{w}(\mathbf{q}) = A\mathbf{q}$$

$$\begin{bmatrix} w_x \\ w_y \end{bmatrix} = A \begin{bmatrix} q_1^{jet} \\ q_2^{jet} \\ q_3^{jet} \end{bmatrix} \tag{4.8}$$

$$A = \begin{bmatrix} \sin\left(\frac{\pi}{3} - \delta\beta\right) & \sin(\delta\alpha) & -\sin\left(\frac{\pi}{3} - \delta\gamma\right) \\ \cos\left(\frac{\pi}{3} - \delta\beta\right) & -\cos(\delta\alpha) & \cos\left(\frac{\pi}{3} - \delta\gamma\right) \end{bmatrix}$$

where q_1, q_2, and q_3 are the three applied forces due to the water jets and $\delta\alpha, \delta\beta, \delta\gamma$ represent the deviation in alignment of the actual jet force with the intended direction due to manufacturing imperfections (Fig. 4.5). With the applied wrench $\mathbf{w}_a$ expressed in the tip frame, we can express the boundary conditions at $s = l$ as:

$$\mathbf{Q}_b(l) - \begin{bmatrix} w_x & w_y \end{bmatrix}^T = \mathbf{0}$$
$$\mathbf{u}(l) - \widetilde{\mathbf{u}}(l) = \mathbf{0} \tag{4.9}$$

For the purpose of modelling, the bellow and the internal water lines were considered as a single element having a cylindrical shape with inner diameter of 6 mm, outer diameter of 8 mm, and a length of 90 mm. The soft body is considered massless (i.e. $m_b = 0$) and the mass of the capsule m_t (2.58 g) is used in equation (3.24) to compute the force due to gravity in tip frame. This assumption is reasonable for this particular robot design, as the concentrated mass at the tip has a much greater influence on its motion than the smaller mass distributed along the length.

The force exerted on the capsule from the water jets was calculated using the thrust equation:

Table 4.1: Calibrated values of model parameters

Parameter	Value
$q_1^{jet}\|_{max}$	243 mN
$q_2^{jet}\|_{max}$	224 mN
$q_3^{jet}\|_{max}$	244 mN
GJ	$2.23 \cdot 10^{-4}$ N m
EI	$6.01 \cdot 10^{-4}$ N m
u_x	$0.034\ m^{-1}$
u_y	$0.88\ m^{-1}$
A_{in}	$1.13 \cdot 10^{-6}\ m^2$
A_{out}	$3.84 \cdot 10^{-7}\ m^2$
L	0.09 m
m_t	2.58 g
$\delta\alpha$	0.12 rad
$\delta\beta$	0.06 rad
$\delta\gamma$	-0.08 rad

$$\mathbf{q}^{jet} = -\dot{m}(\mathbf{v}_{in} - \mathbf{v}_{out}) \tag{4.10}$$

where $\dot{m}$ is the mass flow rate through the jet cavity, and $\mathbf{v}_{out}$ and $\mathbf{v}_{in}$ are the outlet and inlet velocity that relate to the nozzles external and internal areas through $\mathbf{v}_{in}A_{in} = \mathbf{v}_{out}A_{out}$. The EM sensor was aligned to the tip frame by placing the tip of the soft manipulator in a calibration box with a known position with respect to the global frame. This calibration allowed the alignment of the jets with respect to the EM frame. A similar calibration procedure was performed for the base orientation sensor to align its frame with respect to the base holder. The orientation of both frames with respect to the global frame is shown in Fig. 4.4.

The calibration of the soft body parameters was done experimentally by finding the parameter vector ζ_{cal}^* that minimizes the objective function representing the rotation error between the estimated and experimentally observed orientations over a set of 40 random jet force combinations around the workspace:
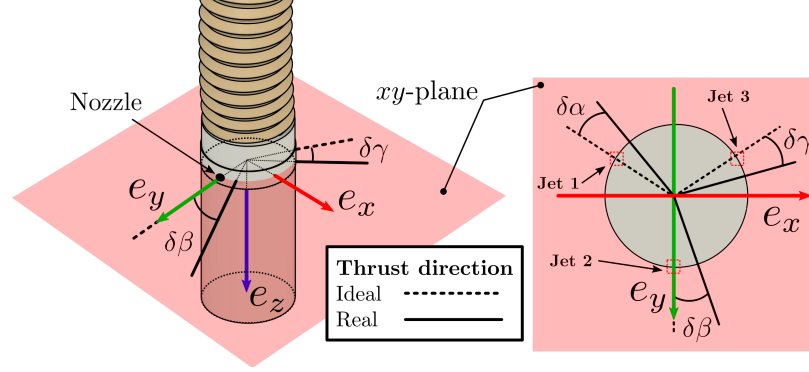
Figure 4.5: Waterjet actuation system: the force vectors generated by the jets lay on the tip xy-plane and are ideally spaced 120 degrees from each other. The parameters $\delta\alpha, \delta\beta, \delta\gamma$ describe the jets misalignment, with respect to the ideal case, due to manufacturing imperfections.

$$\zeta_{cal} = \underset{\zeta}{\arg\min}(\sum_{i=1}^{40} ||(< \mathbf{h}_m(\mathbf{q}_i, \zeta), \mathbf{h}_i >)||^2) \qquad (4.11)$$

where $\mathbf{h}_m = a + b\mathbf{i} + c\mathbf{j} + d\mathbf{k}$ represents the quaternion associated with the rotation computed by solving the forward kinematics with inputs $\mathbf{q}_i$ and parameter vector ζ, $\mathbf{h}_i$ represents the quaternion associated with the measured experimental rotation from the EM sensor, and $< \cdot >$ represents the scalar product of two vectors. The parameter vector is constituted by: $\begin{bmatrix} u_x & u_y & G & E & \delta\alpha & \delta\beta & \delta\gamma \end{bmatrix}^T$. Results of the calibration are summarized in Table 4.1.

4.5   Experimental Validation

Two sets of experiments were performed, each using both open-loop and closed-loop schemes. The first experiment consisted of controlling manipulator tip orientations along a spiral trajectory while having the z-axis of the base connector aligned with the direction of gravity, as shown in Fig. 4.7(a). In the second experiment, the base connector was rotated by 30 degrees around its local x-axis, and the same spiral trajectory was commanded to the manipulator. Due to this change in the alignment with respect to gravity, the forces and moments along the soft body under static equilibrium result in an initial shape ($\mathbf{w}_a = 0$) that bends toward the direction of gravity (Fig. 4.7(b)). Both of these base angles fall within

the expected range of deployment angles for the intended application of gastroscopy.

4.5.1 Path Generation

The spiral trajectory commanded to the robot was expressed in terms of two angles as $\mathbf{x}_{des}(t) = \begin{bmatrix} \vartheta_{des}(t) & \varphi_{des}(t) \end{bmatrix}^T$, with respect to the base frame, as shown in Fig. 4.6. The time-varying trajectory was defined according to the equation:

$$
\begin{aligned}
\vartheta_{des}(t) &= \vartheta_{start} + \varsigma t \\
\varphi_{des}(t) &= \varphi_{start} + \varepsilon t
\end{aligned}
\tag{4.12}
$$

where $\varsigma = 0.1$ [rad/sec] and $\varepsilon = 0.8$ [rad/sec]. Which results in a desired tip speed of 1.61 rad/sec. The tip speed is relatively low to limit the effects of both body dynamics and of nonlinearities of the actuation system. The trajectory was set to be completed in 600s. This relatively slow speed is chosen to be consistent with the quasistatic modeling assumption; however, it is still fast enough to perform the intended task of gastroscopy in the time frame of about 12 minutes typically required to complete the procedure ([106]).

4.5.2 Software Implementation

The control system was implemented in a custom C++ Linux program running on a 3.7 GHz Intel Core i7-8700K processor with 16 GB RAM using ROS Kinetic. The model equations ((3.17), (3.20), (3.23) and (3.25)) were numerically integrated, beginning with the tip pose and integrating backward toward the base. The state Jacobians were integrated with an eighth-order Runge-Kutta method ([107]). Altogether, the program is capable of solving the rod equations and calculating the necessary Jacobians within 10 ms. To provide values for $\mathbf{q}_{obs}$ and $\mathbf{x}_{obs}$, the flow sensors and electromagnetic sensors were sampled at 100Hz.
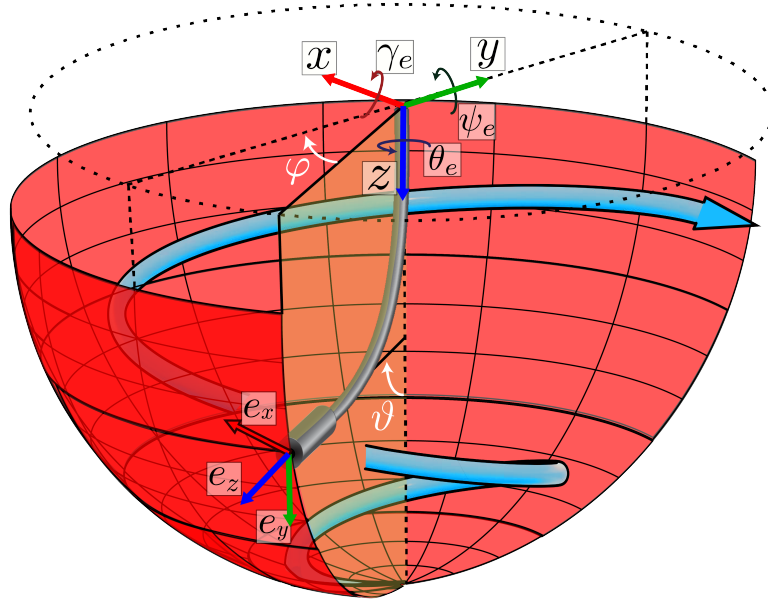
Figure 4.6: The HydroJet's workspace: the manipulator's tip can be maneuvered with two DoF by commanding ϑ and φ.

4.5.3   Open-loop Testing

The open-loop water-jet forces for a given desired orientation were computed by subsequent minimization of the tip orientation error using the Jacobian matrix, equation (4.3). In this test, the actuator feedback is utilized to compute both the estimated pose of the manipulator and the Jacobian matrix, without including any pose feedback. The desired orientation $(\vartheta_{des}, \varphi_{des})$ is converted to the equivalent representation in Euler angles (pitch and yaw) by using an axis angle transformation. The orientation error is then obtained by subtracting estimated pitch and yaw from the desired values and the water-jet forces updated accordingly. The test was considered complete if $\vartheta = 1.04$ rad and $\varphi = 14$ rad, or was aborted if the amplitude of the oscillations of the tip during the transitions between two consecutive commanded states were higher than 0.5 rad.
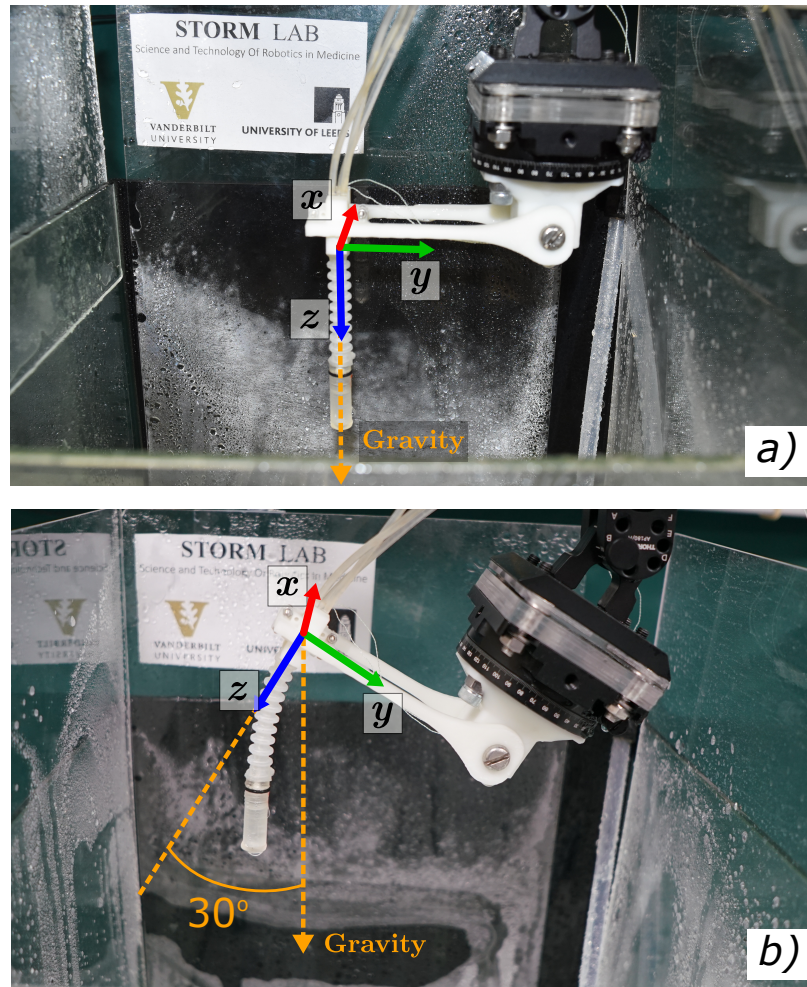
Figure 4.7: Starting configurations during the trajectory following trials: a) initially straight and b) initially bent with respect to the direction of the gravity vector.

4.5.4 Closed-loop Testing

Closed-loop testing was performed using the control scheme described in Section 4.2 utilizing both actuators and tip pose feedback. Real time computation of the water-jet forces was performed based on the orientation error between the desired values and those measured from the embedded EM sensor in the tip frame. The proportional and differential gains were manually tuned to reduce oscillations during the transition between states. Test completion criteria were the same as for the open-loop test case.
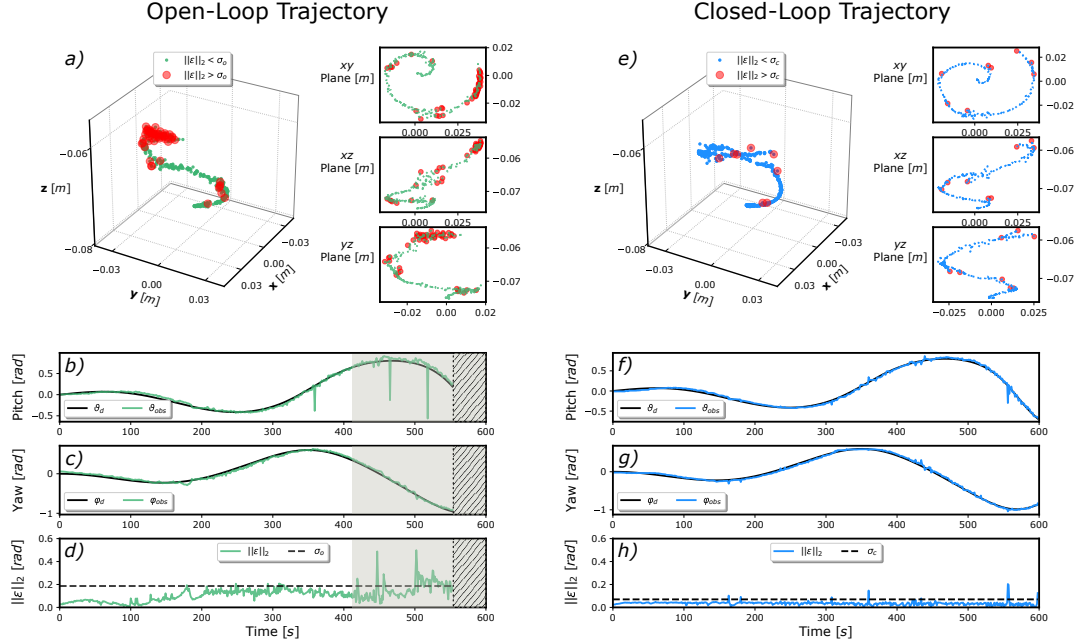
Figure 4.8: Trajectory following results for open-loop (left column) and closed-loop (right column) strategies applied to the HydroJet soft continuum manipulator under TFA with the base oriented parallel to Earth's surface, such that gravity acts along the z-axis of the robot at its base (0 degrees base angle). Graphs a) and e) show a 3D view of the measured trajectory followed by the capsule-shaped tip and its projection on xy, xz and yz planes for open-loop and closed-loop, respectively; the red dots indicate the locations of trajectory points where the norm of the error was greater than a pre-defined threshold ($\sigma = 90^{th}$-percentile). The desired (black line) and measured (colored lines) trajectories for pitch and yaw angles are shown in b) and c) for the open-loop case, and in f) and g) for the closed-loop case. Finally, the norm of the error is presented for open-loop and closed-loop trials in d) and h), respectively; the threshold (dashed line) representing the 90th-percentile, the region where where the tip oscillations become large (shaded region), and areas where the trial was aborted due to excessive oscillations ($\vartheta > 0.5$ rad (shaded region with hatch) are shown.

4.5.5 Path Following Results: Initially Straight Configuration

As mentioned previously, the first set of experiments were performed with the base aligned with gravity, i.e. with the manipulator body starting in a nearly straight configuration pointing downward (Fig. 4.7(a)). Five repeat trajectory following trials were performed for the open-loop and closed-loop control configurations. Fig. 4.8 presents the results from single trajectory tracking trials using the open-loop and closed loop control
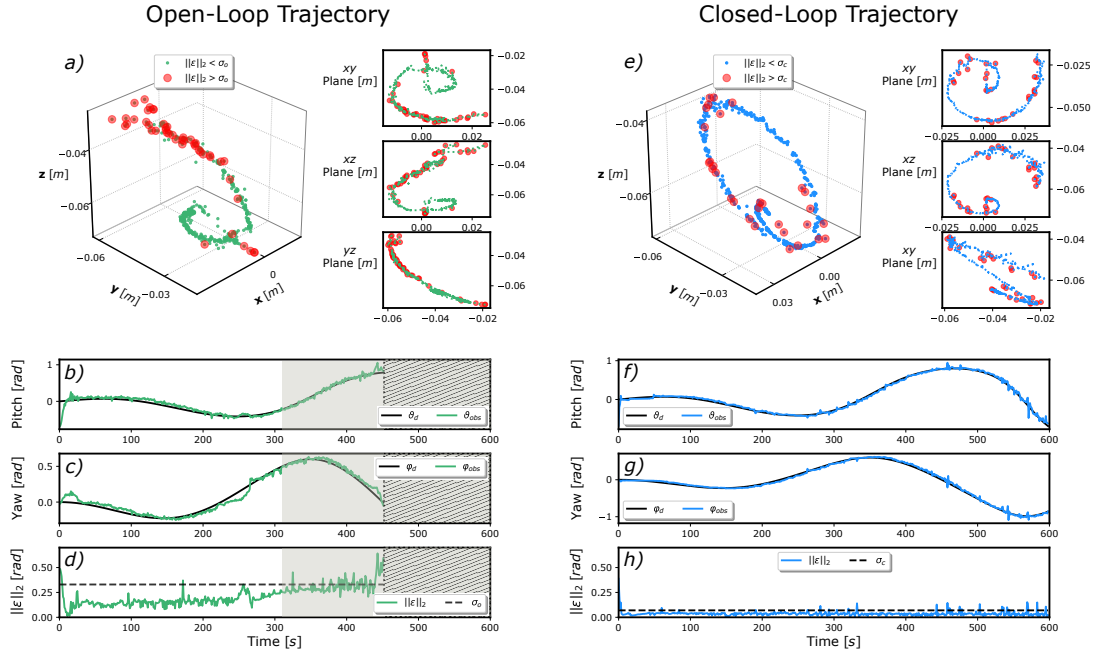
Figure 4.9: Trajectory following results for open-loop (left column) and closed-loop (right column) strategies applied to the HydroJet soft continuum manipulator under TFA with the base in a bent configuration with respect to gravity (30 degrees base angle). Graphs a) and e) show a 3D view of the measured trajectory followed by the capsule-shaped tip and its projection on *xy*, *xz* and *yz* planes for open-loop and closed-loop, respectively; the red dots indicate the locations of trajectory points where the norm of the error was greater than a pre-defined threshold ($\sigma = 90^{th}$-percentile). The desired (black line) and measured (coloured lines) trajectories for pitch and yaw angles are shown in b) and c) for the open-loop case, and in f) and g) for the closed-loop case. Finally, the norm of the error is presented for open-loop and closed-loop trials in d) and h), respectively; the threshold (dashed line) representing the 90th-percentile, the region where where the tip oscillations become large (shaded region), and areas where the trial was aborted due to excessive oscillations ($\vartheta > 0.5$ rad (shaded region with hatch) are shown.

schemes. The orientation error is defined as the Euclidean norm of the difference between desired tip orientation and measured tip orientation obtained from the EM sensor located at the tip. The points along the trajectory where the norm of the orientation error exceed the 90th-percentile of its distribution (indicated as σ in Fig. 4.8) are highlighted in red. These points represent areas of the trajectory where the system shows a slower convergence to the desired orientation with increased oscillation. The root-mean-square (RMS) open-loop and closed-loop orientation error was 0.09 rad and 0.03 rad respectively, indicating significant
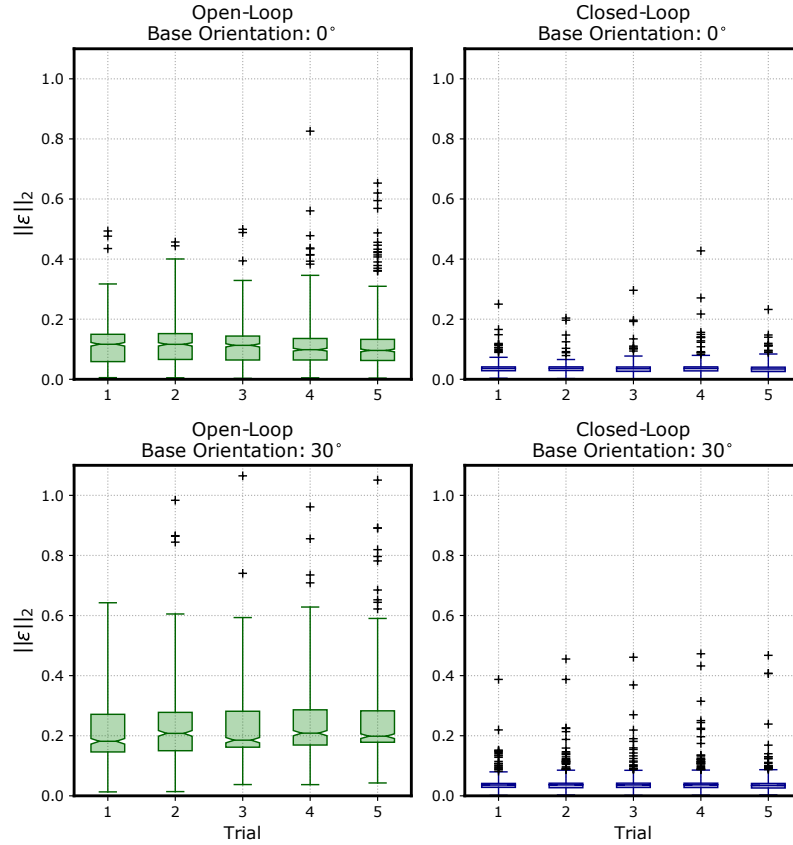
Figure 4.10: Box plot showing error distribution and variability over the 5 tests performed for each set of experiments for both closed-loop and open-loop, in the flat and pre-bent initial configuration.

improvement in tracking accuracy in the closed-loop case over the open-loop case. It is also evident from Fig. 4.8 that the closed-loop performance is consistent along the entire trajectory, while the open-loop tracking accuracy degrades and oscillations increase toward the end of the trajectory, corresponding to larger pitch angles. In addition, the desired open-loop trajectory was not completed due to excessive oscillations ($\vartheta > 0.5$ rad).

4.5.6 Path Following Results: Initially Bent Configuration

The second set of experiments demonstrate motion controllability of the soft manipulator tip along a desired trajectory starting from an initially bent manipulator configuration, induced via a 30 degree rotation of the base frame around its local x-axis (Fig. 4.7(b)),

such that it is no longer aligned with the direction of gravity. The same testing protocol described in Section 4.5.5 was implemented to again assess performance under open-loop and closed-loop control schemes. As in the previous set of experiments, five repeat trajectory following trials were performed for the open-loop and closed-loop control schemes respectively. Trajectory following results are presented in Fig. 4.9. The RMS open-loop and closed-loop orientation error was 0.18 rad and 0.035 rad respectively. The open-loop trajectory again shows a greater tracking error than the closed-loop, with accuracy and stability being largely dependent on ϑ_{des}; again, for the open-loop case, this results in an incomplete test due to excessive oscillations ($\vartheta > 0.5$ rad). In contrast, under closed-loop control, tracking accuracy is improved and the oscillation of the manipulator along the trajectory is maintained across the range of desired orientations.

4.5.7 Repeated Trials

Results indicating the median, interquartile range, maximum and minimum values for each repeat trial under the tested configuration are summarized in Fig. 4.10. To allow comparison between experimental configurations, the mean error distribution has also been presented for each control scheme and base orientation combination. For the open-loop case, large variability is evident across trial repeats, and the median error values range from 0.096 to 0.116 rad for the initially straight configuration and from 0.181 to 0.208 rad for the initially bent configuration (corresponding to $\mu \pm sd$ values of 0.115±0.072 rad and 0.228±0.106 rad respectively when averaged over all repeats). The relatively large standard deviations are in agreement with the large error distribution seen for all open-loop trials, highlighting high oscillations in the system. The influence of gravity on the soft manipulator under the initially bent configuration increases the median of the error from 0.106 to 0.197 rad when compared to the initially straight configuration; representing a increase of 85.5%.

In comparison, the closed-loop scheme generates narrow error distributions and shows
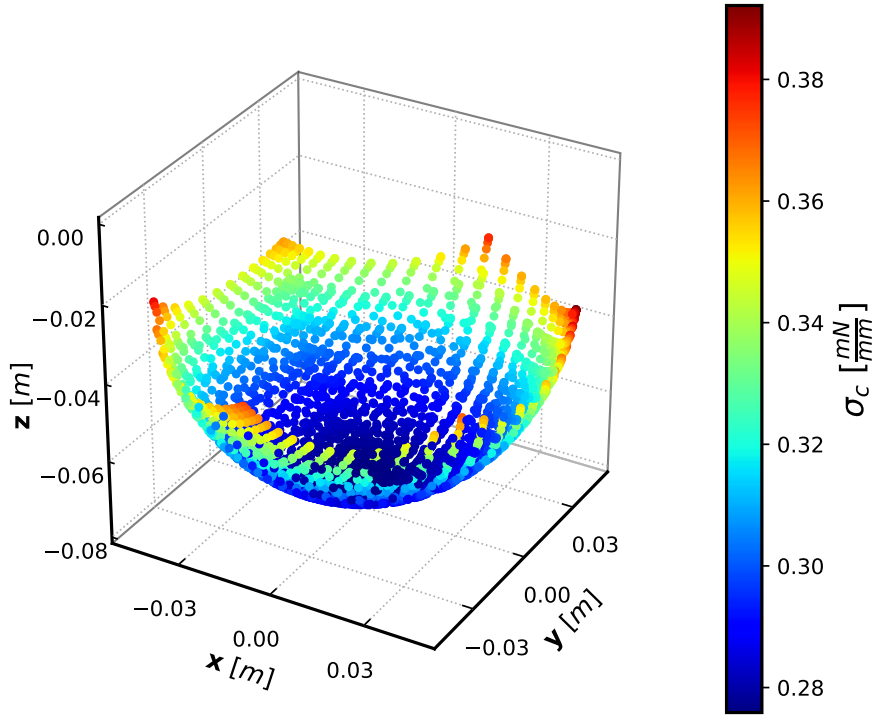
Figure 4.11: Stability test of the manipulator workspace for the initially straight case. The eigenvalues of the stiffness matrix remain positive throughout the entire actuation space.

minimum variability of the median, ranging from 0.034 to 0.037 rad for the initially straight configuration and from 0.035 to 0.037 rad for the initially bent configuration (corresponding to $\mu \pm sd$ values of 0.035±0.019 rad and 0.039±0.032 rad respectively when averaged over all repeats). The influence of gravity in the initially bent configuration increases the median error from 0.0359 to 0.0360 rad, representing an increase of 0.20%.

4.5.8 Stability Analysis

To demonstrate that both commanded paths utilized in previous experiments are within an elastically stable workspace for the manipulator, the stability measure σ_c is evaluated for the HydroJet System. The workspace is evaluated across a discretized range of jet forces spanning the achievable actuator range ($\mathbf{q} < \mathbf{q}_{max}$), resulting in an input data set of 3000 actuation combinations. For both initial robot configurations (initially straight and initially
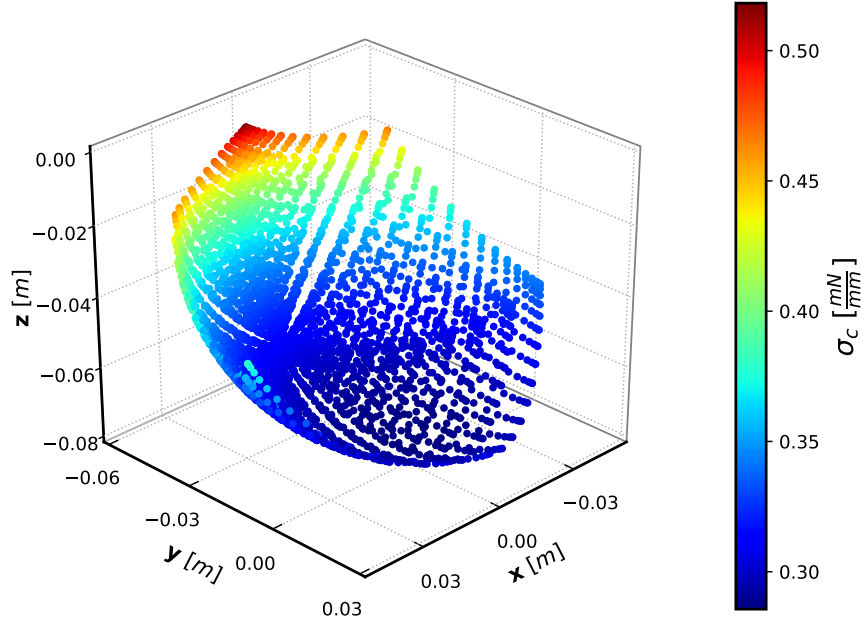
Figure 4.12: Stability test of the manipulator workspace for the initially bent case. The effective stiffness of the manipulator is not symmetric due to the rotation of the base frame. Similar to the initially straight case, the eigenvalues of the stiffness matrix remain positive throughout the entire actuation space.

bent), the stability measure is calculated by evaluating the compliance matrix at each single pose within the range of inputs. Results are shown in Figure 4.11 for the initially straight configuration and in Figure 4.12 for the initially bent configuration. In both plots, the value of the smallest eigenvalue of the S matrix remains positive throughout the entire actuation space, confirming the elastic stability of the manipulator during both previous path following tasks.

4.6   Discussion

The results suggest that the Cosserat rod equations can be successfully implemented to model and control a soft continuum manipulator under TFA in free space. The presented closed-loop scheme improves the tracking capability when compared to the open-loop test cases, as evidenced by the large reduction in orientation error when moving from the open-

loop to the closed-loop case (from 0.096 to 0.034 rad for 0 degree base angle and from 0.181 to 0.035 rad for 30 degree base angle, respectively). The open-loop oscillations are particularly prominent at larger pitch angles, demonstrating the importance of using feedback to compensate model and parameter inaccuracies intrinsic to soft manipulators under TFA. In particular, the use of a closed-loop scheme is important when considering possible clinical applications that require accurate and repeatable poses, such as camera positioning or autonomous screening. Thus, future work that focuses on adding a human in the loop through teleoperation would be interesting from both a clinical and technical standpoint.

The closed-loop scheme presented requires measurement of the tip orientation, which in the presented case was achieved using a EM sensor. The idea of using orientation feedback enables control using inexpensive feedback sensors. For example, orientations can also be tracked via lower-cost sensors, such as inertial measurement units (IMUs), embedded into the base and tip of the manipulator, without significantly reducing accuracy ([108]). This is relevant for clinical applications, where pairing cheap manufacturing of soft continuum bodies with inexpensive sensors enables the whole system to be used as a low-cost disposable medical device.

The model and control strategy can be generalized for other applications to account for, for example, a full 6 DoF wrench applied at any location along the body or a connection of multiple soft bodies with different stiffness characteristics. In addition, the Cosserat rod framework has been used in other types of continuum robots for contact detection with external bodies ([109]) and/or implementation of state constraints ([110]), suggesting these goals should also be possible for soft manipulators under TFA.

Naturally, the framework presented in this chapter has its limitations for applications that require fast transitions between equilibrium states. In that case the non-linear dynamics of the soft body may result in excessive oscillations, even under the presented closed-loop scheme, rendering the quasi-static model described in this chapter insufficient. A possible

solution was presented in [72], where a Cosserat rod based dynamic model was developed for continuum robot and might be extended for the soft manipulator case. A real-time implementation of the Cosserat rod dynamic model for the soft manipulator case would enable better control schemes, particularly in the case of fast motions of the manipulator. Another possible solution to reduce oscillations while keeping the static model is to improve the design of the hydraulic actuation system in order to obtain a more nearly linear relationship between current and flow rate. This would reduce hysteresis in the actuation system thus enable a even more precise control of the applied wrench.

4.7   Conclusions

This chapter presents a method for employing real-time control of the equilibrium configurations of soft continuum manipulators actuated via a follower wrench and experiencing external loading. The proposed method couples Cosserat rod based modelling with integrated sensing and efficient numerical determination of the Jacobian matrix at each time step to deliver a practically viable, closed-loop control system for application to soft continuum manipulators. Closed-loop performance was demonstrated on the HydroJet, and has shown to be effective in reducing orientation error and increasing system stability even under the influence of gravity. The stable closed-loop path following as demonstrated has the potential to enable semi and fully autonomous manipulation tasks in the next generation of soft continuum robots under TFA.

Chapter 5

Teleoperation and Contact Detection of Soft Continuum Manipulators Under Tip Follower

Actuation

5.1 Introduction

The previous chapters have demonstrated the ability to describe the kinematics of a soft continuum manipulator under TFA using a model based on Cosserat rod theory/PRB approximation, and to track trajectories with the device using a resolved rates approach coupled with feedback from orientation sensors. From a control strategy perspective, the purpose of this chapter is to bridge several of the gaps that remain between the prior experiments and the use of a SCM as an intuitively controlled UGI inspection device. This includes two basic components: a teleoperation scheme for translating user inputs into commanded tip trajectories, and a method for contact detection which can alert the operator when the device is no longer able to move in a certain direction due to interaction with the environment.

Teleoperation methods have been presented in literature for various continuum manipulator morphologies [111, 112, 113] and applied to endoluminal procedures [114]. Many of the presented methods rely on the resolved motion rate approach (introduced in [115]) to send commands to the manipulator's end effector. In addition to teleoperation, contact detection is a valuable addition in endoscopy, as intuitive control of the device relies on accurate computation of the manipulator's differential kinematics, and unknown external loads can introduce considerable error into this computation. Related methods for contact detection based on sensor feedback have been presented and successfully applied to other types of continuum manipulator designs, including multi-backbone robots [15, 116] and pneumatic chamber robots [117]. In this Chapter, the force deviation method presented in [116], is used to establish contact and is integrated with the closed-loop control scheme
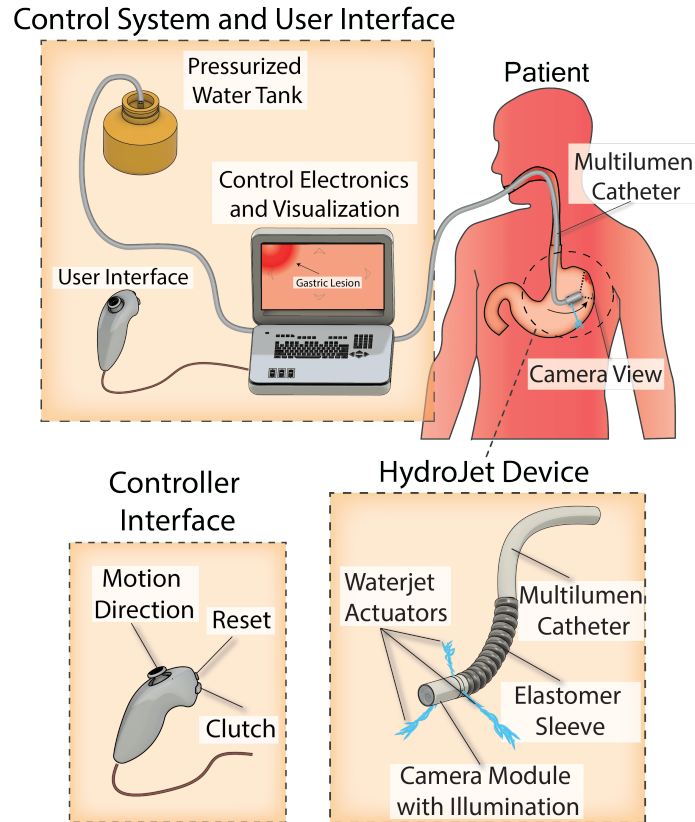
Figure 5.1: Schematic representation of UGI screening procedure using the HydroJet Endoscopic Platform. The user controls movement of the camera via the joystick coupled with manual insertion of the catheter.

based on the Cosserat framework. The integration of the contact detection within the motion controller allows less reliance on the absolute accuracy of the kinematic model and more on the ability of the differential kinematics and closed-loop controller to reduce error during free space operation. This chapter demonstrates for the first time closed-loop teleoperation of a waterjet actuated soft continuum manipulator and provides a new method that enables improved protocols to compensate for environmental interaction forces.

5.2 Telerobotic Operation and Contact Detection

The model described in Chapter 3 allows for the shape of the robot and the manipulator Jacobian to be computed for any set of actuation inputs, thereby enabling trajectory

control of the manipulator tip via a resolved rates approach. However, two key additions in the control method are required in order to enable low-cost stomach inspection with the HydroJet device. First, an intuitive method for telerobotic operation using a simple input device is required. This is important both for limiting the cost of the overall system and enabling users to operate it without the highly specialized skill set required to perform EGD with current flexible endoscopes. Second, a method for coping with environmental interactions is extremely useful for maintaining intuitive control of the device. The soft, flexible nature of the device greatly mitigates the risk of accidental injury to the anatomy; however, unmodeled external forces can have a significant impact on the accuracy of the model and Jacobian computation. Thus, unknowingly interacting the with the environment can make the device more difficult for the user to control. To combat this, a contact detection algorithm is presented, which can indicate to the user the presence and direction of contact with the environment, enabling them to either move away from the contact before the model error becomes too significant, or to turn the jets off altogether and return the device to a neutral, unpowered position.

5.2.1   Teleoperation Scheme

As stated in Chapter 2, the HydroJet can achieve motions in 2-DOF via the water jet actuators located at its tip. During stomach inspection, a third DOF of motion is available to the operator via the manual translation of the multilumen catheter within the esophagus. To provide the user with intuitive control of the two robotic degrees of freedom, we use a thumb-controlled joystick interface, as shown in Fig. 5.2. Deflection of the joystick in 2-DOF space provides desired directions of motion with respect to the camera frame whenever the user depresses a trigger-style "clutch" button on the controller. A second trigger-style button can be used to turn the water jets on and off, enabling the user to "reset" the device to its unpowered position.

The teleoperation scheme is presented in Fig. 5.3. The desired twist in the tip frame
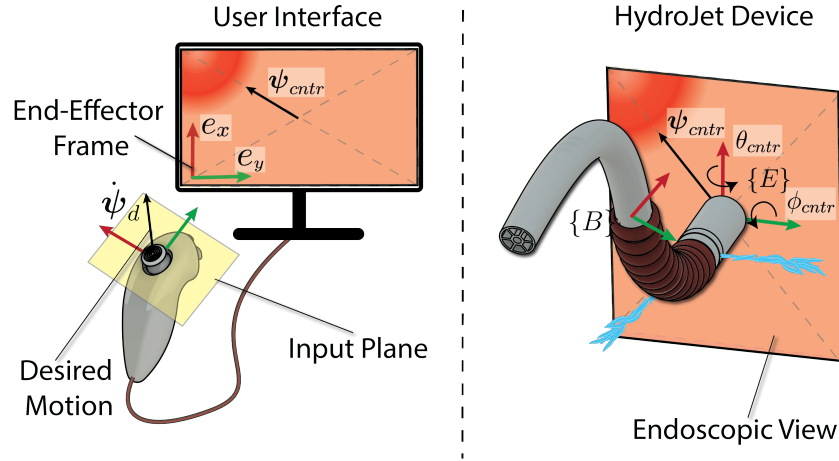
Figure 5.2: The rotation of the tip frame is commanded by summing the desired tip velocity sent through the joystick and the orientation error.

consists of velocities in the roll and pitch angle of the camera frame: $\dot{\psi}_d = \begin{bmatrix} \dot{\theta}_d & \dot{\phi}_d \end{bmatrix}^T$. The control signal ψ_{cntr} is obtained by summing the desired tip velocity to a proportional-derivative feedback term:

$$\psi_{cntr} = \dot{\psi} + \mathbf{K}_p \psi_e + \mathbf{K}_d \frac{d\psi_e}{dt} \tag{5.1}$$

where $\mathbf{K}_p$ and $\mathbf{K}_d$ are the proportional and derivative feedback gains and ψ_e is the pose error defined as:

$$\psi_e = \psi_d - \psi_{obs}. \tag{5.2}$$

The vector ψ_{obs} is the observed orientation of the tip frame with respect to the base frame and ψ_d is computed by integrating the desired tip velocity over $\dot{\psi}_d$ over time. The control signal is then converted into change in tip wrench by using:

$$\dot{\mathbf{w}}_b = \left(\mathbf{C}^T \left(\mathbf{C}_b \mathbf{C}_b^T - \mu \mathbf{I} \right)^{-1} \right) \psi_{cntr} \tag{5.3}$$

where the body Jacobian matrix $\mathbf{C}_b$ is inverted with least-squares method such as the
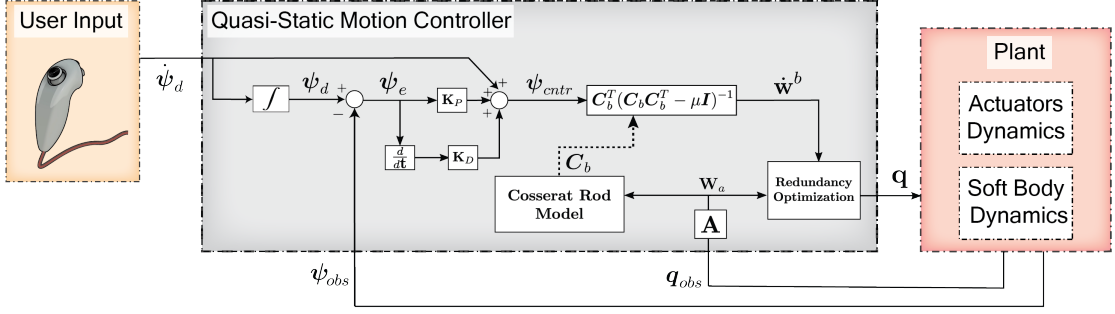
Figure 5.3: Block diagram detail of the proposed teleoperation scheme.

Moore-Penrose pseudoinverse [118], μ is a damping factor and $\mathbf{I}$ is the identity matrix. Quadratic programming is used to find the configuration parameters that minimize the norm squared of the error between the desired follower wrench to be applied by the actuators $\mathbf{w}_{a,des}(\mathbf{q})$ and the applied follower wrench detected by the sensors $\mathbf{w}_a$:

$$
\begin{aligned}
\underset{\mathbf{q}}{\text{minimize}} \quad & \left\| A\mathbf{q} - (\mathbf{w}_a + \dot{\mathbf{w}}^b) \right\|^2 + \|\mathbf{q}\|^2 \\
\text{subject to} \quad & \mathbf{q}_{min} \leq \mathbf{q} < \mathbf{q}_{max}
\end{aligned}
\tag{5.4}
$$

Here, $\mathbf{q}_{min}$ and $\mathbf{q}_{max}$ represent respectively the lower and the upper limit of the actuator value.

5.2.2 Contact Detection

The contact detection algorithm enables the system to detect when the tip comes into contact with its environment based on commanded tip forces and orientation feedback provided by the two IMUs. It is intended to work in combination with the telerobotic scheme presented in Section 5.2.A. At each time step of the teleoperation loop, the inputs to the contact detection algorithm are the commanded angular velocity vector $\dot{\psi}_d$, the kinematic error ψ_e and the Jacobian matrix $\mathbf{C}_b$. The algorithm can be thought of as a state machine which moves between three different states: (1) no contact, (2) possible contact, and (3)

confirmed contact. The pseudocode for the algorithm is presented in Algorithm 2.

The algorithm is assumed to start from a contact-free state when the user enables the jets to begin teleoperation. As the device is driven by the user, the system remains in a contact-free state as long as the kinematic error remains below a pre-selected threshold. Possible contact is triggered any time that

$$\|\boldsymbol{\psi_e}\| - \zeta_\psi > 0 \tag{5.5}$$

where $\|\boldsymbol{\psi}_e\|$ is the norm of the kinematic error vector, and ζ_ψ is the threshold value on kinematic error.

During possible contact, the PD controller will continue to act to close the error in commanded pose by incrementing/decrementing the applied wrench. If the error falls back below the threshold (consistent with transient unmodeled effects), the system returns to the contact-free state; otherwise, if the actuation wrench continues to change in a certain direction without reducing the error in that direction to below the error threshold, this confirms contact detection in that direction. This condition is tested by monitoring the difference between the current commanded wrench, $\mathbf{w}^b$, and the commanded wrench at the onset of possible contact, $\mathbf{w}_c$. To facilitate determination of the direction of contact, the x- and y-components of this difference are computed separately. The conditions for contact in the x and y directions can then be written as:

$$\begin{aligned} \left\| \mathbf{w}^b|_x - \mathbf{w}_c|_x \right\| &> \zeta_\sigma \\ \left\| \mathbf{w}^b|_y - \mathbf{w}_c|_y \right\| &> \zeta_\sigma \end{aligned} \tag{5.6}$$

where the two equations describe contact conditions along the x-axis and y-axis, respectively, an ζ_σ is another pre-selected threshold on the change in commanded wrench during possible contact. The direction of contact on either axis (i.e. if contact is occuring on the positive side of the axis or the negative) can then be deduced according to the desired direction of motion $\boldsymbol{\psi}_{cntr}$.

Algorithm 2 Contact Detection.

ContactDetection$[\dot{\psi}_d, \psi_e, \mathbf{C}_b]$

1: $\psi_{cntrl} \leftarrow \dot{\psi}_d + \mathbf{K}_p \psi_e + \mathbf{K}_d \dot{\psi}_e$
2: $\mathbf{w}^b \leftarrow \overline{\mathbf{w}}_b$
3: **repeat**
4:     $\mathbf{w}^b \leftarrow \mathbf{w}^b + \mathbf{C}_b^{\dagger} \psi_{cntr}$
5:     **if** $\|\psi_e\| > \zeta_\psi$ **then**
6:        Possible Contact $\leftarrow true$
7:        $\mathbf{w}_c = \mathbf{w}^b$
8:     **else**
9:        Possible Contact $\leftarrow false$
10:    **end if**
11:    **if** Possible Contact $== true$ **then**
12:      **if** $\left\| \mathbf{w}^b|_x - \mathbf{w}_c|_x \right\| > \zeta_\sigma$ **then**
13:         **if** $\psi_{cntrl}|_x > 0$ **then**
14:           Contact Triggered X+ $\leftarrow true$
15:         **else**
16:           Contact Triggered X- $\leftarrow true$
17:         **end if**
18:      **end if**
19:      **if** $\left\| \mathbf{w}^b|_y - \mathbf{w}_c|_y \right\| > \zeta_\sigma$ **then**
20:         **if** $\psi_{cntrl}|_y > 0$ **then**
21:           Contact Triggered Y+ $\leftarrow true$
22:         **else**
23:           Contact Triggered Y- $\leftarrow true$
24:         **end if**
25:      **end if**
26:    **end if**
27: **until** Reset $== true$
28: **return** $=0$

5.3   Experimental Validation

To validate our proposed teleoperation scheme for EGD, we first experimentally assessed the effectiveness of our contact detection method, then performed several simulated stomach inspection trials. All experiments were performed in water to increase the damping during motion.

5.3.1   HydroJet System TestBed

The overall device consists of four main parts: the distal tip, the soft sleeve, the base connector and the multilumen catheter (Fig. 5.4.(a)). With the exception of the catheter and sleeve, all parts are manufactured using photosensitive resin (Clear resin, FormLabs, Sommerville, MA, USA) through SLA rapid prototyping. The distal tip contains a camera (AD- 3915, Aidevision, China) with illumination and an inertial measurement unit (IMU) (BNO055, Bosch Sensortech, USA). It has a cylindrical shape, with a diameter of 11.7 mm and length of 28 mm. A soft elastomer sleeve (Ecoflex 00-30, Smooth-On, USA) connects the distal end of the multilumen catheter to the tip, and encases three flexible tubes which carry pressurized water from the multilumen catheter to the jets. This structure is designed to be significantly softer and more flexible than the multilumen catheter. As a result, the forces generated by the actuators produce bending almost entirely within the soft sleeve portion of the device rather than in the multilumen catheter, enabling high bending angles within a relatively small workspace.

The base connector serves as an interface between the multilumen catheter, which is connected directly to three solenoid valves, and to the individual tubes within the bending section. It also contains a second inertial sensor, which provides a reference frame in which to describe the bending of the tip and aids in kinematic modeling by providing knowledge of the direction of external constant forces acting on the device (i.e.gravity, buoyant forces, etc.).
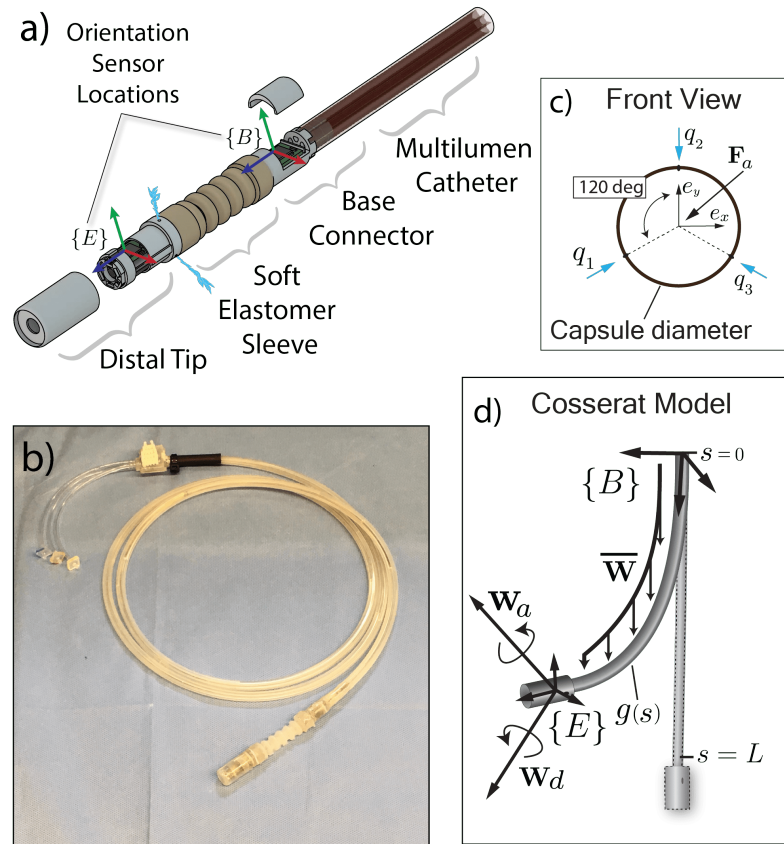
Figure 5.4: a) Exploded view diagram of the Hydrojet device. b) Photo of the prototype used in experiments. c) Head-on view diagram of the capsule tip, showing the direction of the jet locations and coordinate frame definition.d) Kinematic variable definitions used for the Cosserat rod model.

With each jet's actuation force controlled individually, the net force acting on the robot's tip produces bending of the soft sleeve, resulting in two degrees of freedom of motion. The net applied wrench in the body frame acting on the tip of the manipulator due to the water jet forces is:

$$\mathbf{F_a}|_{xy} = A \begin{bmatrix} q_1 \\ q_2 \\ q_3 \end{bmatrix} \tag{5.7}$$

$$A = \begin{bmatrix} \sin\left(\frac{\pi}{3}\right) & 0 & -\sin\left(\frac{\pi}{3}\right) \\ \cos\left(\frac{\pi}{3}\right) & -1 & \cos\left(\frac{\pi}{3}\right) \end{bmatrix}$$

where q_1, q_2, and q_3 are the three applied forces due to the water jets and $\mathbf{F}_a|_{xy}$ represents the *x* and *y* components of the tip force in tip frame, as defined in Fig. 5.4.(c). *A* represents a geometric mapping according to the locations of the jets. Since the three actuators are all coplanar with the tip of the endoscope, the *z* component of the force is zero.

5.3.2 Contact Detection Algorithm Validation

The first set of experiments was designed to investigate the performance of the contact detection algorithm in the idealized case in which the base does not move during teleoperation, to facilitate repeated testing under consistent conditions. Using the testbed shown in Fig. 5.5, the base of the HydroJet was clamped to a rigid, fixed frame, with the device pointing downward in an initially straight configuration. A glass container was placed around the robot, creating an obstacle in every direction for the HydroJet to contact with. The tip of the device was commanded in four different directions with respect to the camera frame (+X, -X, +Y, -Y) by deflecting the joystick left, right, up and down. The glass container was approached five times from each of the four directions. The time of contact according to visual inspection was recorded, along with the times at which the algorithm identified as possible contact and confirmed contact. Results for one example trial in each direction are shown in Fig. 5.7, illustrating the algorithm's ability to identify possible contact conditions based on a threshold on rotational error (first row on Fig.5.7), and to confirm contact based
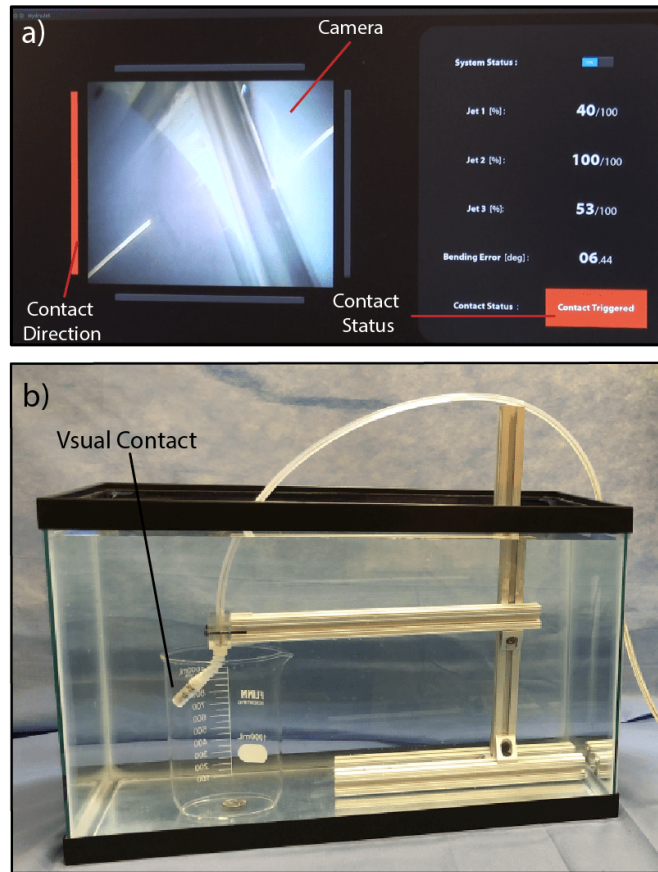
Figure 5.5: a) User interface communicating left side contact detection via the red bar on the left side of the screen and the red "Contact Triggered" status. b) Experimental setup for the repeated contact detection trials, including the contact which generated the messages on the GUI in (a).

on subsequent change in actuation force (second row of Fig.5.7). The direction of contact can be inferred from the desired direction of motion after contact was detected (third row of Fig.5.7). In all 20 experiments, contact and direction of contact were successfully detected by the proposed algorithm. On average, visual contact was achieved 6.34 seconds before contact was confirmed by the algorithm; however, this time depends on the selected force threshold which can be tuned to achieve more or less sensitive behavior of the algorithm. We next tested the contact detection algorithm with the constraint on the base frame removed, and the tether held by the operator as shown in Fig.e 5.6.(a) , more closely simulating the conditions of teleoperation during EGD. The results of one example contact
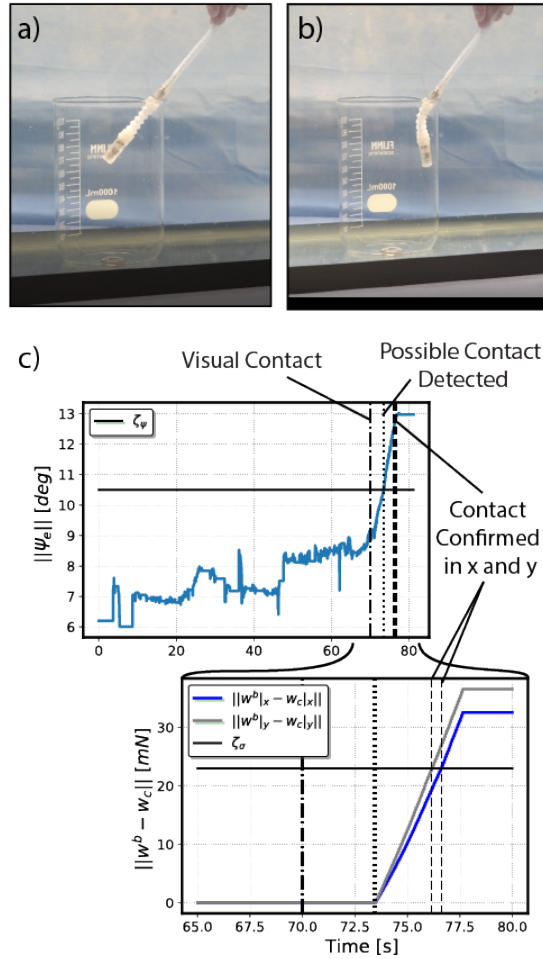
Figure 5.6: a) Starting configuration with user holding the HydroJet. b) Configuration after visual contact is triggered. c) Experimental plots showing the norm of the orientation error and the difference between the current commanded wrench and the commanded wrench at the onset of possible contact.

detection are shown in Fig. 5.6.(b). As seen in Fig. 5.6.(c) visual contact was detected 6.2 sec before the contact was triggered.

5.3.3 Stomach Inspection

To assess the ability for an operator to use the HydroJet to complete EGD, we performed a simulated stomach inspection in a phantom model. The clinical standard for a successful completion of an EGD is the visualization of six key landmarks (gastro-esophageal junction
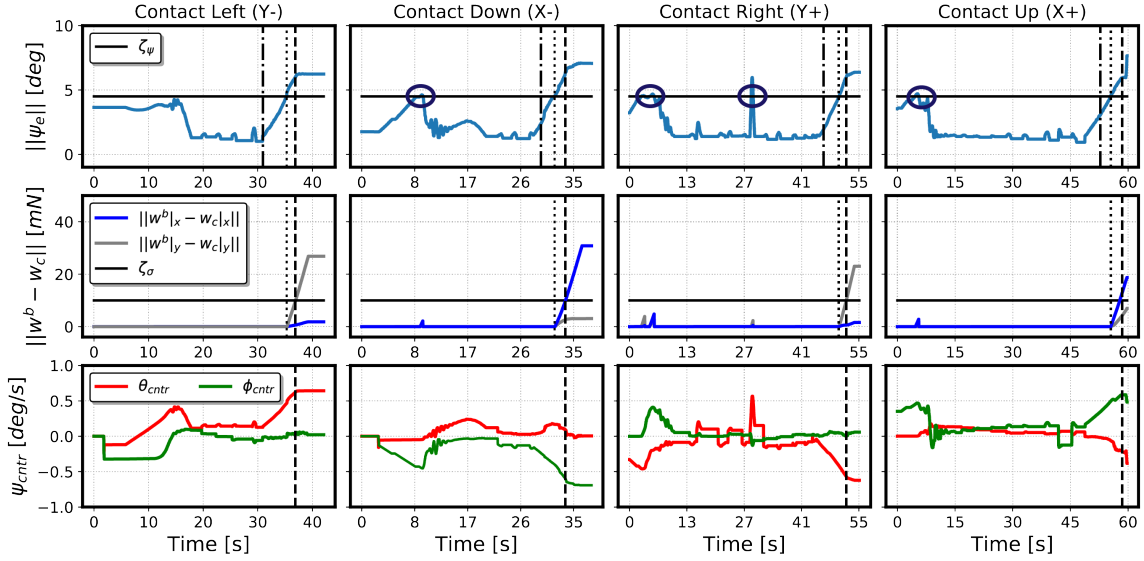
Figure 5.7: Results of contact detection trials in four directions (left, down, right, up) with respect to the camera frame. The first row shows the kinematic error measurement over time, with the horizontal line representing the threshold for possible contact. The vertical lines represent the time of visual contact, possible contact detected, and contact confirmed by the algorithm (in order from left to right). Circled locations on these plots correspond to times when transient error resulted in the algorithm identifying possible contact temporarily. The second row shows the change in force after the detection of possible contact. In each case, this measure increases in the direction of contact without bringing the error back below the possible contact threshold. The third row shows the commanded motions, which determine the direction of contact along each axis.

(GEJ)/cardia, antrum greater and lesser curvature (AGC and ALC), body greater and lesser curvature (BGC and BLC), and fundus). The experimental setup is presented in Fig. 5.8. An UGI tract phantom, consisting of an esophagus and an anatomically realistic stomach with internal capacity of 1.5 L was pressure molded using transparent plastic sheets. Six different colored pieces of tape were placed at the key landmark positions in the stomach by an experienced gastroenterologist. A novice user was asked to manually insert the device into the esophagus, then use the joystick interface to perform an inspection. The phantom model was hidden to the user, such that the only visual feedback was from the HydroJet's camera view. All six landmarks were successfully inspected during the procedure, as shown in Fig. 5.9, with an overall procedure time of 3 minutes and 5 seconds. Contact with the stomach walls was detected four times in total; three of those four times, the user opted to
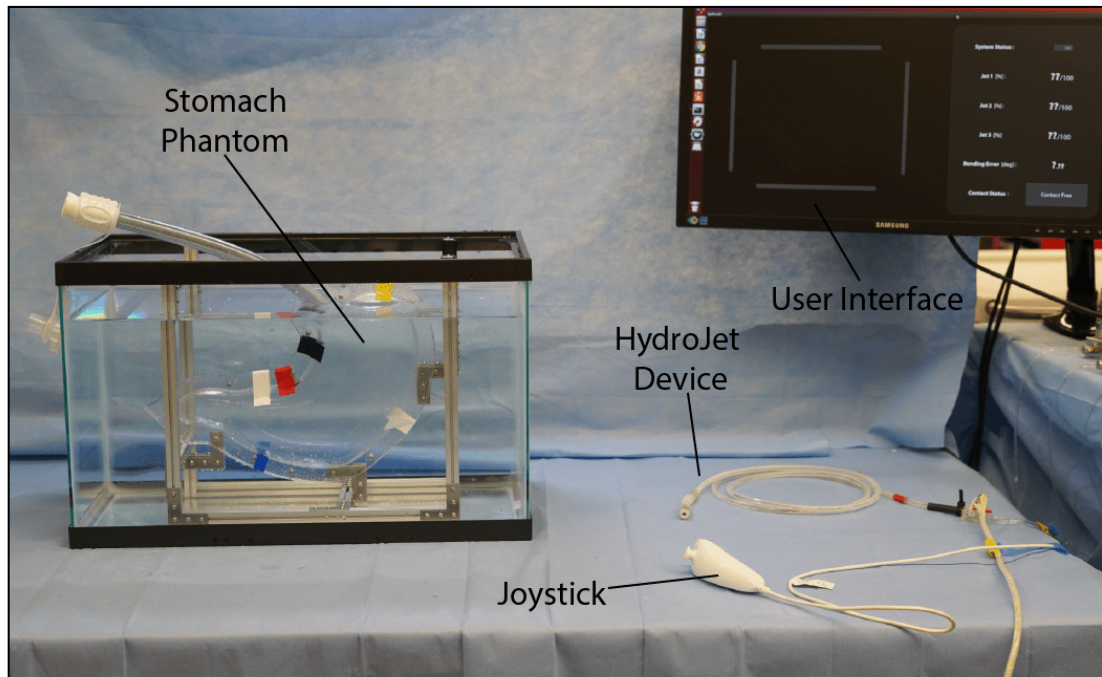
Figure 5.8: Teleoperation setup.

turn off the jets and reset the device to its unpowered position.

5.3.4 Repeated Trials

To further explore the efficacy of the HydroJet System, a total of 30 trials (15 using the HydroJet System and 15 using a conventional endoscope as a benchmark device) were performed in the phantom model. One expert gastroenterologist (having performed >3,000 lifetime EGDs) and two non-expert users with minimal or no previous experience with FEs were asked to perform visualization of the six key landmarks using either the HydroJet or a conventional FE (Karl Storz-Tuttlingen, Germany). In all experiments, direct view of the phantom was blocked and the users were asked to rely only on camera feedback to complete the inspection. Each user performed the trial 5 times with each device, and for each trial, the time required to visualize all the landmarks and thus complete the procedure was recorded. The time required for each user group to complete the inspection with each device (including mean, standard deviation (STD), first quartile (Q1) and third quartile
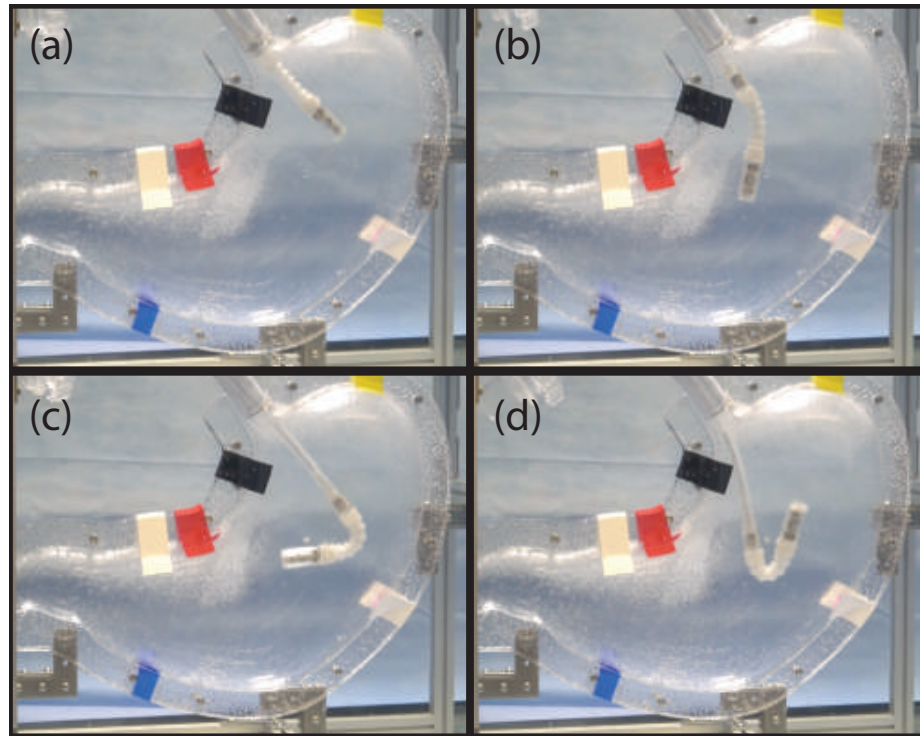
Figure 5.9: Endoscope configurations when visualizing various markers representing important GI landmarks.

(Q3)) are shown in Table 5.1.

The expert user took less time to complete landmark visualization with the conventional endoscope compared to the HydroJet (mean 1 minute and 5 seconds vs. 2 minutes and 32 seconds, respectively). With novice users, the HydroJet took on average comperable time to the flexible endoscope to complete a procedure. With the expert user, the difference between the HydroJet and flexible endoscope was larger due to the users prior expertise in using traditional endoscopes.

5.4   Discussion

The work in this chapter represents several key steps toward clinical use for the HydroJet system. The presented contact detection algorithm addresses one of the major challenges of eye-in-hand teleoperation in a system like this, enabling the user to cope with external loading in an informed way and maintain intuitive control of the device. One of

Table 5.1: Repeated trials results

User Group	Inspection Time	Device	
		HydroJet	Conventional Scope
Expert	Mean [*min* : *sec*]	2:32	1:05
	STD [*min* : *sec*]	1:05	0:43
	Q1 [*min* : *sec*]	1:14	0:40
	Q3 [*min* : *sec*]	2:48	1:11
Novice	Mean [*min* : *sec*]	3:30	3:21
	STD [*min* : *sec*]	1:34	1:60
	Q1 [*min* : *sec*]	2:27	2:10
	Q3 [*min* : *sec*]	4:02	4:30

the remaining challenges associated with this approach, however, is a protocol for selecting the appropriate thresholds on orientation error and change in force to trigger possible and confirmed contact, respectively. In this work, thresholds were heuristically selected which were suitable for the HJ prototype and the rigid environment it interacted with in these experiments. In future work, it would be valuable to implement an automated method for tuning these thresholds in the same way that the kinematic parameters for the device are tuned automatically. A method for continuously adjusting these thresholds based on the speed and pose of the device could even further improve the performance of the contact detection algorithm.

In addition to developing a contact detection algorithm, this chapter has demonstrated for the first time the integration of a human operator into the control loop for a waterjet-actuated soft continuum robot. The intuitive and inexpensive user interface enabled even novice users to complete full gastric cancer screenings in a clinically reasonable amount of time as shown by the experiments in the phantom model. While these experiments

provide a highly promising first investigation of the HydroJet's capabilities as a telerobotic upper GI inspection device, more studies are needed to further explore its capabilities and limitations. In the future, trials with larger groups of participants from a broader variety of training backgrounds will serve to expand these results beyond proof of concept. In addition, future studies in phantom models whose mechanical properties better simulate those of real tissue will also be valuable, as well as eventual studies in animal models.

While these experiments showed that complete inspections performed with the Hydro-Jet tend to take a somewhat greater amount of time than those performed with a conventional endoscope, this increase in time is negligible in comparison with the amount of time a patient spends in a clinic or hospital for pre- and post-procedure care. A typical diagnostic EGD procedure takes just 4-12 minutes, while the total time the patient spends with the medical staff is 60-120 minutes when sedation, recovery and discharge are included [56]. More importantly, the reduced cost of the HydroJet device stands to make gastric cancer screenings available to patients with little or no access to gastroscopies performed with conventional endoscopes. In addition, the disposable HydroJet represents a potential solution to the problem of inter-patient cross-contamination in settings where FEs are available but access to proper sterlization facilities are limited [37].

5.5   Conclusion

This chapter details a new method for performing UGI inspection with a soft, waterjet-actuated robotic device called the HydroJet. This low-cost, intuitive, and intrinsically safe device is designed specifically to meet a major need for increased gastric cancer screening in low- and middle-income countries. We integrate an inexpensive and intuitive user interface that enables the operator to easily control the camera to perform the inspection. To maintain intuitive control even as the device interacts with the surrounding anatomy, we developed a new contact detection algorithm, which is particularly well-suited to the extremely flexible HydroJet device. Experimental validation of the overall system in phantom

models demonstrates that even a novice user can perform a complete gastric cancer screening with our device in a clinically reasonable amount of time, and for a small fraction of the cost of a conventional gastroscopy. While further studies are needed, these results are highly promising for the HydroJet's potential as a first line of screening against one of the deadliest cancers worldwide.

Chapter 6

WAterjet Necrosecomy Device (WAND): A Soft Continuum Device for Waterjet
Fragmentation of Pancreatic Necrosis

6.1 Introduction

Acute pancreatitis is the third most common gastrointestinal diagnosis, resulting in approximately 275,000 hospital admissions and more than 2.5 $ billion in health care costs annually [119]. While the majority of cases of acute interstitial pancreatitis consist of a self-limited illness with full clinical resolution, cases of severe pancreatitis with local complications including pancreatic or peripancreatic necrosis can be associated with significant morbidity and mortality. Over a period of days to weeks following onset of necrotizing pancreatitis, areas of necrosis may evolve to form mature collections of walled off necrosis (WON) requiring intervention/drainage. Indications for drainage of WON include the presence of infected necrosis, intolerance of oral intake due to extrinsic gastroduodenal compression, obstructive jaundice due to extrinsic bile duct compression, and pain.

Current practice guidelines suggest that endoscopic intervention be preferred over surgical intervention as a first-line approach when drainage of WON is indicated [120]. The initial step in endoscopic drainage consists of endoscopic ultrasound (EUS)-guided transgastric or transduodenal access to the collection, followed by placement of a transmural stent (with or without prior dilation) to create a fistula tract and allows drainage of WON contents into the gastrointestinal lumen. While a percentage of patients with predominantly liquefied WON may achieve complete resolution with this drainage intervention alone, the majority of patients with WON containing solid debris typically require further intervention [121].

Options for further intervention include chemical or mechanical debridement [122]. Chemical debridement using hydrogen peroxide has been described, although published

reports consist largely of uncontrolled series of carefully selected patients and the potential for serious adverse events has not been fully elucidated [123]. Alternatively, mechanical debridement/necrosectomy may be facilitated by transmural retroperitoneal endoscopy via the previously created fistula tract. Once under direct visualization, instruments may be passed through the working channel of the endoscope to attempt fragmentation of solid necrotic debris. Current options for this technique consist of off-label use of endoscopic accessories including polypectomy snares, retrieval nets, forceps, and biliary stone extraction baskets. Potential adverse events of this technique include bleeding due to mechanical trauma inflicted on major vascular strictures such as the splenic artery.

A major limitation of these techniques is the inability to achieve sufficient fragmentation of solid necrotic debris. Development of innovative technologies dedicated for necrosectomy use, capable of fragmenting necrotic debris while sparing viable tissue, has been identified as a critical need in the endoscopic management of WON [120].

The use of a highly focused water beam for necrotic tissue dissection may present an alternative solution in the endoscopic management of WON. The use of waterjets in medicine has been explored in the literature [124]. In the medical field this technology has been applied in: thrombectomy, arthroscopic backbone operations, plastic surgery for removal of tattoos or liposuction, and surgical ophthalmology. Papachristou and Barters [125] were the first to describe the use of a highly focused saline beam in medicine and found that liver resection using a saline mixture results in less blood loss during the surgery. In addition, as the cutting of organs is typically caused by the particle density of the beam, it can be used as an alternative for applications such as orthopedics where unwanted structural changes of the material (bone) can occur due to heat. A microwave waterjet scalpel can be used used for minimally invasive removal or resection of localized tumors. The cutting is controlled by modifying the water beam intensity and focus depending on the type of tissue (nerve tissue, ligaments, blood vessels, etc.). [126].

To specifically address symptomatic WON, this chapter details the design of a WAter-

jet Necrostomy Device (WAND). The mechanism of tissue fragmentation offered by the WAND consists of a highly focused waterjet delivered through a 2 mm steerable catheter. This allows the device to pass through the working channel of a standard diagnostic flexible scope. The device offers adjustable levels of water beam intensity controlled through a foot pedal as well as 180 degree of articulation independent of the endoscope tip. This articulation consists of a one degree of freedom push-pull mechanism operated by rotating a nob located on the device handle. Initial phase testing demonstrated successful WAND fragmentation of gelatin in varying degrees of stiffness, as a surrogate for necrotic debris. Second phase benchtop testing demonstrated successful WAND fragmentation of freshly harvested human pancreatic necrosis.

6.2   Device Design and Fabrication

The system is presented in Fig. 6.1. The WAND is composed of three functional parts: the user handle, the three lumen catheter extrusion and the articulating tip. The articulating tip contains a waterjet nozzle whose bending is controlled by two hyperelastic nitinol wires running through the multilumen catheter through the PTFE Catheter. The nozzle and the catheter are connected by a single tri-lumen flexible tube, used to separate the two nitinol wires that facilitate tip articulation, which allows high bending angles within a relatively small workspace. Miniature pressure fittings create the hydraulic connection between the central lumen of the catheter and the flexible tube. A support sleeve surrounding the flexible, single lumen tube is necessary to maintain the focus of the waterjet during operation, it helps avoid instability, and constrain the bending of the device to a plane with maximum and minimum angles of -90 and +90 with respect to the straight configuration.

The user independently selects both the intensity of the water beam and the articulation of the tip. The intensity of the water beam is determined through the use of a foot pedal that directly control a proportional solenoid valve. The valve is connected to a pressurized dispensing vessel through 3/8 tubing. The articulation of the tip is obtained through the

103
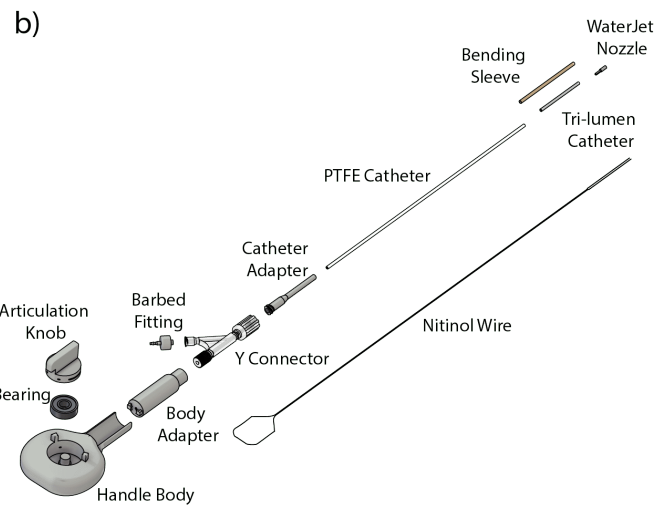
Figure 6.1: a) Picture of the Prototype. b) Exploded view of the WAterjet Necrosectomy Device (WAND).

rotation of an articulation knob on the device handle. The knob is mounted on a mechanical bearing that allows low friction with respect to the anchoring shaft and is connected tangentially to the wires. The rotation of the knob causes the push of one wire with pull of the other wire in a very intuitive manner. The handle adapter attaches to a Y-connector to prevent backflow of water.

The prototype, with exception of the PTFE Catheter, the Y-Connector and the bearing, was entirely fabricated using a Stereolithography 3D printer (Form 2, Formlabs, USA).

6.3 Waterjet Force Modeling

To achieve debris fragmentation while preserving tissue safety, the geometry of the nozzle as well as the overall diameter and length of the catheter play an important role. Considering the fluid conservation of mass and assuming a time invariant laminar flow, the water jet force generated by the nozzle can be calculated using the thrust equation as follow:

$$F = -\dot{m}(v_{in} - v_{out}) \tag{6.1}$$

where $\dot{m}$ is the mass flow rate through the cavity, v_{out} and v_{in} the outlet and inlet velocity, p_{out} the pressure acting on A_{out} and n is the unit vector normal to the inner wall surface. The analytical model obtained by integration over the two different contours was then validated using experimental data.

Volumetric flowrate was estimated starting from the energy conservation equation:

$$\frac{p_2 - p_1}{\gamma} + \frac{v_2^2 - v_1^2}{g} + h_l = 0 \tag{6.2}$$

where p_2 and p_1 are pressures at two location on the hydraulic system, v_2^2 and v_1^2 are fluid velocities, $\gamma = \rho g$ is the specific weight of the fluid and h_l is the head loss in the tubing that can be calculated as:

$$h_l = f\frac{L}{D}\frac{v^2}{2g} \tag{6.3}$$

where f is the Darcy friction factor, L and D are the length and internal diameter of the tube, v is the velocity of the fluid and g is the gravitational constant. Jet flow rate was measured during jet force testing using an ultrasonic flowmeter (Atrato, Model: Titan 760), which provides the instantaneous flow rate through the jet. Basic fluid dynamics theory dictates that for a non-deforming system at steady state, jet force is a function of
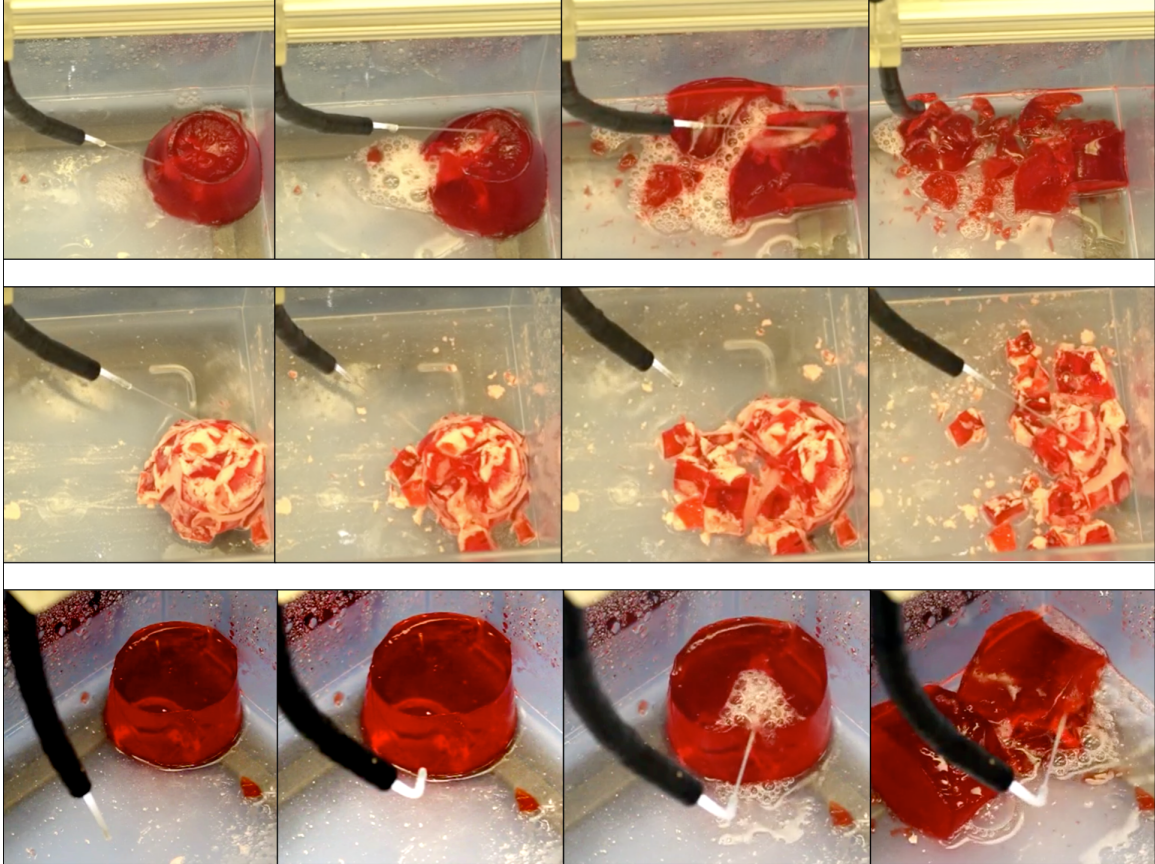
Figure 6.2: Experimental testing of the WAND using gelatin of various levels of stiffness. The independent articulation of the device from the endoscope is shown in the bottom row.

flow rate alone. This relationship provides a basis for control of the jet actuation force.

6.4 Experimental Validation

The use of waterjet pressure serves the dual purposes of both dissecting/fragmenting necrotic tissue and facilitating irrigation of the necroma cavity.

6.4.1 Benchtop Testing

Initial phase testing demonstrated successful WAND fragmentation of gelatin in varying degrees of stiffness as a surrogate for necrotic debris (Fig. 6.2). In this setup, the WAND achieved a surface pressure of 1 bar at a flow rate of 0.45 L/min. Overall, the
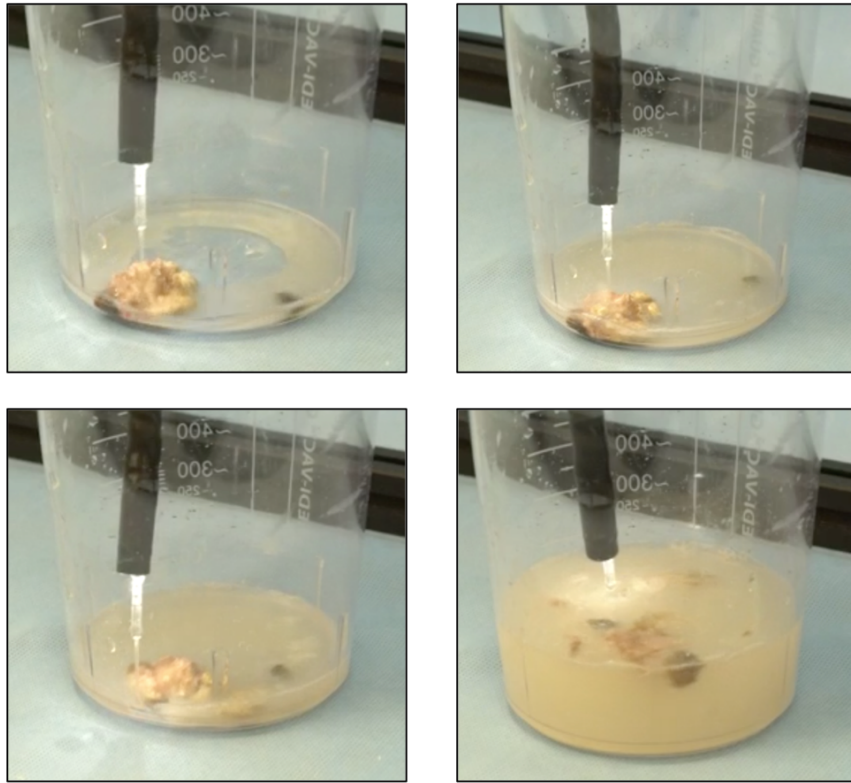
Figure 6.3: Experimental testing using freshly harvested pancreatic necrotic tissue. Fragmentation was achieved using multiple passes of the directed water beam across the necrotic tissue.

WAND can achieve a maximum flow rate of 0.5 L/min while reaching a maximum surface pressure of 1.3 bar, which is much lower than the tissue safety threshold of 3 bar.

6.4.2   Ex-vivo Testing

Second phase benchtop testing demonstrated successful WAND fragmentation of freshly harvested human pancreatic necrosis (Fig. 6.3). In this example, the WAND is achieving a surface pressure of 0.72 bar at a flow rate of 0.37 L/min. Obliteration of the explanted human pancreatic necrosis was successful.
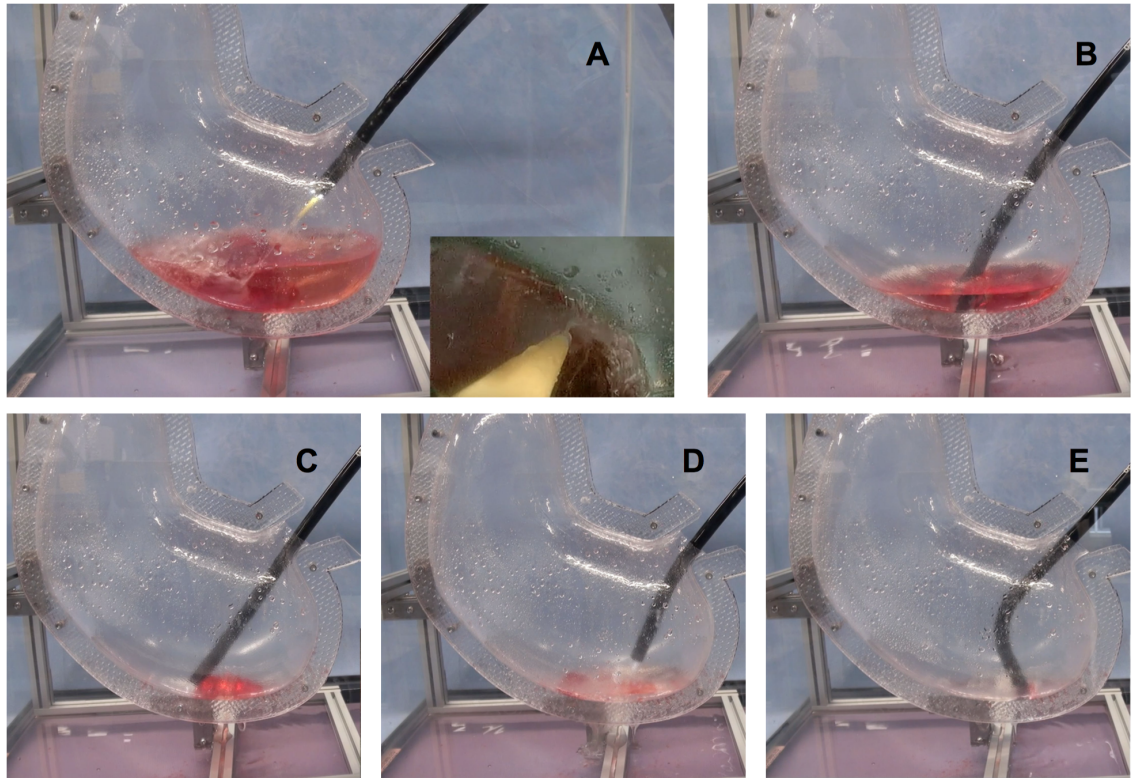
Figure 6.4: Experimental testing of the WAND in stomach phantom. A) Gelatin is dissected in confined work environment using the WAND. B) Excess fluid is aspirated using standard endoscope. C) Larger pieces of gelatin debris are unable to be aspirated. D) WAND is reinserted, remaining pieces are fragmented. E) All gelatin and fluid is successfully removed.

6.4.3 Stomach Phantom Testing

The WAND was further tested to assess articulation and function in a confined environment. Gelatin was placed inside a clear stomach phantom visible from a frontal view and the view of the endoscope in (Fig. 6.4). A continuous waterjet force was applied with a surface pressure of 0.72 bar at a flow rate of 0.37 L/min to achieve adequate fragmentation. The WAND was completely removed from the endoscope and fragmented gelatin was aspirated through the empty working channel of the endoscope. While some gelatin chunks were too big to be aspirated initially, the WAND was reinserted for further fragmentation and subsequent aspiration to successfully remove all gelatin from the confined environ-
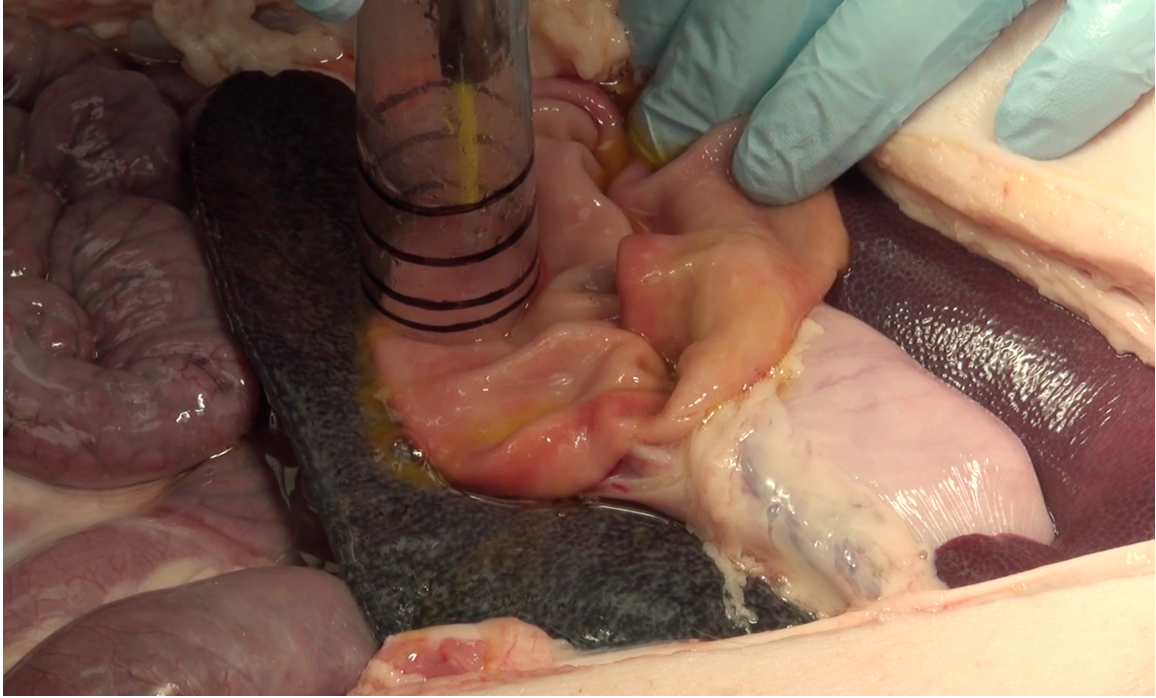
Figure 6.5: In-vivo safety testing of WAND on tissues surrounding the pancreas, on the small intestine in this example.

ment. This trial demonstrates the WAND's capability to be inserted and removed multiple times throughout the course of a procedure, allowing for multiple passes of fragmentation and aspiration.

6.4.4   In-vivo Safety Testing

To evaluate system safety, the WAND was tested in-vivo using a 40kg female Yorkshire-Landrace cross swine (Fig. 6.5). Effects of the WAND on the pancreas, small intestine, liver, stomach, spleen, and aorta were assessed. To assess maximum possible damage, the tip of the WAND was held within 5 millimeters of the porcine organ or vessel for 30 seconds over a range of 0.04 bar to 1.3 bar to determine if any tissue damage would occur. There were 5 cases of mild blanching and erythema at surface pressures above 0.72 bar. None of the organs or vessels sustained perforation, erosion, or excoriation at any of the pressures, including at the maximal pressure for the platform.

6.5 Conclusions

This chapter demostrated benchtop development and ex-vivo testing of a novel necro-sectomy debridement device, compatible for use through the working channel of a flexible endoscope. Future work on the device include improvement of design as well as additional ex-vivo and first in-human in-vivo testing.

Chapter 7

Conclusion

7.1   Summary of Findings

This dissertation presents the design, modeling, and control of tip follower actuated soft continuum devices with its primary application in gastrointestinal endoscopy. This work also describes novel methods for controlling waterjet force to inspect and intervene in the endoluminal environment and the experimental validation of these methods.

In Chapter 2, design improvements from the platform presented in [29] enable the platform to serve as an option for UGI screening in LMICs. The improvements are as follows: First, the pump was replaced by both a dispensing vessel and an air pressure tank. A pressure regulator connected to the dispensing vessel allows precise regulation of the overall pressure, without requiring water to constantly flow within the system. On/off valves were replaced by proportional valves which allow selective control of the flowrate at each waterjet. Next, the four full-length single lumen tubes were replaced with a multilumen catheter connected distally to a low stiffness section, which is constituted by a soft elastomer sleeve that wraps around single lumen flexible tubing. This allows the tip of the scope to achieve high bending angles while maintaining a uniform body. This design allows the force generated by the waterjets to be uniquely dependent on the fluid flow rate passing through the tubing and the geometry of the nozzle, while the mechanical deflection is determined by choosing the geometric and material properties of the sleeve. These design improvements result in improved controllability and repeatability of results and fulfill the need of a low cost, disposable, transportable device for screening in LMIC.

Chapter 3 presents modeling of TFA soft manipulators using both a PRB-C and a Cosserat rod framework. It also explores calibration issues that are common in CM designs and proposes a method that improves the disturbance estimation based on sensor feedback.

111

This compensates for unmodeled effects such as friction, nonlinear elastic and/or spatially varying material properties, and manufacturing imprecision. Experimental validation on the HJ endoscopic device shows similar behavior of the two modeling frameworks with comparable position and orientation errors. The proposed disturbance method significantly improves the modeling accuracy of SCM under TFA and is easy to generalize to other designs where embedding sensors is possible. Results show 42% positional error reduction and 32% orientation error reduction for 75° deflection of the end effector when compared to standard geometric calibration.

Chapter 4 describes novel control methods of soft continuum manipulators under TFA. The proposed closed-loop scheme improves the tracking capability when compared to the open-loop test cases. For the open-loop case, large variability is evident across trial repetitions, and the median error values range from 0.096 to 0.116 rad for the initially straight configuration and from 0.181 to 0.208 rad for the initially bent configuration. The relatively large standard deviations are in agreement with the large error distribution seen for all open-loop trials, highlighting high oscillations in the system. The influence of gravity on the soft manipulator under the initially bent configuration increases the median of the error from 0.106 to 0.197 rad when compared to the initially straight configuration, representing a increase of 85.5%. In comparison, the closed-loop scheme generates narrow error distributions and shows minimum variability of the median, ranging from 0.034 to 0.037 rad for the initially straight configuration and from 0.035 to 0.037 rad for the initially bent configuration. The influence of gravity in the initially bent configuration increases the median error from 0.0359 to 0.0360 rad, representing a negligible increase of 0.20%. The presented motion controller reduces oscillations that limit robot functionality allowing for high bending angles independent of the robot orientation. This has the potential to enable semi and fully autonomous manipulation tasks in the next generation of soft continuum robots under TFA.

Chapter 5 presents the teleoperation scheme and introduces a method for contact detec-

tion of soft continuum manipulators under TFA. The presented contact detection algorithm addresses one of the major challenges of eye-in-hand teleoperation, enabling the user to cope with external loading in an informed way and maintain intuitive control of the device. In addition to presenting a contact detection algorithm, this chapter has demonstrated for the first time the integration of a human operator into the control loop for a waterjet-actuated soft continuum robot. The intuitive and inexpensive user interface enabled even novice users to complete full gastric cancer screenings in a clinically reasonable amount of time as shown by the experiments in a phantom model. These results are highly promising for the HydroJet's potential as a first line screening device against one of the deadliest cancers worldwide.

Lastly, Chapter 6 presents the design and characterization of a novel WAterjet Necrosectomy Device (WAND). Experimental results show successful fragmentation of multiple densities of material including freshly explanted human pancreatic necrosis, at pressure and flow rates well below the threshold necessary to cause tissue damage. These results are paving the way for the first human in-vivo trials.

7.2   Future Research Directions

While this work provides a highly promising investigation of the HydroJet's capabilities as a telerobotic upper GI tract inspection device, more studies are needed to explore its full capabilities and limitations. From a medical standpoint, trials with a larger groups of participants from a broad variety of training backgrounds will serve to expand these results beyond proof of concept. This would be followed by future survival studies in animal models and then the first in-human trials. With regard to the teleoperation strategy, the disturbance estimation method presented in Chapter 4 can be integrated within the motion controller. This may allow the system to detect any external force applied from the environment and minimize the effect of these disturbances. A dynamic model of the actuation system would ultimately allow certain TFA soft manipulators to have faster actuation

113

wrench control and thus quicker device motion.

7.3   Summary of the Major Contribution to the Field

In summary, the main contributions of this work to the field of robotics and medical devices are as follows:

- Presented and experimentally characterized novel soft continuum manipulator designs that use waterjet force to inspect and intervene in the endoluminal environment.

- Presented methods to improve kinematic model accuracy for continuum manipulators under TFA through the use of a disturbance parameter that is updated in real-time through sensory feedback.

- Presented novel closed-loop control framework for soft continuum manipulators under TFA based on the Cosserat framework that integrates mixed pose/actuation feedback.

- First time integration of a human operator within the control loop scheme for a waterjet-actuated soft continuum robot and experimental validation of contact detection within an anatomically accurate stomach phantom.

With these contributions, the field of medical robotics and TFA soft continuum manipulators may be expanded and future directions can be pursued.

BIBLIOGRAPHY

[1] Puneet Kumar Singh and C Murali Krishna. Continuum arm robotic manipulator: A review. *Universal Journal of Mechanical Engineering*, 2(6):193–198, 2014.

[2] Ian D Walker, Darren M Dawson, Tamar Flash, Frank W Grasso, Roger T Hanlon, Binyamin Hochner, William M Kier, Christopher C Pagano, Christopher D Rahn, and Qiming M Zhang. Continuum robot arms inspired by cephalopods. In *Unmanned Ground Vehicle Technology VII*, volume 5804, pages 303–315. International Society for Optics and Photonics, 2005.

[3] N Giri and I Walker. Continuum robots and underactuated grasping. *Mechanical Sciences*, 2(1):51–58, 2011.

[4] Gregory S Chirikjian and Joel W Burdick. The kinematics of hyper-redundant robot locomotion. *IEEE transactions on robotics and automation*, 11(6):781–793, 1995.

[5] Siddharth Sanan, J Moidel, and Christopher G Atkeson. A continuum approach to safe robots for physical human interaction. In *Intl Symposium on Quality of Life Technology*. Citeseer, 2011.

[6] Hedyeh Rafii-Tari, Christopher J Payne, and Guang-Zhong Yang. Current and emerging robot-assisted endovascular catheterization technologies: a review. *Annals of biomedical engineering*, 42(4):697–715, 2014.

[7] Baldwin Po Man Yeung and Philip Wai Yan Chiu. Application of robotics in gastrointestinal endoscopy: A review. *World journal of gastroenterology*, 22(5):1811, 2016.

[8] Nabil Simaan, Kai Xu, Wei Wei, Ankur Kapoor, Peter Kazanzides, Russell Taylor, and Paul Flint. Design and integration of a telerobotic system for minimally invasive

surgery of the throat. *The International journal of robotics research*, 28(9):1134–1153, 2009.

[9] Arnau Garriga-Casanovas and Ferdinando Rodriguez y Baena. Complete follow-the-leader kinematics using concentric tube robots. *The International Journal of Robotics Research*, 37(1):197–222, 2018.

[10] Hunter B Gilbert, D Caleb Rucker, and Robert J Webster III. Concentric tube robots: The state of the art and future directions. In *Robotics Research*, pages 253–269. Springer, 2016.

[11] Pierre E Dupont, Jesse Lock, Brandon Itkowitz, and Evan Butler. Design and control of concentric-tube robots. *IEEE Transactions on Robotics*, 26(2):209–225, 2010.

[12] D Caleb Rucker, Bryan A Jones, and Robert J Webster III. A geometrically exact model for externally loaded concentric-tube continuum robots. *IEEE transactions on robotics: a publication of the IEEE Robotics and Automation Society*, 26(5):769, 2010.

[13] Marta Scali, Tim P Pusch, Paul Breedveld, and Dimitra Dodou. Needle-like instruments for steering through solid organs: A review of the scientific and patent literature. *Proceedings of the Institution of Mechanical Engineers, Part H: Journal of Engineering in Medicine*, 231(3):250–265, 2017.

[14] Robert J Webster III, Jin Seob Kim, Noah J Cowan, Gregory S Chirikjian, and Allison M Okamura. Nonholonomic modeling of needle steering. *The International Journal of Robotics Research*, 25(5-6):509–525, 2006.

[15] Andrea Bajo and Nabil Simaan. Kinematics-based detection and localization of contacts along multisegment continuum robots. *IEEE Transactions on Robotics*, 28(2):291–302, 2012.

[16] Mohsen Mahvash and Pierre E Dupont. Stiffness control of surgical continuum manipulators. *IEEE Transactions on Robotics*, 27(2):334–345, 2011.

[17] Daniela Rus and Michael T Tolley. Design, fabrication and control of soft robots. *Nature*, 521(7553):467, 2015.

[18] N Elango and AAM Faudzi. A review article: investigations on soft materials for soft robot manipulations. *The International Journal of Advanced Manufacturing Technology*, 80(5-8):1027–1037, 2015.

[19] Mariangela Manti, Vito Cacucciolo, and Matteo Cianchetti. Stiffening in soft robotics: A review of the state of the art. *IEEE Robotics & Automation Magazine*, 23(3):93–106, 2016.

[20] G Dogangil, BL Davies, and F Rodriguez y Baena. A review of medical robotics for minimally invasive soft tissue surgery. *Proceedings of the Institution of Mechanical Engineers, Part H: Journal of Engineering in Medicine*, 224(5):653–679, 2010.

[21] Cecilia Laschi, Barbara Mazzolai, and Matteo Cianchetti. Soft robotics: Technologies and systems pushing the boundaries of robot abilities. *Sci. Robot*, 1(1):eaah3690, 2016.

[22] Tommaso Ranzani, Giada Gerboni, Matteo Cianchetti, and A Menciassi. A bioinspired soft manipulator for minimally invasive surgery. *Bioinspiration & biomimetics*, 10(3):035008, 2015.

[23] Hesheng Wang, Weidong Chen, Xiaojin Yu, Tao Deng, Xiaozhou Wang, and Rolf Pfeifer. Visual servo control of cable-driven soft robotic manipulator. In *IROS*, pages 57–62, 2013.

[24] Marcello Calisti, Michele Giorelli, Guy Levy, Barbara Mazzolai, B Hochner, Ce-

cilia Laschi, and Paolo Dario. An octopus-bioinspired solution to movement and manipulation for soft robots. *Bioinspiration & biomimetics*, 6(3):036002, 2011.

[25] Raphael Deimel and Oliver Brock. A compliant hand based on a novel pneumatic actuator. In *Robotics and Automation (ICRA), 2013 IEEE International Conference on*, pages 2047–2053. IEEE, 2013.

[26] Ramses V Martinez, Jamie L Branch, Carina R Fish, Lihua Jin, Robert F Shepherd, Rui MD Nunes, Zhigang Suo, and George M Whitesides. Robotic tentacles with three-dimensional mobility based on flexible elastomers. *Advanced materials*, 25(2):205–212, 2013.

[27] Guy Immega and Keith Antonelli. The ksi tentacle manipulator. In *Proceedings of 1995 IEEE International Conference on Robotics and Automation*, volume 3, pages 3149–3154. IEEE, 1995.

[28] P R Slawinski, A Z Taddese, K B Musto, K L Obstein, and P Valdastri. Autonomous Retroflexion of a Magnetic Flexible Endoscope. *IEEE Robotics and Automation Letters*, 2(3):1352–1359, 2017.

[29] Robert Caprara, Keith L Obstein, Gabriel Scozzarro, Christian Di Natali, Marco Beccani, Douglas R Morgan, and Pietro Valdastri. A platform for gastric cancer screening in low-and middle-income countries. *IEEE Transactions on Biomedical Engineering*, 62(5):1324–1332, 2015.

[30] Luca Ascari, Cesare Stefanini, Arianna Menciassi, Sambit Sahoo, Pierre Rabischong, and Paolo Dario. A new active microendoscope for exploring the subarachnoid space in the spinal cord. In *2003 IEEE International Conference on Robotics and Automation (Cat. No. 03CH37422)*, volume 2, pages 2657–2662. IEEE, 2003.

[31] Josie Hughes, Utku Culha, Fabio Giardina, Fabian Guenther, Andre Rosendo, and Fumiya Iida. Soft manipulators and grippers: a review. *Frontiers in Robotics and AI*, 3:69, 2016.

[32] Jacques Ferlay, Hai-Rim Shin, Freddie Bray, David Forman, Colin Mathers, and Donald Maxwell Parkin. Estimates of worldwide burden of cancer in 2008: Globocan 2008. *International journal of cancer*, 127(12):2893–2917, 2010.

[33] Ahmedin Jemal, Freddie Bray, Melissa M Center, Jacques Ferlay, Elizabeth Ward, and David Forman. Global cancer statistics. *CA: a cancer journal for clinicians*, 61(2):69–90, 2011.

[34] Catherine De Martel, Jacques Ferlay, Silvia Franceschi, Jérôme Vignat, Freddie Bray, David Forman, and Martyn Plummer. Global burden of cancers attributable to infections in 2008: a review and synthetic analysis. *The lancet oncology*, 13(6):607–615, 2012.

[35] Kyung-Jae Lee, Manami Inoue, Tetsuya Otani, Motoki Iwasaki, Shizuka Sasazuki, and Shoichiro Tsugane. Gastric cancer screening and subsequent risk of gastric cancer: a large-scale population-based cohort study, with a 13-year follow-up in japan. *International journal of cancer*, 118(9):2315–2321, 2006.

[36] Victor Pasechnikov, Sergej Chukov, Evgeny Fedorov, Ilze Kikuste, and Marcis Leja. Gastric cancer: prevention, screening and early diagnosis. *World journal of gastroenterology: WJG*, 20(38):13842, 2014.

[37] Julia Kovaleva, Frans TM Peters, Henny C van der Mei, and John E Degener. Transmission of infection by flexible gastrointestinal endoscopy and bronchoscopy. *Clinical microbiology reviews*, 26(2):231–254, 2013.

[38] Timothy E Moutafis, Donald C Freeman Jr, and Kevin Staid. Liquid jet-powered surgical instruments, December 30 2003. US Patent 6,669,710.

[39] Peter Gilling, Rana Reuther, Arman Kahokehr, and Mark Fraundorfer. Aquablation image-guided robot-assisted waterjet ablation of the prostate: initial clinical experience. *BJU International*, 117(6):923–929.

[40] WHO Globocan. Estimated cancer incidence, mortality and prevalence worldwide in 2012. *Lyon: WHO*, 2012.

[41] Christopher JL Murray and Alan D Lopez. Alternative projections of mortality and disability by cause 1990–2020: Global burden of disease study. *The Lancet*, 349(9064):1498–1504, 1997.

[42] Paul E Goss, Brittany L Lee, Tanja Badovinac-Crnjevic, Kathrin Strasser-Weippl, Yanin Chavarri-Guerra, Jessica St Louis, Cynthia Villarreal-Garza, Karla Unger-Saldaña, Mayra Ferreyra, Márcio Debiasi, et al. Planning cancer control in latin america and the caribbean. *The Lancet Oncology*, 14(5):391–436, 2013.

[43] D Brent Polk and Richard M Peek Jr. Helicobacter pylori: gastric cancer and beyond. *Nature Reviews Cancer*, 10(6):403, 2010.

[44] Pelayo Correa. Helicobacter pylori and gastric cancer: state of the art. *Cancer Epidemiology and Prevention Biomarkers*, 5(6):477–481, 1996.

[45] Lydia E Wroblewski, Richard M Peek, and Keith T Wilson. Helicobacter pylori and gastric cancer: factors that modulate disease risk. *Clinical microbiology reviews*, 23(4):713—739, October 2010.

[46] Kenichi Saito, Kazuko Arai, Masatomo Mori, Ryouta Kobayashi, and Ichiro Ohki. Effect of helicobacter pylori eradication on malignant transformation of gastric adenoma. *Gastrointestinal endoscopy*, 52(1):27–32, 2000.

[47] Hyun Jin Oh and Jin Su Kim. Clinical practice guidelines for endoscope reprocessing. *Clinical endoscopy*, 48(5):364, 2015.

[48] H Makuuchi, T Machimura, H Shimada, K Mizutani, O Chino, Y Kise, T Nishi, H Tanaka, T Mitomi, M Horiuchi, M Sakai, J Gotoh, J Sasaki, and Y Osamura. Endoscopic screening for esophageal cancer in 788 patients with head and neck cancers. *The Tokai journal of experimental and clinical medicine*, 21(3):139—145, October 1996.

[49] Akira Oshima, Noriko Hirata, Takashi Ubukata, Katstuhiko Umeda, and Isaburo Fujimoto. Evaluation of a mass screening program for stomach cancer with a case-control study design. *International Journal of Cancer*, 38(6):829–833.

[50] TJ Wilhelm, H Mothes, D Chiwewe, B Mwatibu, and G Kähler. Gastrointestinal endoscopy in a low budget context: delegating egd to non-physician clinicians in malawi can be feasible and safe. *Endoscopy*, 44(02):174–176, 2012.

[51] Anastasios Koulaouzidis and Sarah Douglas. Capsule endoscopy in clinical practice: concise up-to-date overview. In *Clinical and experimental gastroenterology*, 2009.

[52] Daniel S. Mishkin, Ram Chuttani, Joseph Croffie, James DiSario, Julia Liu, Raj Shah, Lehel Somogyi, William Tierney, Louis M. Wong Kee Song, and Bret T. Petersen. Asge technology status evaluation report: wireless capsule endoscopy. *Gastrointestinal Endoscopy*, 63(4):539–545, 2019/04/28 2006.

[53] Shi Zhaocun, Yu Jian, and Luo Xiaohui. Research on the modeling and simulation of reaction thrust characteristics of water jet. In *2015 International Conference on Fluid Power and Mechatronics (FPM)*, pages 80–83. IEEE, 2015.

[54] YS Yang, SL Nie, YQ Zhu, YP Li, and GH Huang. Reaction thrust of submerged water jets. *Proceedings of the Institution of Mechanical Engineers, Part A: Journal of Power and Energy*, 221(4):565–573, 2007.

[55] Shuhei Miyashita, Steven Guitron, Kazuhiro Yoshida, Shuguang Li, Dana D Damian, and Daniela Rus. Ingestible, controllable, and degradable origami robot

for patching stomach wounds. In *2016 IEEE International Conference on Robotics and Automation (ICRA)*, pages 909–916. IEEE, 2016.

[56] Nicolo Garbin, Long Wang, James H Chandler, Keith L Obstein, Nabil Simaan, and Pietro Valdastri. Dual-continuum design approach for intuitive and low-cost upper gastrointestinal endoscopy. *IEEE Transactions on Biomedical Engineering*, 2018.

[57] Robert J Webster III and Bryan A Jones. Design and kinematic modeling of constant curvature continuum robots: A review. *The International Journal of Robotics Research*, 29(13):1661–1683, 2010.

[58] Matthias Rolf and Jochen J Steil. Efficient exploratory learning of inverse kinematics on a bionic elephant trunk. *IEEE transactions on neural networks and learning systems*, 25(6):1147–1160, 2014.

[59] Roy J Roesthuis and Sarthak Misra. Steering of multisegment continuum manipulators using rigid-link modeling and fbg-based shape sensing. *IEEE transactions on robotics*, 32(2):372–382, 2016.

[60] Larry L Howell. Compliant mechanisms. In *21st Century Kinematics*, pages 189–216. Springer, 2013.

[61] Larry L Howell and Ashok Midha. Parametric deflection approximations for end-loaded, large-deflection beams in compliant mechanisms. 1995.

[62] Hafez Tari, GL Kinzel, and DA Mendelsohn. Cartesian and piecewise parametric large deflection solutions of tip point loaded euler–bernoulli cantilever beams. *International Journal of Mechanical Sciences*, 100:216–225, 2015.

[63] Guimin Chen and Ruiyu Bai. Modeling large spatial deflections of slender bisymmetric beams in compliant mechanisms using chained spatial-beam constraint model. *Journal of Mechanisms and Robotics*, 8(4), 2016.

[64] Joby Pauly and Ashok Midha. Pseudo-rigid-body model chain algorithm: part 1 introduction and concept development. In *ASME 2006 International Design Engineering Technical Conferences and Computers and Information in Engineering Conference*, pages 173–181. American Society of Mechanical Engineers Digital Collection, 2006.

[65] Robert P Chase Jr, Robert H Todd, Larry L Howell, and Spencer P Magleby. A 3-d chain algorithm with pseudo-rigid-body model elements. *Mechanics based design of structures and machines*, 39(1):142–156, 2011.

[66] Mahta Khoshnam and Rajni V Patel. A pseudo-rigid-body 3r model for a steerable ablation catheter. In *2013 IEEE International Conference on Robotics and Automation*, pages 4427–4432. IEEE, 2013.

[67] Tipakorn Greigarn and M Cenk Çavuşoğlu. Pseudo-rigid-body model and kinematic analysis of mri-actuated catheters. In *2015 IEEE International Conference on Robotics and Automation (ICRA)*, pages 2236–2243. IEEE, 2015.

[68] Piotr R Slawinski, Keith L Obstein, and Pietro Valdastri. Capsule endoscopy of the future: Whats on the horizon? *World Journal of Gastroenterology: WJG*, 21(37):10528, 2015.

[69] Addisu Z Taddese, Piotr R Slawinski, Keith L Obstein, and Pietro Valdastri. Nonholonomic closed-loop velocity control of a soft-tethered magnetic capsule endoscope. In *2016 IEEE/RSJ International Conference on Intelligent Robots and Systems (IROS)*, pages 1139–1144. IEEE, oct 2016.

[70] Frederick Largilliere, Valerian Verona, Eulalie Coevoet, Mario Sanz-Lopez, Jeremie Dequidt, and Christian Duriez. Real-time control of soft-robots using asynchronous finite element modeling. In *Robotics and Automation (ICRA), 2015 IEEE International Conference on*, pages 2550–2555. IEEE, 2015.

[71] Deepak Trivedi, Christopher D Rahn, William M Kier, and Ian D Walker. Soft robotics: Biological inspiration, state of the art, and future research. *Applied bionics and biomechanics*, 5(3):99–117, 2008.

[72] D Caleb Rucker and Robert J Webster III. Statics and dynamics of continuum robots with general tendon routing and external loading. *IEEE Transactions on Robotics*, 27(6):1033–1044, 2011.

[73] Janis Edelmann, Andrew J. Petruska, and Bradley J. Nelson. Magnetic control of continuum devices. *International Journal of Robotics Research*, 36(1):68–85, 2017.

[74] Louis B Kratchman, Trevor L Bruns, Jake J Abbott, and Robert J Webster. Guiding elastic rods with a robot-manipulated magnet for medical applications. *IEEE Transactions on Robotics*, 33(1):227–233, 2017.

[75] Robert J Webster, Joseph M Romano, and Noah J Cowan. Kinematics and calibration of active cannulas. In *2008 IEEE International Conference on Robotics and Automation*, pages 3888–3895. IEEE, 2008.

[76] Stanislao Grazioso, Giuseppe Di Gironimo, and Bruno Siciliano. A geometrically exact model for soft continuum robots: The finite element deformation space formulation. *Soft robotics*, 2018.

[77] Jesse Lock and Pierre E Dupont. Friction modeling in concentric tube robots. In *2011 IEEE International Conference on Robotics and Automation*, pages 1139–1146. IEEE, 2011.

[78] Guru Subramani and Michael R Zinn. Tackling friction-an analytical modeling approach to understanding friction in single tendon driven continuum manipulators. In *2015 IEEE International Conference on Robotics and Automation (ICRA)*, pages 610–617. IEEE, 2015.

[79] Sylvaine Leleu, Hisham Abou-Kandil, and Yvan Bonnassieux. Piezoelectric actuators and sensors location for active control of flexible structures. In *Proceedings of the 17th IEEE Instrumentation and Measurement Technology Conference [Cat. No. 00CH37066]*, volume 2, pages 818–823. IEEE, 2000.

[80] Sergey Edward Lyshevski. Data-intensive analysis and control of flexible pointing systems with pzt actuators. In *IEEE International Frequency Control Symposium and PDA Exhibition Jointly with the 17th European Frequency and Time Forum, 2003. Proceedings of the 2003*, pages 948–956. IEEE, 2003.

[81] Xinhua Yi, Jinwu Qian, Linyong Shen, Yanan Zhang, and Zhen Zhang. An innovative 3d colonoscope shape sensing sensor based on fbg sensor array. In *2007 International Conference on Information Acquisition*, pages 227–232. IEEE, 2007.

[82] David B Camarillo, Kevin E Loewke, Christopher R Carlson, and J Kenneth Salisbury. Vision based 3-d shape sensing of flexible manipulators. In *2008 IEEE International Conference on Robotics and Automation*, pages 2940–2947. IEEE, 2008.

[83] Michael W Hannan and Ian D Walker. Real-time shape estimation for continuum robots using vision. *Robotica*, 23(5):645–651, 2005.

[84] Richard M Murray, Zexiang Li, S Shankar Sastry, and S Shankara Sastry. *A mathematical introduction to robotic manipulation*. CRC press, 1994.

[85] Chris Kimball and Lung-Wen Tsai. Modeling of flexural beams subjected to arbitrary end loads. *J. Mech. Des.*, 124(2):223–235, 2002.

[86] Yu V Zakharov and KG Okhotkin. Nonlinear bending of thin elastic rods. *Journal of applied mechanics and technical physics*, 43(5):739–744, 2002.

[87] Aimei Zhang and Guimin Chen. A comprehensive elliptic integral solution to the

large deflection problems of thin beams in compliant mechanisms. *Journal of Mechanisms and Robotics*, 5(2), 2013.

[88] Larry L Howell. *Compliant mechanisms*. John Wiley & Sons, 2001.

[89] Bryan A Jones, Ricky L Gray, and Krishna Turlapati. Three dimensional statics for continuum robotics. In *Intelligent Robots and Systems, 2009. IROS 2009. IEEE/RSJ International Conference on*, pages 2659–2664. IEEE, 2009.

[90] D Caleb Rucker and Robert J Webster. Computing jacobians and compliance matrices for externally loaded continuum robots. In *Robotics and Automation (ICRA), 2011 IEEE International Conference on*, pages 945–950. IEEE, 2011.

[91] Ellis Harold Dill. Kirchhoff's theory of rods. *Archive for History of Exact Sciences*, 44(1):1–23, 1992.

[92] Du Q Huynh. Metrics for 3d rotations: Comparison and analysis. *Journal of Mathematical Imaging and Vision*, 35(2):155–164, 2009.

[93] Sebastian Madgwick. An efficient orientation filter for inertial and inertial/magnetic sensor arrays. *Report x-io and University of Bristol (UK)*, 25:113–118, 2010.

[94] D Caleb Rucker, Jadav Das, Hunter B Gilbert, Philip J Swaney, Michael I Miga, Nilanjan Sarkar, and Robert J Webster. Sliding mode control of steerable needles. *IEEE Transactions on Robotics*, 29(5):1289–1299, 2013.

[95] Mohsen Khadem, Carlos Rossa, Ron S Sloboda, Nawaid Usmani, and Mahdi Tavakoli. Ultrasound-guided model predictive control of needle steering in biological tissue. *Journal of Medical Robotics Research*, 1(01):1640007, 2016.

[96] Bita Fallahi, Carlos Rossa, Ron S Sloboda, Nawaid Usmani, and Mahdi Tavakoli. Sliding-based switching control for image-guided needle steering in soft tissue. *IEEE Robotics and Automation Letters*, 1(2):860–867, 2016.

[97] Michele Giorelli, Federico Renda, Marcello Calisti, Andrea Arienti, Gabriele Ferri, and Cecilia Laschi. Neural network and jacobian method for solving the inverse statics of a cable-driven soft arm with nonconstant curvature. *IEEE Transactions on Robotics*, 31(4):823–834, 2015.

[98] Thomas George Thuruthel, Yasmin Ansari, Egidio Falotico, and Cecilia Laschi. Control strategies for soft robotic manipulators: A survey. *Soft robotics*, 5(2):149–163, 2018.

[99] M Giorelli, F Renda, M Calisti, A Arienti, G Ferri, and C Laschi. Learning the inverse kinetics of an octopus-like manipulator in three-dimensional space. *Bioinspiration & biomimetics*, 10(3):035006, 2015.

[100] David B Camarillo, Christopher R Carlson, and J Kenneth Salisbury. Configuration tracking for continuum manipulators with coupled tendon drive. *IEEE transactions on robotics*, 25(4):798–808, 2009.

[101] Michael C Yip and David B Camarillo. Model-less feedback control of continuum manipulators in constrained environments. *IEEE Transactions on Robotics*, 30(4):880–889, 2014.

[102] Andrea Bajo, Roger E Goldman, and Nabil Simaan. Configuration and joint feedback for enhanced performance of multi-segment continuum robots. In *2011 IEEE International Conference on Robotics and Automation*, pages 2905–2912. IEEE, 2011.

[103] Roger A Horn and Charles R Johnson. *Matrix analysis*. Cambridge university press, 2012.

[104] John Till and D Caleb Rucker. Elastic stability of cosserat rods and parallel continuum robots. *IEEE Transactions on Robotics*, 33(3):718–733, 2017.

[105] Janis Edelmann, Andrew J Petruska, and Bradley J Nelson. Magnetic control of continuum devices. *The International Journal of Robotics Research*, 36(1):68–85, 2017.

[106] Alexander T Miller, Robert E Sedlack, Walter J Coyle, Keith L Obstein, Michael A Poles, Francisco C Ramirez, Frank J Lukens, C Prakash Gyawali, Jennifer A Christie, Denise Kalmaz, et al. Competency in esophagogastroduodenoscopy: A validated tool for assessment and generalizable benchmarks for gastroenterology fellows. *Gastrointestinal endoscopy*, 2019.

[107] David Ketcheson and Umair bin Waheed. A comparison of high-order explicit runge–kutta, extrapolation, and deferred correction methods in serial and parallel. *Communications in Applied Mathematics and Computational Science*, 9(2):175–200, 2014.

[108] Sebastian OH Madgwick, Andrew JL Harrison, and Ravi Vaidyanathan. Estimation of imu and marg orientation using a gradient descent algorithm. In *Rehabilitation Robotics (ICORR), 2011 IEEE International Conference on*, pages 1–7. IEEE, 2011.

[109] Mohsen Mahvash and Pierre E Dupont. Stiffness control of a continuum manipulator in contact with a soft environment. In *Proceedings of the... IEEE/RSJ International Conference on Intelligent Robots and Systems. IEEE/RSJ International Conference on Intelligent Robots and Systems*, volume 2010, page 863. NIH Public Access, 2010.

[110] Stephen Tully, Andrea Bajo, George Kantor, Howie Choset, and Nabil Simaan. Constrained filtering with contact detection data for the localization and registration of continuum robots in flexible environments. In *Robotics and Automation (ICRA), 2012 IEEE International Conference on*, pages 3388–3394. IEEE, 2012.

[111] Andrea Bajo, Latif M Dharamsi, James L Netterville, C Gaelyn Garrett, and Nabil

Simaan. Robotic-assisted micro-surgery of the throat: The trans-nasal approach. In *2013 IEEE International Conference on Robotics and Automation*, pages 232–238. IEEE, 2013.

[112] Jessica Burgner, D Caleb Rucker, Hunter B Gilbert, Philip J Swaney, Paul T Russell, Kyle D Weaver, and Robert J Webster. A telerobotic system for transnasal surgery. *IEEE/ASME Transactions on Mechatronics*, 19(3):996–1006, 2013.

[113] Hari Das, Haya Zak, Jason Johnson, John Crouch, and Don Frambach. Evaluation of a telerobotic system to assist surgeons in microsurgery. *Computer Aided Surgery*, 4(1):15–25, 1999.

[114] Andrew L Orekhov, Caroline B Black, John Till, Scotty Chung, and D Caleb Rucker. Analysis and validation of a teleoperated surgical parallel continuum manipulator. *IEEE Robotics and Automation Letters*, 1(2):828–835, 2016.

[115] Daniel E Whitney. Resolved motion rate control of manipulators and human prostheses. *IEEE Transactions on man-machine systems*, 10(2):47–53, 1969.

[116] Andrea Bajo and Nabil Simaan. Finding lost wrenches: Using continuum robots for contact detection and estimation of contact location. In *2010 IEEE international conference on robotics and automation*, pages 3666–3673. IEEE, 2010.

[117] Yue Chen, Long Wang, Kevin Galloway, Isuru Godage, Nabil Simaan, and Eric Barth. Modal-based kinematics and contact detection of soft robots. *arXiv preprint arXiv:1906.11654*, 2019.

[118] Charles R Johnson and Roger A Horn. *Matrix analysis*. Cambridge University Press Cambridge, 1985.

[119] Santhi Swaroop Vege, Matthew J DiMagno, Chris E Forsmark, Myriam Martel, and Alan N Barkun. Initial medical treatment of acute pancreatitis: American gastroen-

terological association institute technical review. *Gastroenterology*, 154(4):1103–1139, 2018.

[120] V Raman Muthusamy, Vinay Chandrasekhara, Ruben D Acosta, David H Bruining, Krishnavel V Chathadi, Mohamad A Eloubeidi, Ashley L Faulx, Lisa Fonkalsrud, Suryakanth R Gurudu, Mouen A Khashab, et al. The role of endoscopy in the diagnosis and treatment of inflammatory pancreatic fluid collections. *Gastrointestinal endoscopy*, 83(3):481–488, 2016.

[121] Rogier P Voermans, Marc G Besselink, and Paul Fockens. Endoscopic management of walled-off pancreatic necrosis. *Journal of Hepato-Biliary-Pancreatic Sciences*, 22(1):20–26, 2015.

[122] Todd H Baron and Richard A Kozarek. Endotherapy for organized pancreatic necrosis: perspectives after 20 years. *Clinical Gastroenterology and Hepatology*, 10(11):1202–1207, 2012.

[123] Patrick Yachimski. Can we now recommend hydrogen peroxide for pancreatic necrosectomy? time for controlled data. *Endoscopy international open*, 5(09):E854–E855, 2017.

[124] Pavol Hreha, Sergej Hloch, D Magurovd, Jan Valicek, Dražan Kozak, M Harnicdrovd, and Marko Rakin. Water jet technology used in medicine. *Tehnicki Vjesnik*, 17(2):237–240, 2010.

[125] Dimitrios N Papachristou and Richard Barters. Resection of the liver with a water jet. *British journal of Surgery*, 69(2):93–94, 1982.

[126] HG Rau, MW Wichmann, S Schinkel, E Buttler, S Pickelmann, R Schauer, and FW Schildberg. Surgical techniques in hepatic resections: Ultrasonic aspirator versus jet-cutter. a prospective randomized clinical trial. *Zentralblatt fur Chirurgie*, 126(8):586–590, 2001.